POLITECNICO DI TORINO
Repository ISTITUZIONALE

Frame-invariant sub-grid corrections to the Fictitious Domain Method for the simulation of particulate suspensions in nonlinear flows using OpenFOAM

Original
Frame-invariant sub-grid corrections to the Fictitious Domain Method for the simulation of particulate suspensions in nonlinear flows using OpenFOAM / Orsi, Michel; Lobry, Laurent; Peters, François. - In: JOURNAL OF COMPUTATIONAL PHYSICS. - ISSN 0021-9991. - ELETTRONICO. - 474:(2023), pp. 1-41. [10.1016/j.jcp.2022.111823]

Availability:
This version is available at: 11583/2996640 since: 2025-01-23T08:55:40Z

Publisher:
Elsevier

Published
DOI:10.1016/j.jcp.2022.111823

Terms of use:

This article is made available under terms and conditions as specified in the corresponding bibliographic description in the repository

Publisher copyright
Elsevier postprint/Author's Accepted Manuscript

© 2023. This manuscript version is made available under the CC-BY-NC-ND 4.0 license
http://creativecommons.org/licenses/by-nc-nd/4.0/.The final authenticated version is available online at:
http://dx.doi.org/10.1016/j.jcp.2022.111823

(Article begins on next page)

06 May 2026

Frame-invariant sub-grid corrections to the Fictitious Domain Method for the simulation of particulate suspensions in nonlinear flows using OpenFOAM

Michel Orsi, Laurent Lobry, François Peters*

Université Côte d'Azur, CNRS, Institut de Physique de Nice (INPHYNI), France

Abstract

A particle-scale simulation method for non-Brownian suspensions at low Reynolds numbers is presented, which is well suited to nonlinear flows. It is based on a Fictitious Domain Method supplemented by sub-grid corrections [*S. Gallier et al. "A fictitious domain approach for the simulation of dense suspensions", Journal of Computational Physics 256 (2014) 367–387*]. In the original method, the standard sub-grid corrections involve the underlying suspension linear flow. The conditions required to remove this ambient flow from the sub-grid corrections, while keeping frame indifference, are determined. A sub-grid correction matrix is built for the particle-particle and particle-wall hydrodynamic interactions, such that the mentioned conditions inherently hold. The method is validated against various flows that involve a few particles or a concentrated suspension in linear and nonlinear flows, with various boundary conditions.

Keywords: Suspensions, Nonlinear flows, Sub-grid corrections, Fictitious Domain Method, Discrete Element Method, OpenFOAM

1. Introduction

Particulate suspension flows are widely encountered in industrial applications, such as fluidized beds, fresh concrete flows, and uncured solid rocket fuel processing. They display a wide variety of behaviors depending on the nature of the suspending fluid, the particle density, shape, and size, the particle surface chemistry, etc. Even suspensions of model spherical particles in a Newtonian liquid in slow flow display strong non-Newtonian behaviors, such as normal stress differences, shear-thinning, and continuous and discontinuous shear-thickening. In addition, the transport of particles is strongly influenced by the shear-induced migration, according to which the particles migrate toward specific regions of the flow, basically from high- to low-stress regions. Even though these behaviors have been evidenced a long time ago, a perfect understanding of the involved mechanisms is still lacking.

However, particle scale simulations have substantially contributed to identifying the relevant physical mechanisms in play and probing their specific role in the various behaviors of interest. For instance, in the specific field of non-Brownian suspensions at low particle-scale Reynolds number, hydrodynamic interactions, both long- and short-range, direct interactions and external potential forces have a prominent influence. Their relative influence depends on the nature of the fluid (Newtonian or not), the particle volume fraction level, the density mismatch between particles and fluid (particle settling, inertia), and the velocity gradient intensity. Various numerical methods have been developed, which can account for part of these mechanisms, if not all of them. A few examples among a vast literature follow, and the interesting reader may consult the recent review of Maxey (2017) [1] and references therein for more detail. We leave aside very accurate

*Corresponding author. e-mail: francois.peters@univ-cotedazur.fr

methods that may not tackle more than a few particles. The below-mentioned methods especially differ in their treatment of hydrodynamic interactions.

The so-called Stokesian Dynamics [2, 3] has remarkably contributed to the understanding of suspension physics at a low Reynolds number. This is a meshless method that does not explicitly compute the fluid flow. It rests on a truncated multipole expansion of the velocity far-field induced by a particle. The short-range hydrodynamic interactions are accounted for using a correction resistance matrix computed in a pair-wise manner. Stokesian Dynamics is only suited to a Newtonian suspending liquid and has been mainly implemented for spherical particles, although it can tackle ellipsoidal particles as well [4]. A periodic shear flow is usually implemented, but the method has been upgraded so that plane boundary walls may be tackled [5].

Other methods involve the actual computation of the suspending fluid flow, so that long-range hydrodynamic interactions between particles are inherently accounted for. The fluid flow is computed over the whole simulation domain, including the particle domain, and the particle-fluid interactions are modeled in different ways. In the Force Coupling Method, a specific force density is exerted on the Newtonian suspending fluid, which allows the mean particle deformation to vanish. It is well suited to spheres [6, 7] and ellipsoids [8] in Stokes flow or at finite Reynolds number [9]. In the Immersed Boundary Method [10, 11], point forces are exerted on the fluid in the vicinity of the surface defining the solid boundaries to enforce the rigid body motion of the particle. In the Fictitious Domain Method (FDM), a body force is applied over the volume of each particle for the same purpose. The determination of the force may involve a Lagrange multiplier [12, 13, 14], or not [15]. Lagrange-multiplier-free FDMs have been applied to tackle spherical [16] or non-spherical particles [17]. The Smooth Particle Hydrodynamics is an example of a lagrangian meshless method where flow fields are represented using co-moving fluid volumes interacting via pairwise force. Particles and walls are modeled as frozen sets of particles similar to fluid ones. Both Brownian [18] and non-Brownian spherical particles in Newtonian [19] or non-Newtonian [20] fluids may be tackled, as well as arbitrary particle shape. Finally, the Lattice Boltzmann Method should be mentioned. In the frame of this method, the Navier-Stokes equations are not solved directly either, but the fluid flow is computed using as the primary quantity the one-particle discrete-velocity distribution function discretized at the nodes of a lattice [21, 22]. It should be stressed that all the methods mentioned in this paragraph need specific treatment to be able to account for short-range hydrodynamic interactions as the particles are closer to each other than the smallest length scale specified by the method (mesh size or particle size). In addition, particle motion is driven by Newton's law in the same way as in the Discrete Element Method (see below) and non-hydrodynamic forces such as particle interactions or external forces are readily accounted for.

Finally, the Discrete Element Method (DEM) has emerged as a fast and powerful numerical method for the simulation of suspensions [23, 24]. Originally developed in the field of dry granular material [25], it accounts for direct contact interactions, including friction. To allow suspension simulations, it must be supplemented with short-range lubrication interactions. It usually involves the relative velocities and positions of the particles together with the underlying suspension flow [23], although the latter is not included in some versions [26]. DEM is usually applied to the simulation of concentrated to highly concentrated suspensions. In the last decade, it allowed outstanding progress in the understanding of the Discontinuous Shear Thickening (DST) in non-Brownian suspensions [27, 23], as the stress-induced transition from frictionless to frictional particle interactions (see Ref. [28] for a review). The influence of various particle contact behaviors on DST has been also evidenced, such as adhesion [29] and rolling friction [29]. Apart from DST, the effect of adhesive forces in highly concentrated suspensions on jamming has been probed [30]. The rheology of suspensions in extensional flow has also been studied [31] using an additional drag force on the particle to emulate the mean flow. The main drawback of the method is that it does not account for long-range hydrodynamics, which seems not that important for straining flows, except maybe when shear-induced diffusion is addressed [32]. Nevertheless, problems are expected for flows where particle settling is relevant since long-range interactions are known to have primary effects (see Ref. [33] for a review). It should be noted that a kind of long-range hydrodynamic interactions may be re-introduced using a pore pressure field that must be solved [34, 35]. Another drawback is that the ambient flow field must be explicitly accounted for, which raises problems when the latter is not prescribed, as in the case of particle migration. In any case, for nonlinear flows to be induced, an external force density may be used [36].

Among the mentioned methods, those which deal with the actual computation of the flow offer significant benefits, usually at a significant computational cost though: they inherently account for long-range hydrodynamic interactions, they are well suited to the application of various boundary conditions, some of them may tackle any type of suspending liquid and various particle shape, at finite Reynolds number. These features allow such methods to tackle a wide variety of flows. Nonetheless, as mentioned above, they need a special procedure to account for the short-range hydrodynamic interactions, which are significant even for semi-dilute suspensions in straining flow. Such corrections are based on theoretical arguments from low-Reynolds-number hydrodynamics of Newtonian liquid [37, 38]. They are usually written in a form involving the underlying local flow of the suspension, which is assumed to be a linear straining flow [38]. Those lubrication-corrected methods allowed outstanding insight into suspension physics and mechanics, mainly for linear flows, including particle settling. However, they are less suited to nonlinear flows, especially when they are not prescribed but evolve with time, while many open questions involve such flows, starting with the shear-induced migration of particles that takes place in flows where the strain rate depends on the position, e.g. pressure-driven flows [39, 40]. In such flows, the particle volume fraction evolves with time, resulting in the variation of the velocity profile. As a consequence, lubrication corrections that would depend on the instantaneous velocity profile are difficult to apply. Thus, there is a need for conveniently design lubrication corrections that may apply to nonlinear flows.

In the current article, a Fictitious Domain Method supplemented by standard sub-grid corrections [16] is modified, so that nonlinear suspension flows may be conveniently tackled. The main features of the standard method are briefly recalled in the first section. In the second section, the sub-grid correction matrix is built, allowing the computation of the stress moments on the particles from the particle velocities and angular velocities only, with no reference to the ambient flow. The conditions under which the ambient flow may be safely omitted are explained in detail. In particular, due to the lack of inertia at the particle scale in low-Reynolds number flow, the relation between the stress moments on the particle and the velocities should be strictly frame-invariant. The correction matrix is finally presented, conveniently accounting for the short-range hydrodynamic interactions, while enforcing rigorous frame indifference. After a section devoted to the numerical implementation, the whole method is validated against linear and nonlinear flow configurations, involving a few particles or a concentrated suspension.

2. Fictitious domain method with sub-grid corrections

The Fictitious Domain Method supplemented by standard sub-grid corrections has been presented in detail in Ref. [16] and references therein. Its main features are recalled below.

2.1. The fictitious domain method: governing equations

In the FDM, the fluid flow is computed in the whole simulation domain $\mathcal{D}$ including the particles. A Newtonian fluid is assumed, with dynamic viscosity η and density ρ_f. The particles are rigid spheres whose density is denoted by ρ_p. The rigidity of the particles is enforced using a force density $\rho_f \boldsymbol{\lambda}$ that acts only in the volume of each particle $\mathcal{D}_p$. As a consequence, the fluid obeys modified Navier-Stokes equations:

$$\begin{gathered} \rho_f \left(\frac{\partial \mathbf{u}}{\partial t} + \mathbf{u} \cdot \boldsymbol{\nabla} \mathbf{u} \right) = \boldsymbol{\nabla} \cdot \boldsymbol{\sigma} + \rho_f \boldsymbol{\lambda} \\ \boldsymbol{\nabla} \cdot \mathbf{u} = 0 \end{gathered} \tag{1}$$

$$\boldsymbol{\sigma} = -p\boldsymbol{\delta} + \eta \left(\boldsymbol{\nabla} \mathbf{u} + \boldsymbol{\nabla} \mathbf{u}^T \right) \tag{2}$$

with the constraint that the fluid inside the particles undergoes rigid body motion:

$$\mathbf{u}(\mathbf{x}) = \mathbf{U}_p + \boldsymbol{\Omega}_p \times (\mathbf{x} - \mathbf{x}_p) \qquad \text{for} \quad \mathbf{x} \in \mathcal{D}_p \tag{3}$$

Then, Newton's equations read for each particle (p):

$$\begin{aligned} M_p \frac{\mathrm{d}\mathbf{U}_p}{\mathrm{d}t} &= \frac{\rho_p - \rho_f}{\rho_p} M_p \mathbf{g} + \mathbf{F}_p^h + \mathbf{F}_p^c + \mathbf{F}_p^{ext} \\ \mathbf{J}_p \cdot \frac{\mathrm{d}\mathbf{\Omega}_p}{\mathrm{d}t} + \mathbf{\Omega}_p \times (\mathbf{J}_p \cdot \mathbf{\Omega}_p) &= \mathbf{T}_p^h + \mathbf{T}_p^c + \mathbf{T}_p^{ext} \end{aligned} \tag{4}$$

where $\mathbf{F}_p^h$, $\mathbf{F}_p^c$, and $\mathbf{F}_p^{ext}$ respectively stand for the hydrodynamic, contact and additional external forces exerted on the particle (p), and $\mathbf{T}_p^h$, $\mathbf{T}_p^c$, and $\mathbf{T}_p^{ext}$ are the corresponding torques. Since the gravity force on the fluid has been absorbed in the pressure (Eqs. (1) and (2)), the hydrodynamic force $\mathbf{F}_p^h$ does not include the buoyancy force on the particle.

The momentum equations for the fluid (Eq. (1)) and for the particles (Eq. (4)) are coupled, since on the one hand the particle (p) and the fluid inside $\mathcal{D}_p$ share the same velocity field (Eq. (3)), and on the other hand the hydrodynamic force and torque exerted on any particle originate in the stress on the particle surface. In more detail, Eq. (1) may be integrated over the volume of each particle, which, with the help of Eq. (3), leads to:

$$\begin{aligned} \frac{\rho_f}{\rho_p} M_p \frac{\mathrm{d}\mathbf{U}_p}{\mathrm{d}t} &= \int_{\partial\mathcal{D}_p} \boldsymbol{\sigma} \cdot \mathbf{n} \, \mathrm{d}\mathcal{S} + \rho_f \int_{\mathcal{D}_p} \boldsymbol{\lambda} \mathrm{d}\mathcal{V} \\ \frac{\rho_f}{\rho_p} \left(\mathbf{J}_p \cdot \frac{\mathrm{d}\mathbf{\Omega}_p}{\mathrm{d}t} + \mathbf{\Omega}_p \times (\mathbf{J}_p \cdot \mathbf{\Omega}_p) \right) &= \int_{\partial\mathcal{D}_p} (\mathbf{x} - \mathbf{x}_p) \times \boldsymbol{\sigma} \cdot \mathbf{n} \, \mathrm{d}\mathcal{S} + \rho_f \int_{\mathcal{D}_p} (\mathbf{x} - \mathbf{x}_p) \times \boldsymbol{\lambda} \mathrm{d}\mathcal{V} \end{aligned} \tag{5}$$

The hydrodynamic force and torque exerted on each particle (p) as computed by the fluid flow solver are:

$$\begin{aligned} \mathbf{F}_p^{FDM} &= \int_{\partial\mathcal{D}_p} \boldsymbol{\sigma} \cdot \mathbf{n} \, \mathrm{d}\mathcal{S} \\ \mathbf{T}_p^{FDM} &= \int_{\partial\mathcal{D}_p} (\mathbf{x} - \mathbf{x}_p) \times \boldsymbol{\sigma} \cdot \mathbf{n} \, \mathrm{d}\mathcal{S} \end{aligned} \tag{6}$$

and from Eq. (5) they read:

$$\begin{aligned} \mathbf{F}_p^{FDM} &= \frac{\rho_f}{\rho_p} M_p \frac{\mathrm{d}\mathbf{U}_p}{\mathrm{d}t} - \rho_f \int_{\mathcal{D}_p} \boldsymbol{\lambda} \mathrm{d}\mathcal{V} \\ \mathbf{T}_p^{FDM} &= \frac{\rho_f}{\rho_p} \left(\mathbf{J}_p \cdot \frac{\mathrm{d}\mathbf{\Omega}_p}{\mathrm{d}t} + \mathbf{\Omega}_p \times (\mathbf{J}_p \cdot \mathbf{\Omega}_p) \right) - \rho_f \int_{\mathcal{D}_p} (\mathbf{x} - \mathbf{x}_p) \times \boldsymbol{\lambda} \mathrm{d}\mathcal{V} \end{aligned} \tag{7}$$

Then, the fluid flow solver cannot compute the flow at a scale smaller than the mesh grid size Δ, so a sub-grid (SG) correction has to be added to the force and torque on each particle, such that the total hydrodynamic force and torque in Eq. (4) read:

$$\begin{aligned} \mathbf{F}_p^h &= \mathbf{F}_p^{FDM} + \mathbf{F}_p^{SG} \\ \mathbf{T}_p^h &= \mathbf{T}_p^{FDM} + \mathbf{T}_p^{SG} \end{aligned} \tag{8}$$

From Eqs. (4), (7) and (8) the equations that govern the constraint on the force density $\boldsymbol{\lambda}$ are derived, and are written in Eq. (9) together with the fluid equations:

$$\rho_f \left(\frac{\partial \mathbf{u}}{\partial t} + (\mathbf{u} \cdot \boldsymbol{\nabla}) \, \mathbf{u} \right) = \eta \boldsymbol{\Delta} \mathbf{u} - \boldsymbol{\nabla} p + \rho_f \boldsymbol{\lambda} \tag{9a}$$

$$\boldsymbol{\nabla} \cdot \mathbf{u} = 0 \tag{9b}$$

$$\mathbf{u}(\mathbf{x}) = \mathbf{U}_p + \boldsymbol{\Omega}_p \times (\mathbf{x} - \mathbf{x}_p) \text{ in } \mathcal{D}_p \tag{9c}$$

$$\frac{\rho_p - \rho_f}{\rho_p} M_p \frac{\mathrm{d}\mathbf{U}_p}{\mathrm{d}t} = \frac{\rho_p - \rho_f}{\rho_p} M_p \mathbf{g} - \rho_f \int_{\mathcal{D}_p} \boldsymbol{\lambda} \mathrm{d}\mathcal{V} + \mathbf{F}_p^{SG} + \mathbf{F}_p^{c} + \mathbf{F}_p^{ext} \tag{9d}$$

$$\frac{\rho_p - \rho_f}{\rho_p} \left(\mathbf{J}_p \cdot \frac{\mathrm{d}\boldsymbol{\Omega}_p}{\mathrm{d}t} + \boldsymbol{\Omega}_p \times (\mathbf{J}_p \cdot \boldsymbol{\Omega}_p) \right) = -\rho_f \int_{\mathcal{D}_p} (\mathbf{x} - \mathbf{x}_p) \times \boldsymbol{\lambda} \mathrm{d}\mathcal{V} + \mathbf{T}_p^{SG} + \mathbf{T}_p^{c} + \mathbf{T}_p^{ext} \tag{9e}$$

In the following, inertia at particle scale is neglected, both for the fluid and the particles, so that the LHS of Eqs. (9a), (9d) and (9e) can be discarded.

Suspension rheology: particle stresslet

To compute the effective stress in a suspension of solid particles, the first moment of the hydrodynamic surface stress acting on each particle $\boldsymbol{D}_p$ [41, 42] is needed:

$$\boldsymbol{D}_p = \int_{\partial \mathcal{D}_p} \boldsymbol{\sigma} \cdot \mathbf{n} \otimes (\mathbf{x} - \mathbf{x}_p) \mathrm{d}\mathcal{S} \tag{10}$$

The anti-symmetric part of the force dipole $\boldsymbol{D}_p$ is the hydrodynamic torque exerted on the particle p, while the symmetric part, the so-called stresslet, determines the contribution of the particle to the effective stress. The latter is split into the deviatoric stresslet $\boldsymbol{S}_p$ and the isotropic part $s_p/3\, \boldsymbol{I}$, where s_p stands for the trace of the force dipole. Both $\boldsymbol{S}_p$ and s_p are computed from the FDM contribution and the sub-grid correction. As shown below, the FDM contribution of the dipole moment is computed from the force density $\boldsymbol{\lambda}$ and the solver pressure p. Using the divergence theorem, Eqs. (1) and (10) where inertia is neglected yield:

$$\boldsymbol{D}_p^{FDM} = -\rho_f \int_{\mathcal{D}_p} \boldsymbol{\lambda} \otimes (\mathbf{x} - \mathbf{x}_p) \mathrm{d}\mathcal{V} + \int_{\mathcal{D}_p} \boldsymbol{\sigma} \mathrm{d}\mathcal{V} \tag{11}$$

The strain rate vanishes inside the particle so that the stress $\boldsymbol{\sigma}$ written in Eq. (2) reduces to the isotropic pressure component and the FDM traceless stresslet and stresslet trace write:

$$\begin{aligned} \mathbf{S}_p^{FDM} &= -\rho_f \int_{\mathcal{D}_p} \left\{ \frac{1}{2} \left[\boldsymbol{\lambda} \otimes (\mathbf{x} - \mathbf{x}_p) + (\mathbf{x} - \mathbf{x}_p) \otimes \boldsymbol{\lambda} \right] - \frac{1}{3} \boldsymbol{\lambda} \cdot (\mathbf{x} - \mathbf{x}_p) \boldsymbol{\delta} \right\} \mathrm{d}\mathcal{V} \\ s_p^{FDM} &= -\int_{\mathcal{D}_p} \left[\rho_f \boldsymbol{\lambda} \cdot (\mathbf{x} - \mathbf{x}_p) + 3p \right] \mathrm{d}\mathcal{V} \end{aligned} \tag{12}$$

As previously mentioned, a sub-grid correction must be added to the FDM stresslet on the particles:

$$\begin{aligned} \mathbf{S}_p^{h} &= \mathbf{S}_p^{FDM} + \mathbf{S}_p^{SG} \\ s_p^{h} &= s_p^{FDM} + s_p^{SG} \end{aligned} \tag{13}$$

2.2. Standard sub-grid corrections

Since low-Reynolds-number flows at particle scale are considered, the governing equations for the liquid are linear (Stokes equations), resulting in linear relations between the stress moments exerted on the particle (force, torque, and stresslet) and the particle translational and angular velocities [38]. Such a relation holds for the total stress moment, as well as for the sub-grid corrections.

In more detail, we can assume the following expression for the ambient linear flow:

$$\mathbf{u}_\infty(\mathbf{x}) = \mathbf{U}_0 + \boldsymbol{\Omega}_\infty \times \mathbf{x} + \mathbf{E}_\infty \cdot \mathbf{x} \tag{14}$$

where $\mathbf{U}_0$, $\boldsymbol{\Omega}_\infty$, $\mathbf{E}_\infty$ are respectively the translational and angular velocities and the strain tensor of the fluid. The three of them are constant, i.e. do not depend on the position $\mathbf{x}$. The linear relation between sub-grid

forces, torques, and stresslets on the one hand, and the particle translational and rotational velocities, on the other hand, can be written as:

$$\begin{aligned}\boldsymbol{\mathcal{F}}^{SG} &= -\boldsymbol{\mathcal{R}}^{SG}_{\mathcal{FU}} \cdot (\boldsymbol{\mathcal{U}} - \boldsymbol{\mathcal{U}}_\infty) + \boldsymbol{\mathcal{R}}^{SG}_{\mathcal{FE}} : \mathbf{E}_\infty \\ \boldsymbol{\mathcal{S}}^{SG} &= -\boldsymbol{\mathcal{R}}^{SG}_{\mathcal{SU}} \cdot (\boldsymbol{\mathcal{U}} - \boldsymbol{\mathcal{U}}_\infty) + \boldsymbol{\mathcal{R}}^{SG}_{\mathcal{SE}} : \mathbf{E}_\infty \\ \mathbf{s}^{SG} &= -\boldsymbol{\mathcal{R}}^{SG}_{s\mathcal{U}} \cdot (\boldsymbol{\mathcal{U}} - \boldsymbol{\mathcal{U}}_\infty) + \boldsymbol{\mathcal{R}}^{SG}_{sE} : \mathbf{E}_\infty \end{aligned} \tag{15}$$

where $\boldsymbol{\mathcal{F}}^{SG}$ is the vector of sub-grid forces and torques exerted on the particles, $\boldsymbol{\mathcal{S}}^{SG}$ is the vector of traceless stresslets and $\mathbf{s}^{SG}$ is the vector of the traces of force dipoles:

$$\begin{aligned}\boldsymbol{\mathcal{F}}^{SG} &= \left(\mathbf{F}_1^{SG}, \mathbf{F}_2^{SG}, \dots, \mathbf{T}_1^{SG}, \mathbf{T}_2^{SG}, \dots\right) \\ \boldsymbol{\mathcal{S}}^{SG} &= \left(\mathbf{S}_1^{SG}, \mathbf{S}_2^{SG}, \dots,\right) \\ \mathbf{s}^{SG} &= \left(s_1^{SG}, s_2^{SG}, \dots,\right) \end{aligned} \tag{16}$$

$\boldsymbol{\mathcal{U}}$ is the vector of the particle translational and angular velocities:

$$\boldsymbol{\mathcal{U}} = (\mathbf{U}_1, \mathbf{U}_2, \dots, \boldsymbol{\Omega}_1, \boldsymbol{\Omega}_2, \dots) \tag{17}$$

$\boldsymbol{\mathcal{U}}_\infty$ is the vector of ambient flow velocities at the center of each particle:

$$\boldsymbol{\mathcal{U}}_\infty = (\mathbf{u}_\infty(\mathbf{x}_1), \mathbf{u}_\infty(\mathbf{x}_2), \dots, \boldsymbol{\Omega}_\infty, \boldsymbol{\Omega}_\infty, \dots) \tag{18}$$

and the various tensors $\boldsymbol{\mathcal{R}}^{SG}_{\dots}$ only depend on the particles sizes and positions.

As explained before, the sub-grid stress moments correction aims at supplying the system with the contribution of the short-scale flow that occurs between particles and that is missed by the fluid flow solver. As a consequence, the matrices are built as the superposition of the individual contributions of the pairs of close particles on the one hand, and the particles close to the bounding walls on the other hand. The former contributions will be tackled in detail in the following, while the latter are described in Appendix A.2 and Appendix D, and in the Supplementary Material.

The building block of the former contribution is the two-particle resistance matrix $\boldsymbol{\mathcal{R}}^{SG}_{2p}$, which allows writing the stress moments vector $\boldsymbol{\mathcal{M}}^{SG}$ as:

$$\begin{aligned}\boldsymbol{\mathcal{M}}^{SG} = \begin{pmatrix} \mathbf{F}_1^{SG} \\ \mathbf{F}_2^{SG} \\ \mathbf{T}_1^{SG} \\ \mathbf{T}_2^{SG} \\ \mathbf{S}_1^{SG} \\ \mathbf{S}_2^{SG} \\ s_1^{SG} \\ s_2^{SG} \end{pmatrix} &= -\boldsymbol{\mathcal{R}}^{SG}_{2p} \cdot \begin{pmatrix} \mathbf{U}_1 - \mathbf{u}_\infty(\mathbf{x}_1) \\ \mathbf{U}_2 - \mathbf{u}_\infty(\mathbf{x}_2) \\ \boldsymbol{\Omega}_1 - \boldsymbol{\Omega}_\infty \\ \boldsymbol{\Omega}_2 - \boldsymbol{\Omega}_\infty \\ -\mathbf{E}_\infty \\ -\mathbf{E}_\infty \end{pmatrix} \\ &= -\eta \begin{pmatrix} \mathbf{A}_{11} & \mathbf{A}_{12} & \tilde{\mathbf{B}}_{11} & \tilde{\mathbf{B}}_{12} & \tilde{\mathbf{G}}_{11} & \tilde{\mathbf{G}}_{12} \\ \mathbf{A}_{21} & \mathbf{A}_{22} & \tilde{\mathbf{B}}_{21} & \tilde{\mathbf{B}}_{22} & \tilde{\mathbf{G}}_{21} & \tilde{\mathbf{G}}_{22} \\ \mathbf{B}_{11} & \mathbf{B}_{12} & \mathbf{C}_{11} & \mathbf{C}_{12} & \tilde{\mathbf{H}}_{11} & \tilde{\mathbf{H}}_{12} \\ \mathbf{B}_{21} & \mathbf{B}_{22} & \mathbf{C}_{21} & \mathbf{C}_{22} & \tilde{\mathbf{H}}_{21} & \tilde{\mathbf{H}}_{22} \\ \mathbf{G}_{11} & \mathbf{G}_{12} & \mathbf{H}_{11} & \mathbf{H}_{12} & \mathbf{M}_{11} & \mathbf{M}_{12} \\ \mathbf{G}_{21} & \mathbf{G}_{22} & \mathbf{H}_{21} & \mathbf{H}_{22} & \mathbf{M}_{21} & \mathbf{M}_{22} \\ \mathbf{P}_{11} & \mathbf{P}_{12} & \mathbf{0} & \mathbf{0} & \mathbf{Q}_{11} & \mathbf{Q}_{12} \\ \mathbf{P}_{21} & \mathbf{P}_{22} & \mathbf{0} & \mathbf{0} & \mathbf{Q}_{21} & \mathbf{Q}_{22} \end{pmatrix} \cdot \begin{pmatrix} \mathbf{U}_1 - \mathbf{u}_\infty(\mathbf{x}_1) \\ \mathbf{U}_2 - \mathbf{u}_\infty(\mathbf{x}_2) \\ \boldsymbol{\Omega}_1 - \boldsymbol{\Omega}_\infty \\ \boldsymbol{\Omega}_2 - \boldsymbol{\Omega}_\infty \\ -\mathbf{E}_\infty \\ -\mathbf{E}_\infty \end{pmatrix} \end{aligned} \tag{19}$$

The elementary blocks $\mathbf{A}_{\alpha\beta}$, $\mathbf{B}_{\alpha\beta}$, ..., are tensors of different ranks, depending on the quantities that they connect. They only depend on the positions and sizes of the particles. Their physical meaning is straightforward: as an example, the tensor $\mathbf{A}_{12}$ defines the sub-grid force exerted on particle (p_1) in the particular case where particle (p_1) is at rest, and particle (p_2) undergoes a translational motion with velocity $\mathbf{U}_2$ in a liquid at rest ($\mathbf{u}_\infty(\mathbf{x}) = \mathbf{0}$) with $\mathbf{F}_1^{SG} = -\eta\mathbf{A}_{12} \cdot \mathbf{U}_2$. In the case of spherical particles of interest in the current study, the elementary tensors in Eq. (19) are simply written as a function of the radii of the particles, the distance between the particle centers, and the unit vector along the line of centers. In addition, they obey symmetry relations. This is recalled in detail in Appendix A.

It should be noted here that the matrix $\boldsymbol{\mathcal{R}}_{2p}^{SG}$ is computed as the difference between the theoretical matrix from Stokes flow theory [43, 44, 42] and the matrix as seen by the Fictitious Domain Method solver [16]: $\boldsymbol{\mathcal{R}}_{2p}^{SG} = \boldsymbol{\mathcal{R}}_{2p}^{th} - \boldsymbol{\mathcal{R}}_{2p}^{FDM}$. The procedure for computing each resistance function in $\boldsymbol{\mathcal{R}}_{2p}^{FDM}$ is explained in Appendix B.

Finally, replacing Eq. (15) in Eq. (9), a set of coupled equations involving the translational ($\mathbf{U}_p$) and angular ($\boldsymbol{\Omega}_p$) velocities of the particles is obtained, which must be solved to get the motion of the particle, together with Eqs. (1) and (2). The numerical procedure that is followed for this purpose has been explained in detail in Ref. [16] for inertial or non-inertial flows. In particular, the force density $\boldsymbol{\lambda}$ is found by a direct forcing scheme. For viscous flows, the nonlinear inertial terms are dropped and an iteration in pseudo-time of the flow is used to achieve the steady state Stokes flow result for that configuration of particles. The implementation of a similar procedure inside OpenFOAM will be addressed in Section 4.

3. Frame-invariant sub-grid correction matrix

The expression of the sub-grid correction as written in Eq. (15) is well suited to homogeneous linear flows obeying Eq. (14). However, as recalled in the introduction, it is not easily implemented when the ambient flow is not prescribed but evolves in the course of the simulation. Then, it seems mandatory to locally measure the ambient flow properties ($\mathbf{U}_0$, $\boldsymbol{\Omega}_\infty$ and $\mathbf{E}_\infty$), which raises some practical problems. In addition, as explained in detail in the following, said measuring may be unnecessary. The purpose of this section is to explain under which conditions the influence of the ambient flow $\mathbf{u}_\infty(\mathbf{x})$ may be ignored in the computation of the sub-grid corrections.

3.1. Ambient flow contribution to sub-grid corrections

The expression of the two-particle stress moments in Eq. (19) may be rearranged to separate the contributions of the particle velocities and the ambient flow:

$$-\boldsymbol{\mathcal{R}}_{2p}^{SG} \cdot \begin{pmatrix} \mathbf{U}_1 - \mathbf{u}_\infty(\mathbf{x}_1) \\ \mathbf{U}_2 - \mathbf{u}_\infty(\mathbf{x}_2) \\ \boldsymbol{\Omega}_1 - \boldsymbol{\Omega}_\infty \\ \boldsymbol{\Omega}_2 - \boldsymbol{\Omega}_\infty \\ -\mathbf{E}_\infty \\ -\mathbf{E}_\infty \end{pmatrix} = -\boldsymbol{\mathcal{R}}_{2p}^{SG} \cdot \begin{pmatrix} \mathbf{U}_1 \\ \mathbf{U}_2 \\ \boldsymbol{\Omega}_1 \\ \boldsymbol{\Omega}_2 \\ \mathbf{0} \\ \mathbf{0} \end{pmatrix} - \boldsymbol{\mathcal{R}}_{2p}^{SG} \cdot \begin{pmatrix} -\mathbf{u}_\infty^{RBM}(\mathbf{x}_1) \\ -\mathbf{u}_\infty^{RBM}(\mathbf{x}_2) \\ -\boldsymbol{\Omega}_\infty \\ -\boldsymbol{\Omega}_\infty \\ \mathbf{0} \\ \mathbf{0} \end{pmatrix} - \boldsymbol{\mathcal{R}}_{2p}^{SG} \cdot \begin{pmatrix} -\mathbf{E}_\infty \cdot \mathbf{x}_1 \\ -\mathbf{E}_\infty \cdot \mathbf{x}_2 \\ \mathbf{0} \\ \mathbf{0} \\ -\mathbf{E}_\infty \\ -\mathbf{E}_\infty \end{pmatrix} \tag{20}$$

where $\mathbf{u}_\infty^{RBM}(\mathbf{x}) = \mathbf{U}_0 + \boldsymbol{\Omega}_\infty \times \mathbf{x}$ denotes the rigid body motion (RBM) component of the ambient flow. The contribution of the ambient flow to the sub-grid correction is thus constituted by the second and third terms of the RHS of Eq. (20). The necessary condition for those terms to be omitted is that they would vanish, or that they would be far smaller than the first term.

Fortunately, rapid analysis of those terms shows that they are expected to be small by construction. The second term of Eq. (20) is the sub-grid correction for a particle pair that moves according to the RBM velocity $-\mathbf{u}_\infty^{RBM}(\mathbf{x})$ in a liquid at rest far away from the pair. In such a motion, no lubrication flow is expected to occur between the surfaces of the particles, so the flow from the solver should be close to the theoretical flow everywhere, and the stress moments should not need significant corrections. Regarding the third term, the same trends are expected: it corresponds to corrections to the stress moments for two particles at rest in a liquid in pure straining motion. Again, no lubrication flow is expected, and weak

sub-grid corrections may be needed. In a conclusion, at first sight, it seems possible to only keep the first term of the RHS of Eq. (20) as the expression of the sub-grid corrections. We thus propose to omit the second and third terms and to write the sub-grid corrections for the stress moments as:

$$\boldsymbol{\mathcal{M}}^{SG} = -\boldsymbol{\mathcal{R}}^{SG} \cdot \begin{pmatrix} \mathbf{U}_1 \\ \mathbf{U}_2 \\ \boldsymbol{\Omega}_1 \\ \boldsymbol{\Omega}_2 \end{pmatrix} \tag{21}$$

where the matrix $\boldsymbol{\mathcal{R}}^{SG}$ is identical to the matrix $\boldsymbol{\mathcal{R}}^{SG}_{2p}$, except for the two last columns that were removed.

In any case, it turns out that the expression in Eq. (21) has more fundamental implications. Due to the lack of inertia in the low-Reynolds number flows (at particle scale) that are considered here, the relation between stress moments and velocities should be frame-invariant. This is indeed the case of the general relation in Eq. (20), which involves the velocities of the particles in the reference frame attached to the liquid in rigid body motion (first and second terms of the RHS), together with the strain rate tensor $\mathbf{E}_\infty$ of the ambient flow. We recall here that the strain rate tensor of any flow is a frame-invariant quantity [45, 46]. Nonetheless, the relation in Eq. (21) may not be invariant to change of reference frame, which cannot be allowed, as the very simple and intuitive following example shows: considering a particle pair at rest in a liquid at rest, the flow solver yields a resting system, which is also the theoretical solution, and no sub-grid correction is needed for the particles at rest, in agreement with Eq. (21). Considering the same system in the reference frame that translates with the velocity $\mathbf{U}_0$ with respect to the initial frame, the flow solver now yields the velocities $-\mathbf{U}_0$ for both particles, as well as for the liquid far away from the particles, and the stress moments vector from the solver vanishes again. The sub-grid stress moments vector $\boldsymbol{\mathcal{M}}^{SG}$ is now:

$$\boldsymbol{\mathcal{M}}^{SG} = -\boldsymbol{\mathcal{R}}^{SG} \cdot \begin{pmatrix} -\mathbf{U}_0 \\ -\mathbf{U}_0 \\ \mathbf{0} \\ \mathbf{0} \end{pmatrix} \tag{22}$$

The stress moments vector in Eq. (22) must vanish, which imposes constraints to be obeyed by the components of the matrix $\boldsymbol{\mathcal{R}}^{SG}$. Should it not be the case, the sub-grid correction would introduce fake forces linearly related to the frame velocity.

The general condition for the relation in Eq. (21) to be frame-invariant can be easily expressed as follows. Assuming that the particles move with velocities ($\mathbf{U}_1$, $\mathbf{U}_2$) and angular velocities ($\boldsymbol{\Omega}_1$, $\boldsymbol{\Omega}_2$) with respect to a given reference frame, any other reference frame may be characterized by a translational velocity $\mathbf{U}_0$ and an angular velocity $\boldsymbol{\Omega}_0$, such that any point $\mathbf{x}$ at rest in this second reference frame moves with respect to the initial frame with the velocity $\mathbf{u}_{ref}(\mathbf{x}) = \mathbf{U}_0 + \boldsymbol{\Omega}_0 \times \mathbf{x}$. The condition for the relation in Eq. (21) to be frame-invariant is that for any value of $\mathbf{U}_0$ and $\boldsymbol{\Omega}_0$:

$$-\boldsymbol{\mathcal{R}}^{SG} \cdot \begin{pmatrix} \mathbf{U}_1 \\ \mathbf{U}_2 \\ \boldsymbol{\Omega}_1 \\ \boldsymbol{\Omega}_2 \end{pmatrix} = -\boldsymbol{\mathcal{R}}^{SG} \cdot \begin{pmatrix} \mathbf{U}_1 - \mathbf{u}_{ref}(\mathbf{x}_1) \\ \mathbf{U}_2 - \mathbf{u}_{ref}(\mathbf{x}_2) \\ \boldsymbol{\Omega}_1 - \boldsymbol{\Omega}_0 \\ \boldsymbol{\Omega}_2 - \boldsymbol{\Omega}_0 \end{pmatrix} \tag{23}$$

and then due to linearity:

$$-\boldsymbol{\mathcal{R}}^{SG} \cdot \begin{pmatrix} \mathbf{U}_0 + \boldsymbol{\Omega}_0 \times \mathbf{x}_1 \\ \mathbf{U}_0 + \boldsymbol{\Omega}_0 \times \mathbf{x}_2 \\ \boldsymbol{\Omega}_0 \\ \boldsymbol{\Omega}_0 \end{pmatrix} = \mathbf{0} \tag{24}$$

This last relation is completely equivalent to the vanishing of the second term in Eq. (20). As a consequence, even though this term would be proven weak, as it will be shown in the following, it should be constrained to vanish. In this respect, neglecting the third term in Eq. (20) is not of equal importance. Not accounting for the third term may induce a quantitatively imperfect computation of the sub-grid forces in

straining flow, but does not imply a violation of fundamental principles, while neglecting the second term without caution may induce the development of spurious frame-dependent forces, torques, etc., which would alter the dynamics of the particles.

In the following section, it is shown that the second and third terms in Eq. (20) may be considered weak. In the next section, the procedure that was chosen to enforce the vanishing of the second term is explained.

3.2. Estimation of ambient flow contributions

The ambient flow contribution to the sub-grid correction from Eq. (20) can be split into three independent contributions, each of which should ideally vanish, or at least be weak:

$$\boldsymbol{\mathcal{R}}_{2p}^{SG} \cdot \begin{pmatrix} \mathbf{U}_0' \\ \mathbf{U}_0' \\ \mathbf{0} \\ \mathbf{0} \\ \mathbf{0} \\ \mathbf{0} \end{pmatrix} + \boldsymbol{\mathcal{R}}_{2p}^{SG} \cdot \begin{pmatrix} -\boldsymbol{\Omega}_\infty \times \dfrac{r\mathbf{d}}{2} \\ \boldsymbol{\Omega}_\infty \times \dfrac{r\mathbf{d}}{2} \\ \boldsymbol{\Omega}_\infty \\ \boldsymbol{\Omega}_\infty \\ \mathbf{0} \\ \mathbf{0} \end{pmatrix} + \boldsymbol{\mathcal{R}}_{2p}^{SG} \cdot \begin{pmatrix} -\mathbf{E}_\infty \cdot \dfrac{r\mathbf{d}}{2} \\ \mathbf{E}_\infty \cdot \dfrac{r\mathbf{d}}{2} \\ \mathbf{0} \\ \mathbf{0} \\ \mathbf{E}_\infty \\ \mathbf{E}_\infty \end{pmatrix} = \mathbf{0} \tag{25}$$

where $\mathbf{U}_0' = \mathbf{U}_0 + \boldsymbol{\Omega}_\infty \times \dfrac{\mathbf{x}_1 + \mathbf{x}_2}{2} + \mathbf{E}_\infty \cdot \dfrac{\mathbf{x}_1 + \mathbf{x}_2}{2}$, $r = \|\mathbf{x}_2 - \mathbf{x}_1\|$ and $r\mathbf{d} = \mathbf{x}_2 - \mathbf{x}_1$.

The various terms in Eq. (25) correspond to the sub-grid corrections for, respectively, a translation of the particle pair with velocity $-\mathbf{U}_0'$ in an otherwise resting liquid, a rigid body rotation of the pair with angular velocity $-\boldsymbol{\Omega}_0$, and a particle pair at rest in a straining flow with strain rate tensor $\mathbf{E}_\infty$. We note that the decomposition in Eq. (25) is not unique, since the particular point $(\mathbf{x}_1 + \mathbf{x}_2)/2$ is arbitrary. Nevertheless, it allows easier algebra while, due to linearity, the various expressions that are deduced do not depend on this particular point. Systematic cancellation of each term yields a set of linear equations with the matrix coefficients as unknowns. The whole set of relations that follows from Eq. (25) is quoted in Appendix C.1. As an example of such a relation, the sub-grid force exerted on particle (p_1) due to pair translation along the line of centers with velocity $\mathbf{U}_0'$ should vanish (Fig. 1a):

$$\mathbf{F}_1^{SG} = -\eta \left(X_{11}^{A,SG} + X_{12}^{A,SG} \right) \mathbf{U}_0' = \mathbf{0} \tag{26}$$

where the scalar coefficients $X_{11}^{A,SG}$ and $X_{12}^{A,SG}$ only depend on the distance between the particles and their radii (see Appendix A). Since the two-particle sub-grid resistance matrix is the difference between the theoretical two-particle matrix and the FDM solver matrix, Eq. (26) may be written as:

$$X_{11}^{A,FDM} + X_{12}^{A,FDM} = X_{11}^{A,th} + X_{12}^{A,th} \tag{27}$$

which means that the solver should properly account for the force due to the translation of the pair without the need for any correction.

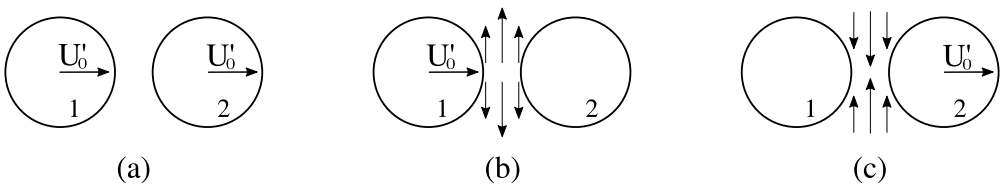

Fig. 1. Sketch of a particle pair translating with velocity $\mathbf{U}_0'$. (a) Translation of the whole pair. Decomposition of the motion in (b) (respectively (c)) a translation of particle 1 (resp. 2) while particle 2 (resp. 1) is at rest.

Thus, the validity of Eq. (26) is easily checked by comparing the two sides of Eq. (27). In Fig. 2a, the LHS of Eq. (27) (FDM resistance coefficient) is displayed as a function of the reduced distance between particle surfaces $\xi = 2\|\mathbf{x}_2 - \mathbf{x}_1\| / (a_1 + a_2) - 2$ for a pair of particles of the same radius a, together with its theoretical counterpart. The agreement is very good, as also shown in Fig. 2b where the relative difference between the two terms is displayed. It should be stressed here that each of the resistance coefficients, X_{11}^A or X_{12}^A, takes very different values, whether the FDM coefficient or the theoretical one is considered, especially in the low distance range.

Indeed, in Fig. 2c, $X_{11}^{A,th}$ is shown to diverge as ξ tends to 0. Since $X_{11}^{A,th}$ accounts for the force exerted on particle (p_1) as it moves, while particle (p_2) is kept at rest, its high value reflects the lubrication flow that occurs between the particles (Fig. 1b). The corresponding FDM coefficient $X_{11}^{A,FDM}$ takes values very close to $X_{11}^{A,th}$ as soon as the distance between the particle surfaces exceeds a distance typically equal to the mesh size Δ (see the upper axis in Fig. 2), but does not diverge at contact. This was indeed expected since the solver cannot account for the lubrication flow between the particle surfaces. The same discrepancy is observed for the coefficient X_{12}^A (Fig. 2d) due to a lubrication flow in the opposite direction to the former, as only particle (p_2) moves (Fig. 1c). Despite these large discrepancies, the sum of the coefficients $X_{11}^A + X_{12}^A$ from the FDM computations or the theory yields very close values. This agreement may be qualitatively understood, considering that no lubrication flow develops between the surfaces of the particles as the particles move as a rigid pair (Fig. 1a). For that reason, the sum of the theoretical resistance coefficients, which accounts for the viscous force on particle (p_1), does not diverge as ξ tends to 0, but smoothly decreases (Fig. 2a). In the same line, since the flow between particles is weak, most of the force exerted on particle (p_1) originates in the flow outside the gap, which is correctly computed by the FDM solver, and the sub-grid corrections are not needed. Nevertheless, considering that the theoretical values of X_{11}^A or X_{12}^A are very large compared to their FDM counterpart in the low range of ξ, and that their sum is quite small compared to the individual FDM values, keeping also in mind that $X_{11}^{A,FDM}$ and $X_{12}^{A,FDM}$ have been computed separately, the agreement between $X_{11}^{A,FDM} + X_{12}^{A,FDM}$ and $X_{11}^{A,th} + X_{12}^{A,th}$ is remarkable, and highlights the great quality of the Fictitious Domain Method. The same comparison has been carried out for each relation in Appendix C.1. The symmetry of the FDM resistance matrix following from Lorentz reciprocal theorem (Appendix A) has been checked in the same way. Each relation has been found to hold to within a few percent. Therefore, the third term of the RHS in Eq. (20) is simply removed. For the second terms to be removed and the sub-grid corrections to be written as in Eq. (21), the matrix $\boldsymbol{\mathcal{R}}^{SG}$ must be modified in such a way that the relations in Appendix C.1 rigorously hold. This is explained now.

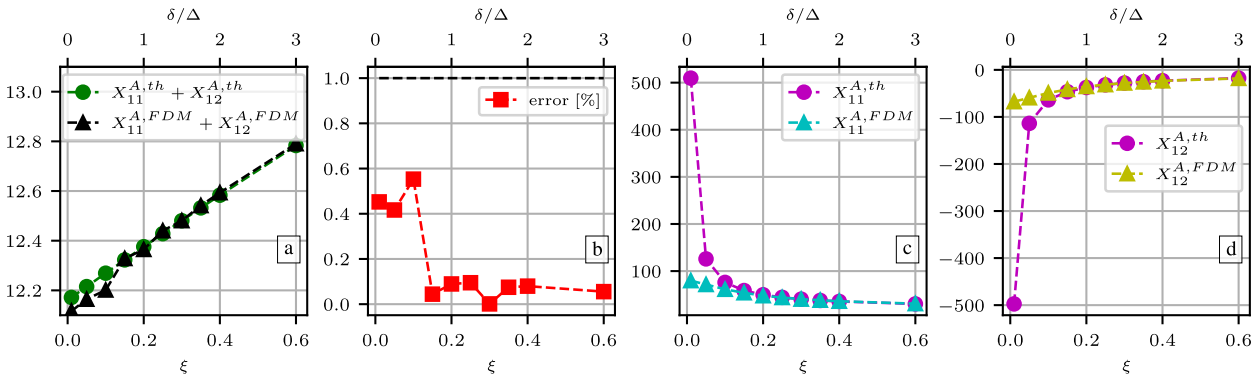

Fig. 2. Comparison between the resistance coefficients as measured by the FDM and as predicted by the lubrication theory for the force exerted on particle (p_1), when the particle pair moves rigidly along the center line, $X_{11}^A + X_{12}^A$, as a function of the reduced distance between the particle surfaces $\xi = 2\|\mathbf{x}_2 - \mathbf{x}_1\| / (a_1 + a_2) - 2$. (a) $X_{11}^{A,FDM} + X_{12}^{A,FDM}$ and $X_{11}^{A,th} + X_{12}^{A,th}$. (b) The relative difference between the terms in Fig a. (c) $X_{11}^{A,FDM}$ and $X_{11}^{A,th}$. (d) $X_{12}^{A,FDM}$ and $X_{12}^{A,th}$. The upper scale shows the ratio of the distance between particle surfaces, δ, to the mesh size Δ. $a_1 = a_2 = a$ and $a/\Delta = 5$.

3.3. Building a frame-invariant sub-grid correction matrix

The idea of a frame-invariant resistance matrix is not new. Such a property has been indeed sought for the hydrodynamic resistance matrix in earlier work from the literature. Ball and Melrose (1997) [47] performed molecular dynamics simulations of Brownian suspensions. They compute the total resistance matrix of hydrodynamic interactions as the superposition of two-particle resistance matrices that obey Eq. (21). To this purpose, the motion of the particles is computed in the co-rotational frame, i.e. the frame attached to the line that joins the centers of the particles. Doing this, they only consider the internal motion modes corresponding to lubrication flow, i.e. squeeze, shear, pump, and twist, and they pick the relevant matrix coefficients from lubrication theory. It should be noted that choosing a sub-grid correction matrix that obeys Eq. (25) is formally equivalent to correcting only the above-mentioned internal motion modes. Their model has been extensively used, and it has been implemented in the molecular dynamics toolbox LAMMPS [48, 24]. The computation of the hydrodynamic forces does not originally involve any ambient flow [47], although a drag force proportional to the difference between the particle velocity and the ambient flow velocity is often added [23]. It neither explicitly accounts for many-body long-range hydrodynamic interactions.

This idea of a frame-invariant correction matrix has also been found important in the frame of the so-called Stokesian Dynamics method [2, 3]. In this method, the long-range hydrodynamic interactions are accounted for using a multipole expansion, supplemented by lubrication corrections in the form of a correction matrix, in a way that inspired the later lubrication-corrected methods, including the one described here. In Ref. [49], Cichocki et al. (1999) note that a correction matrix in the form of Eq. (21) may not only involve the relative motion of the particles inside a particle pair, which is responsible for the so-called lubrication interactions, but also the collective motion of the particles. To keep only the lubrication interactions and get rid of the influence of the collective motion, they build a modified correction matrix from the raw matrix, using a convenient projection. Their purpose is very similar to the one followed in this section since our objective is to modify the matrix $\boldsymbol{\mathcal{R}}^{SG}$ so that a particle pair in rigid body motion, i.e. undergoing collective motion, may yield no sub-grid corrections. Then, only the deviation of the motion of the particles from a rigid body motion will induce sub-grid corrections. Finally, Cichocki et al. (1999) show that using a correction matrix where the collective motion is not projected out results in an erroneous computation of the three-particles contribution to the translational short-time self-diffusion in Brownian suspensions. The explanation that they provide is akin to the simple example that was given in Section 3.1: the translation of a close particles pair results in a spurious lubrication force on the pair, which induces a slow decaying stokeslet flow proportional to the inverse of the distance from the pair. The authors show that this results in the divergence of the translational self-diffusion coefficient.

In the current study, the raw sub-grid matrix is modified differently compared to the method explained in Ref. [49]. It should first be recalled that the matrix $\boldsymbol{\mathcal{R}}^{SG}$ in Eq. (21) is identical to the matrix $\boldsymbol{\mathcal{R}}_{2p}^{SG}$ in Eq. (19), except for the two last columns that were suppressed. As a consequence, we are mainly interested in the functions defining the tensors $\mathbf{A}$, $\mathbf{B}$, $\mathbf{C}$, $\mathbf{G}$, $\mathbf{H}$ and $\mathbf{P}$, but $\tilde{\mathbf{G}}$ and $\tilde{\mathbf{H}}$ have to be tackled as well due to the symmetry relation resulting from the Lorenz's reciprocal theorem. The corresponding part of the matrix involves 52 resistance functions (see Appendix A.1). There are 20 symmetry relations between these functions due to Lorentz's reciprocal theorem, resulting in 32 independent functions. Now there are 26 linear relations involving the functions of interest imposed by the cancellation of each of the independent terms of Eq. (25). These relations are quoted in Appendix C.1. However, they are not linearly independent from the previous equations. In conclusion, we expect only 10 independent resistance functions for the frame-invariant sub-grid correction matrix. We choose one function among each group of similar functions, namely X_{21}^A, Y_{21}^A, Y_{21}^B, X_{21}^C, Y_{11}^C, X_{11}^G, Y_{11}^G, Y_{21}^H, X_{21}^P, X_{12}^P. The remaining functions are expressed as a function of the 10 base functions, as detailed in Appendix C.2. It should be noted that the strong reduction in the number of independent functions is consistent with the approaches developed in Refs. [47, 49]: since such a frame-invariant correction matrix only accounts for the internal motion mode to the exclusion of collective (rigid body) motion, fewer functions are needed.

Finally, the theoretical expressions of the 10 chosen functions from low-Reynolds number flow theory may be found in Refs. [43, 44, 42, 50]. They are recalled in the Supplementary Material, as are the corresponding theoretical expressions for the particle-wall resistance functions.

4. Numerical implementation

This section deals with the method that is followed to solve Eq. (9). As mentioned above, particle and fluid inertia is assumed irrelevant, so the corresponding terms in the equations are removed. It should be stressed that this step is not mandatory and that the method is also convenient for finite Reynolds number flows [16]. The simplified equations are quoted below:

$$\mathbf{0} = \boldsymbol{\nabla} \cdot \left(\frac{\eta}{\rho_f} \left(\boldsymbol{\nabla}\mathbf{u} + \boldsymbol{\nabla}\mathbf{u}^T \right) \right) - \frac{\boldsymbol{\nabla} p}{\rho_f} + \boldsymbol{\lambda} \tag{28a}$$

$$\boldsymbol{\nabla} \cdot \mathbf{u} = 0 \tag{28b}$$

$$\mathbf{u}(\mathbf{x}) = \mathbf{U}_p + \boldsymbol{\Omega}_p \times (\mathbf{x} - \mathbf{x}_p) \ \text{ in } \mathcal{D}_p \tag{28c}$$

$$\mathbf{0} = \frac{\rho_p - \rho_f}{\rho_p} M_p \mathbf{g} - \rho_f \int_{\mathcal{D}_p} \boldsymbol{\lambda} \mathrm{d}\mathcal{V} + \mathbf{F}_p^{SG} + \mathbf{F}_p^{c} + \mathbf{F}_p^{ext} \tag{28d}$$

$$\mathbf{0} = -\rho_f \int_{\mathcal{D}_p} (\mathbf{x} - \mathbf{x}_p) \times \boldsymbol{\lambda} \mathrm{d}\mathcal{V} + \mathbf{T}_p^{SG} + \mathbf{T}_p^{c} + \mathbf{T}_p^{ext} \tag{28e}$$

In the following, the particles are assumed spherical, so that the inertia tensor amounts to a scalar quantity. The latter quantity is not explicitly part of the equations at this stage but will be reintroduced in the course of the resolution. The solution method has been explained in detail in Ref. [16]. The main points of the method will be briefly recalled in the following, together with its implementation in the frame of the OpenFOAM toolbox. Eq. (28) are solved iteratively for each time step. Each iteration starts with the determination of the pressure and incompressible velocity fields using the force density at the previous step. Then, the velocities of the particles are computed, the rigid body motion is enforced inside the particles and the force density is corrected accordingly. This procedure is repeated until convergence.

4.1. Fluid sub-problem

The fluid Eqs. (28a) and (28b) are solved over the whole domain using the finite volume method toolbox OpenFOAM on a fixed Cartesian grid with a constant grid spacing Δ. The discretization of the momentum equation for an incompressible flow is a standard procedure in OpenFOAM [51, 52]. In addition to the discretized velocity equation from Eq. (28a), a pressure equation is derived from Eqs. (28a) and (28b), whose solution allows computation of the new incompressible velocity field. A cell-centerd collocated grid is used for the pressure and velocity fields, and the pressure equation is built using a Rhie-Chow interpolation to prevent checkerboard instability.

The pressure-momentum coupling is dealt with using the PISO (Pressure Implicit with Splitting of Operators) procedure originally proposed by Issa (1986) [53]. The discretized implicit velocity equation is first solved, using the pressure and force density fields from the previous iteration. In a further step, the pressure equation is solved and the velocity field is corrected accordingly to the new pressure. The latter step is performed twice to improve consistency between pressure and velocity.

At the end of the PISO step, the velocity field, denoted by $\mathbf{u}^*$, is divergence-free but not perfectly rigid inside the particles, as the forcing at the previous iteration $\boldsymbol{\lambda}^n$ has been used (more details in the next section). The particle velocities $\mathbf{U}_p^{n+1}$ and $\boldsymbol{\Omega}_p^{n+1}$ must be determined, and the rigid body motion enforced inside the particles and the force density corrected accordingly.

It is worth noting that the equation for the fluid flow (Eq. (28a)) together with Eq. (28b) are quite different from the standard equations usually tackled in OpenFOAM: no inertia is accounted for, so that the lacking convective momentum transport is not a source of nonlinearity. In addition, only steady equations are considered, so that, except for the force density $\boldsymbol{\lambda}$ inside the particles, the equations are linear. Anyway, the main difficulty is the determination of the distribution of $\boldsymbol{\lambda}$, so that Eqs. (28c) and (28e) are fulfilled. This issue is addressed in the following sections.

4.2. Particle sub-problem

The particle sub-problem is three-fold: first, constrain a rigid body motion inside the particles; second, compute the velocities of the particles; and third, update the forcing term $\boldsymbol{\lambda}$. As previously stressed, the fluid velocity $\mathbf{u}^*$ does not exactly comply with a rigid body motion inside particles because the forcing term $\boldsymbol{\lambda}^n$ is taken at the previous time step.

Anyway, the particles velocities $\mathbf{U}_p^{n+1}$ and $\boldsymbol{\Omega}_p^{n+1}$ are still unknown at this stage. We assume that the correction of the force density field $\boldsymbol{\lambda}$ reads [16]:

$$\boldsymbol{\lambda}^{n+1} = \boldsymbol{\lambda}^n + \frac{\mathbf{U}_p^{n+1} + \boldsymbol{\Omega}_p^{n+1} \times (\mathbf{x} - \mathbf{x}_p) - \mathbf{u}^*}{\alpha_\lambda} \qquad \text{inside} \quad \mathcal{D}_p \tag{29}$$

where α_λ has the dimension of time, and has the role of a penalty parameter for the direct forcing. It is given the value of the momentum diffusion time at the scale of a mesh size Δ: $\alpha_\lambda = \Delta^2 \rho_f / \eta$.

Using Eq. (29) into Eqs. (28d) and (28e) yields the following equations that must be solved for the velocities of the particles ${\mathbf{U}_\mathbf{p}}^{n+1}$ and ${\boldsymbol{\Omega}_\mathbf{p}}^{n+1}$:

$$\begin{aligned}
\frac{\rho_f}{\rho_p} M_p \mathbf{U}_p^{n+1} &= \frac{\rho_p - \rho_f}{\rho_p} M_p \mathbf{g} \alpha_\lambda + \rho_f \int_{\mathcal{D}_p} (\mathbf{u}^* - \boldsymbol{\lambda}^n \alpha_\lambda) \, \mathrm{d}\mathcal{V} + \left(\mathbf{F}_p^{SG} + \mathbf{F}_p^c + \mathbf{F}_p^{ext} \right) \alpha_\lambda \\
\frac{\rho_f}{\rho_p} \mathbf{J}_p \cdot \boldsymbol{\Omega}_p^{n+1} &= \rho_f \int_{\mathcal{D}_p} (\mathbf{x} - \mathbf{x}_p) \times (\mathbf{u}^* - \boldsymbol{\lambda}^n \alpha_\lambda) \, \mathrm{d}\mathcal{V} + \left(\mathbf{T}_p^{SG} + \mathbf{T}_p^c + \mathbf{T}_p^{ext} \right) \alpha_\lambda
\end{aligned} \tag{30}$$

It should be stressed here that the L.H.S. of Eq. (30) does not originate in inertia, which is fully neglected, but instead is a consequence of the correction of the force density, which is computed from the unknown particle velocity $\mathbf{U}_p^{n+1}$ according to Eq. (29). As explained above, the sub-grid forces and torques depend on the unknown velocities $\mathbf{U}_p^{n+1}$ and $\boldsymbol{\Omega}_p^{n+1}$. From Eq. (21) and Eq. (30), the set of linear equations that must be solved for the particle velocities reads:

$$\left[\frac{\rho_f}{\rho_p} \frac{\boldsymbol{\mathcal{J}}}{\alpha_\lambda} + \boldsymbol{\mathcal{R}}^{SG} \right] \cdot \boldsymbol{\mathcal{U}}^{n+1} = \boldsymbol{\mathcal{F}}^{tot} \tag{31}$$

where $\boldsymbol{\mathcal{J}}$ is the diagonal matrix accounting for the particle masses and inertia moments, $\boldsymbol{\mathcal{R}}^{SG}$ is the sub-grid resistance matrix for the frame-invariant lubrication correction, $\boldsymbol{\mathcal{U}}^{n+1}$ is the vector of the particles translational and angular velocities, and $\boldsymbol{\mathcal{F}}^{tot}$ is the generalized force vector that reads:

$$\boldsymbol{\mathcal{F}}^{tot} = \begin{pmatrix}
\dfrac{\rho_p - \rho_f}{\rho_p} M_1 \mathbf{g} + \rho_f \displaystyle\int_{\mathcal{D}_1} \left(\frac{\mathbf{u}^*}{\alpha_\lambda} - \boldsymbol{\lambda}^n \right) \mathrm{d}\mathcal{V} + \mathbf{F}_1^c + \mathbf{F}_1^{ext} \\
\dfrac{\rho_p - \rho_f}{\rho_p} M_2 \mathbf{g} + \rho_f \displaystyle\int_{\mathcal{D}_2} \left(\frac{\mathbf{u}^*}{\alpha_\lambda} - \boldsymbol{\lambda}^n \right) \mathrm{d}\mathcal{V} + \mathbf{F}_2^c + \mathbf{F}_2^{ext} \\
\cdots \\
\cdots \\
\rho_f \displaystyle\int_{\mathcal{D}_1} (\mathbf{x} - \mathbf{x}_p) \times \left(\frac{\mathbf{u}^*}{\alpha_\lambda} - \boldsymbol{\lambda}^n \right) \mathrm{d}\mathcal{V} + \mathbf{T}_1^c + \mathbf{T}_1^{ext} \\
\rho_f \displaystyle\int_{\mathcal{D}_2} (\mathbf{x} - \mathbf{x}_p) \times \left(\frac{\mathbf{u}^*}{\alpha_\lambda} - \boldsymbol{\lambda}^n \right) \mathrm{d}\mathcal{V} + \mathbf{T}_2^c + \mathbf{T}_2^{ext}
\end{pmatrix} \tag{32}$$

At this stage, an explicit forcing of the rigid body motion is thus possible:

$$\begin{aligned}
\mathbf{u}^{n+1} &= \mathbf{U}_p^{n+1} + \boldsymbol{\Omega}_p^{n+1} \times (\mathbf{x} - \mathbf{x}_p) \quad \text{inside } \mathcal{D}_p \\
\mathbf{u}^{n+1} &= \mathbf{u}^* \qquad\qquad\qquad\qquad\quad \text{outside } \mathcal{D}_p
\end{aligned} \tag{33}$$

and the force density is corrected according to Eq. (29). We note here that the resistance function in the sub-grid correction matrix diverges as the distance between particle surfaces, or between particle surface and wall, tends to zero. To keep the linear system in Eq. (31) reasonably well conditioned, a threshold (10^{-5}) is imposed on the reduced distances $\xi = 2r/(a_1+a_2)-2$ and $\varepsilon = r/a-1$, below which the resistance functions are kept constant.

4.3. Algorithm

Here follows the numerical algorithm implemented in OpenFOAM:

1. Update the positions of the particles $\mathbf{x}_p$: move the particles using their velocity.
2. Truncate the force density field from previous iteration, i.e. set $\boldsymbol{\lambda} = \mathbf{0}$ outside the particles.
3. Solve the fluid sub-problem: solve the pressure-momentum coupling problem using the forcing term of the previous correction step $\boldsymbol{\lambda}^n$, obtaining $\mathbf{u}^*$ and p^{n+1}.
4. Solve Eq. (31) with Eq. (32) for the particles velocities $\mathbf{U}_p^{n+1}$ and $\boldsymbol{\Omega}_p^{n+1}$.
5. Compute the new forcing term $\boldsymbol{\lambda}^{n+1}$ using Eq. (29).
6. Compute the new velocity field $\mathbf{u}^{n+1}$: correct the velocity field $\mathbf{u}^*$ by enforcing the particles rigid body motion (Eq. (33)).
7. Repeat steps 3, 4, 5, and 6 until convergence of $\boldsymbol{\lambda}$.
8. Proceed to the next time step and repeat.

The reader should note that steps 5 and 6 are independent and switchable. Step 2 is needed to guarantee the absence of the force density $\boldsymbol{\lambda}$ outside the particles; alternatively, $\boldsymbol{\lambda}$ could be advected using the velocity field $\mathbf{u}$. This is at the cost of too much numerical diffusion so the advection step has been discarded.

4.4. Numerical details

We present here the discretization schemes and the boundary conditions employed. We also show a parallelization technique for the treatment of the particles that matches the decomposition method proposed by OpenFOAM. Then, we proceed with the choice of the indicator functions used to compute the required integrals over the volume of the particles. Regarding the dimensions of the particles, we employ two radius lengths $a_1 = 1.0$ and $a_2 = 1.4$, to avoid particle ordering usually observed in concentrated mono-disperse systems [54, 55, 56]; all lengths are normalized by a_1. As for the influence of the mesh size Δ compared to the particle radius, it has been studied before by Gallier et al. (2014) [16], and in the following the value $\Delta = a_1/5$ will not be changed. Finally, we discuss the influence of the tolerances that need to be set.

4.4.1. Numerical schemes and boundary conditions

OpenFOAM employs the Finite Volume Method, which is a numerical technique that transforms the partial differential equations representing conservation laws over differential volumes into discrete algebraic equations over finite volumes. This method is strictly conservative, which makes it a popular method in CFD [52]. To perform the required spatial and temporal discretization of the equations, OpenFOAM proposes multiple schemes. We use a standard Gaussian integration scheme supplemented by linear interpolation for the computation of the face values from the cell center values; for the computation of surface-normal gradient terms, we employ an orthogonal (i.e., non-corrected) scheme, which guarantees a second-order accurate calculation for regular meshes such as the one we use. OpenFOAM proposes various built-in boundary conditions for the velocity and pressure fields. We use the *cyclic* condition in the case of periodic boundary conditions; if a wall is present, we use the *fixedValue* condition for $\mathbf{u}$ imposing the corresponding velocity or a *slip* condition if a velocity different than the wall is needed, and the *fixedFluxPressure* condition for p, which sets the pressure gradient for the volume flux on the boundary to be consistent with the velocity boundary condition.

4.4.2. Parallelization

Parallelization is handled via the domain decomposition method proposed in OpenFOAM: the principle is to break up the domain – geometry and fields – into physical sub-sets and allocate each part to a different CPU. The information is then shared using the standard MPI. Building up from this method, we carry out the parallelization of the particles following the same concept: each process manages the particles inside the corresponding domain together with the particles in the neighboring domains that may interact with them, so that part of the particles is shared by multiple processes. Lubrication and contact interactions require listing the particle pairs: each process performs this task for the particles hosted in its domain and builds the local resistance matrix. Finally, the local matrices are collected by the master process for the inversion of the linear system of Eq. (31). Delegating the resolution of Eq. (31) to the master process using the linear algebra library Eigen [57] was found faster than solving it in parallel using the local matrices with message-passing between the interacting processes. Further speedup of the latter part can be obtained by exploiting the multi-threading available in Eigen.

4.4.3. Indicator functions

Non-boundary-fitted Eulerian methods are attractive since a fixed mesh avoids any re-meshing difficulties and computational costs. Nevertheless, the interface between fluid and particles is critical and must be defined properly. This issue is made simpler here because only rigid particles are considered, and their shape consequently remains unchanged. The particle tracking is needed to define and distinguish the particle region $\mathcal{D}_p$ from the fluid domain $\mathcal{D}_f$. The chosen method rests on the level-set approach, which considers a level-set function $\mathcal{I}_\mathcal{P}(\mathbf{x})$ equal to 1 inside the particles and 0 outside, with a smeared interface, defined as:

$$\mathcal{I}_\mathcal{P} = \frac{1}{2}\left[1 - \tanh\left(b\frac{s}{\Delta}\right)\right] \tag{34}$$

where $s = \|\mathbf{x} - \mathbf{x}_p\| - a_p$, Δ is the grid spacing and b is a free parameter controlling the smearing on a typical size $\sim \mathcal{O}(\Delta/b)$. The level-set function $\mathcal{I}_\mathcal{P}(s)$ is then used to compute the particle mass, volume, and inertia tensor as well as any integral of a quantity ϕ on the particle volume $\mathcal{P}$:

$$\int_{\mathcal{D}_p} \phi \mathrm{d}\mathcal{V} = \int_\mathcal{D} \mathcal{I}_\mathcal{P}(\mathbf{x})\phi(\mathbf{x})\mathrm{d}\mathcal{V} \tag{35}$$

The correction of the force density field $\boldsymbol{\lambda}$ (Eq. (29)) and the forcing of the rigid body motion of the particles (Eq. (33)) require an indicator function as well. Finally, we use two different indicator functions:

- $\mathcal{I}_u(\mathbf{x})$ is used to impose the rigid body motion inside the particles and compute the integrals in which the velocity field is involved, in particular, the computation of M_p and J_p;
- $\mathcal{I}_\lambda(\mathbf{x})$ is used to increment the force density field $\boldsymbol{\lambda}$ and to compute the integrals in which the force density $\boldsymbol{\lambda}$ is involved.

We find that the best choice for $\mathcal{I}_\lambda$ is a steep Heaviside function defined as:

$$\mathcal{I}_\lambda(\mathbf{x}) = \begin{cases} 1 & \text{if } \|\mathbf{x} - \mathbf{x}_p\| \leq a_p + c\Delta \\ 0 & \text{if } \|\mathbf{x} - \mathbf{x}_p\| > a_p + c\Delta \end{cases} \tag{36}$$

and for $\mathcal{I}_u$ a smooth indicator function defined as:

$$\mathcal{I}_u(\mathbf{x}) = \begin{cases} \frac{1}{2}\left[1 - \tanh\left(b\frac{s}{\Delta}\right)\right] & \text{if } \|\mathbf{x} - \mathbf{x}_p\| \leq a_p + c\Delta \\ 0 & \text{if } \|\mathbf{x} - \mathbf{x}_p\| > a_p + c\Delta \end{cases} \tag{37}$$

See Fig. 3 for an example of the indicator functions.

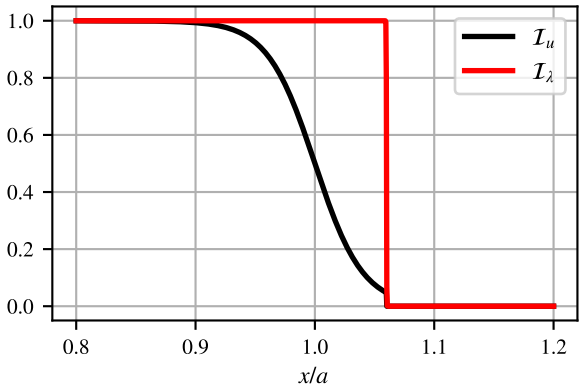

Fig. 3. Indicator functions $\mathcal{I}_\lambda(\mathbf{x})$ and $\mathcal{I}_u(\mathbf{x})$ from Eqs. (36) and (37) with $b = 5$ and $c = 0.3$.

Using the indicator functions, Eqs. (29), (30) and (33) write:

$$
\begin{aligned}
&\frac{\rho_f}{\rho_p} M_p \mathbf{U}_p^{n+1} = \frac{\rho_p - \rho_f}{\rho_p} M_p \mathbf{g} \alpha_\lambda + \rho_f \int_{\mathcal{D}} \left[\mathcal{I}_u(\mathbf{x}) \mathbf{u}^*(\mathbf{x}) - \mathcal{I}_\lambda(\mathbf{x}) \boldsymbol{\lambda}^n(\mathbf{x}) \alpha_\lambda\right] \mathrm{d}\mathcal{V} + \left(\mathbf{F}_p^{SG} + \mathbf{F}_p^c + \mathbf{F}_p^{ext}\right) \alpha_\lambda \\
&\frac{\rho_f}{\rho_p} J_p \boldsymbol{\Omega}_p^{n+1} = \rho_f \int_{\mathcal{D}} (\mathbf{x} - \mathbf{x}_p) \times \left[\mathcal{I}_u(\mathbf{x}) \mathbf{u}^*(\mathbf{x}) - \mathcal{I}_\lambda(\mathbf{x}) \boldsymbol{\lambda}^n(\mathbf{x}) \alpha_\lambda\right] \mathrm{d}\mathcal{V} + \left(\mathbf{T}_p^{SG} + \mathbf{T}_p^c + \mathbf{T}_p^{ext}\right) \alpha_\lambda \\
&\boldsymbol{\lambda}^{n+1}(\mathbf{x}) = \boldsymbol{\lambda}^n(\mathbf{x}) + \mathcal{I}_\lambda(\mathbf{x}) \frac{\mathbf{U}_p^{n+1} + \boldsymbol{\Omega}_p^{n+1} \times (\mathbf{x} - \mathbf{x}_p) - \mathbf{u}^*(\mathbf{x})}{\alpha_\lambda} \\
&\mathbf{u}^{n+1}(\mathbf{x}) = \mathbf{u}^*(\mathbf{x}) + \mathcal{I}_u(\mathbf{x}) \left[\mathbf{U}_p^{n+1} + \boldsymbol{\Omega}_p^{n+1} \times (\mathbf{x} - \mathbf{x}_p) - \mathbf{u}^*(\mathbf{x})\right]
\end{aligned}
\tag{38}
$$

Mainly, the indicator function $\mathcal{I}_u$ controls to what extent the velocity inside the particle is set to rigid body motion, and connects the particle velocity and angular velocity to the underlying liquid velocity field. The indicator function $\mathcal{I}_\lambda$ allows the force density felt by the liquid to be properly transmitted to the particles. Some comments on the choice of the form of the different indicator functions may be useful:

- due to the small parameter $c > 0$, the actual size of the particle is slightly larger than the theoretical size a_p. Should it not be the case, the hydrodynamic resistance coefficients on a sphere would be underestimated, as shown below in the particular case of the drag on a cubic lattice of particles. The parameters b and c in Eqs. (36) and (37) have to be tuned, as explained in Section 4.4.4;
- the integral of the force density over each particle directly defines the force and torque felt by the particle (Eq. (6)). From physical sound arguments, it seems important that the total force on the liquid has to be equal to the sum of all forces F_p^{FDM}. This is the reason for using a steep Heaviside function for the integration of $\boldsymbol{\lambda}$;
- for the same reason, since the indicator functions $\mathcal{I}_\lambda$ of two close particles may overlap, they are given the value 0.5 at overlapping positions;
- the indicator function $\mathcal{I}_u$ used in the computation of M_p, J_p, $\int \mathbf{u}^*(\mathbf{x})\mathrm{d}\mathcal{V}$ has been given a smooth shape to limit the oscillations of these quantities due to the finite mesh-size Δ;
- choosing a smooth function to increment $\boldsymbol{\lambda}$ results in a decrease of the convergence rate.

4.4.4. Choice of the parameters for the indicator functions

We can now tune the parameters b and c that determine the shape of the indicator functions $\mathcal{I}_u$ and $\mathcal{I}_\lambda$ (Eqs. (36) and (37)). We measure the drag coefficient K (Eq. (40)) of a translating periodic array of spheres averaged over 64 positions evenly distributed inside a single mesh cell in a domain of size $L/a = 8$ by varying b and c. The different tolerances are now set to $\mathrm{tol}_p = 5 \cdot 10^{-6}$, $\mathrm{tol}_u = 10^{-6}$, and $\mathrm{tol}_\lambda = 10^{-4}$ except for the first position for which we set $\mathrm{tol}_\lambda = 10^{-5}$. This choice is justified in the next section, and a full study of

the convergence is proposed in the Supplementary Material. The flow geometry, boundary conditions, etc. are described in detail in Section 5.1.

The parameter c seems to have the most important role, as it sets the actual size of the particle, i.e the precise spatial zone where $\boldsymbol{\lambda}$ is computed. On the contrary, the parameter b sets the smoothness of the indicator function $\mathcal{I}_u$, and has a role of *smoother* of some of the quantities as the particle moves through the mesh; in addition, we recall that the indicator function $\mathcal{I}_\lambda$ used to increment $\boldsymbol{\lambda}$ is a discontinuous Heaviside function for which only c is relevant.

We first let b vary while keeping $c = 0.3$: as we can observe in Table 1, K keeps nearly constant, and so does its standard deviation σ_K. This is at first sight surprising since the role of a smooth indicator function is to limit the oscillations of particle quantities as it moves across the mesh. Nonetheless, although not shown here, other quantities such as the particle mass do oscillate as the particle moves across the mesh, and the oscillations are all the more intense as the indicator function $\mathcal{I}_u$ is steep. Nevertheless, too smooth an indicator function is not convenient either. Indeed, $\mathcal{I}_u$ is forced to vanish at $\|\mathbf{x} - \mathbf{x}_p\| = a_p + c\Delta$ (Eq. (37) and Fig. 3), so that a smaller value of b induces a larger discontinuity of $\mathcal{I}_u$. $b = 5$ turns out to be a satisfactory compromise and is also the value that has been used in previous works [16]. The influence of the parameter c is now probed while keeping $b = 5$ fixed. As displayed in Table 2, $c = 0.3$ yields the value of $\langle K \rangle$ closest to the theoretical value. In Fig. 3 we represent the indicator function with the optimal parameters.

Table 1
Drag coefficient of a translating periodic array of spheres for different values of the parameter b of the indicator function $\mathcal{I}_u$, averaged over 64 positions in a single mesh cell and standard deviation.

b $(c = 0.3)$	$\langle K \rangle$	σ_K
2	1.532135	0.014381
5	1.532059	0.014380
7	1.532041	0.014387
10	1.532030	0.014399

Table 2
Drag coefficient of a translating periodic array of spheres for different values of the parameter c of the indicator functions, mean over 64 positions in a single mesh cell.

c $(b = 5)$	$(\langle K \rangle - K_{th})/K_{th}$ [%]
0.10	-5.69
0.20	-3.01
0.25	-1.27
0.30	0.11
0.35	1.47
0.40	3.25
0.50	6.09

4.4.5. Convergence control

We used the same setup as the one of the previous section (that is described in detail in Section 5.1) to investigate the role of the tolerances needed for the solution of $\mathbf{u}$ and p and for the convergence rate of $\boldsymbol{\lambda}$. A full study is proposed in the Supplementary Material: we measure the drag coefficient K (Eq. (40)) of a translating periodic array of spheres in a domain of size $L/a = 8$ using the parameters b and c for the indicator functions chosen in the previous section, and we record the convergence history for numerous values of the various tolerances. Note that a tolerance for the inversion of the linear system of Eq. (31) for the computation of the velocities of the particles is needed as well: as this step is much less expensive than solving the fluid flow, this tolerance is set to a small value (10^{-6}) and is never changed. From the data, we have drawn that tol_λ sets the distance of the solution from the value at convergence, tol_u influences the minimal value of the residual of $\boldsymbol{\lambda}$ for which a good convergence behavior is still maintained, and tol_p has an influence on the oscillations of the residual of $\boldsymbol{\lambda}$; the latter also sets the fractional rate of expansion.

The purpose of this article is the illustration of the method and its numerical implementation and features, and we concentrate on its validation. As a consequence, we chose to keep low tolerances for the different quantities, considering that, depending on the required computation speed and precision, less demanding tolerances could be chosen. Therefore, for all the results shown in this article, except for the simulations of particulate suspensions, we set $\mathrm{tol_u} = 10^{-6}$ and $\mathrm{tol_p} = 5 \cdot 10^{-6}$; as for $\boldsymbol{\lambda}$, we set $\mathrm{tol}_\lambda = 10^{-5}$ for the first time step (always more computationally expensive) and $\mathrm{tol}_\lambda = 10^{-4}$ for the next ones.

4.4.6. Computational performances

In this section, the computational performances of the numerical method are evaluated against the computation of the shear flow of moderately concentrated to concentrated suspensions as detailed in Section 6.1. In Table 3, we present the relative computational times of the flow resolution (step 3 of the algorithm: fluid velocity and pressure fields) and computation of the velocities of the particles (step 4 of the algorithm: inversion of the linear system of Eq. (31)) with respect to the total time step, varying the number of particles N_P. The sum of these two computational times does not amount to the total computation time, as the writing of results files and the setup of the time step (moving the particles, building the resistance matrix, etc.) are not shown here. As we can observe, the computation of particle velocities takes more and more time with respect to the total time step as we increase the number of particles. We did not test the optimization of this step, however, it may be possible to reduce it by coupling OpenMP with MPI, since OpenMP is already implemented in the Eigen library, which is used to solve the linear system associated with the velocities of the particles. We also present the wall times for the different simulations; we employed two different partitions: one with Intel Xeon Gold 6428 @2.5GHz cores and the other with AMD Epyc 7302 @3GHz cores.

Table 3
Computational times for the Couette flow of a suspension.

ϕ	N_P	$(L_x, L_y)/a_1$	L_z/a_1	flow res. [%]	parts. vels. [%]	partition	N_{cores}	N_P/N_{cores}	wall time [s]
0.27	350	20	20	80	7	Intel	96	3.65	0.40
0.32	416	20	20	77	8	Intel	96	4.33	0.42
0.37	481	20	20	72	10	Intel	96	5.01	0.45
0.42	547	20	20	76	9	Intel	64	8.55	0.66
0.47	956	25	20	48	20	AMD	128	7.47	0.58
0.52	1057	25	20	40	30	Intel	192	5.51	0.91

5. Validations: one to three spheres in Stokes flow

5.1. Stokes flow through a periodic array of spheres

We consider here the slow flow of a Newtonian liquid through a simple cubic periodic array of spheres, and we focus on the drag force exerted on the array. This problem has been solved by Hasimoto (1958) [58] using the Fourier series and by Zick and Homsy (1982) [59] using a collocation method. The direction of the flow is parallel to one of the lattice basis vector and, in the cited papers, the spheres are kept stationary. In this geometry, the slip velocity is defined as the mean velocity over a unit cell:

$$\mathbf{U}_s = \frac{1}{V_0}\int_{\mathcal{D}_{fluid}} \mathbf{u}\ \mathrm{d}\mathcal{V} = \frac{1}{V_0}\int_{\mathcal{D}} \mathbf{u}\ \mathrm{d}\mathcal{V} \tag{39}$$

where V_0 is the volume of the unit cell $\mathcal{D}$. The drag force exerted on each sphere of the array is given by:

$$\mathbf{F} = 6\pi\eta a K \mathbf{U}_s \tag{40}$$

where K is the drag coefficient. Hasimoto (1958) [58] derives the following expression for K for a simple cubic lattice:

$$K = \frac{1}{1 - 1.7601\sqrt[3]{\phi} + \phi - 1.5593\phi^2 + \dots} \tag{41}$$

where $\phi = (4/3)\pi a^3/V_0$ is the solid volume fraction of the array. The numerical computations by Zick et al. (1982) [59] showed that Eq. (41) is valid up to volume fraction values of approximately 0.06. In this article, we consider volume fraction lower than 0.0082, i.e. inside the validity range of Eq. (41).

In Fig. 4 we show the numerical setup that allows measurement of the drag coefficient K, i.e. a single sphere in a cubic domain of side length L with periodic boundary conditions for the velocity $\mathbf{u}$ and the

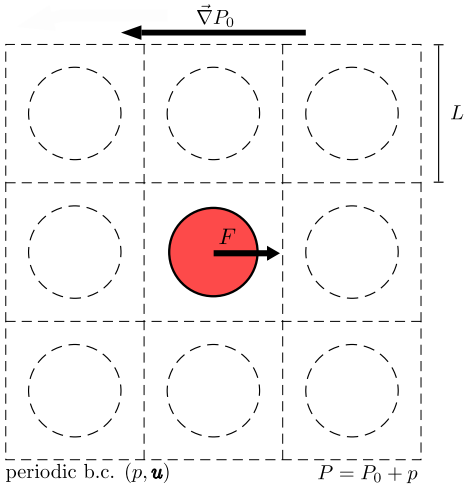

Fig. 4. Stokes flow through a periodic array of particles. **F** denotes the hydrodynamic drag force exerted on the particle.

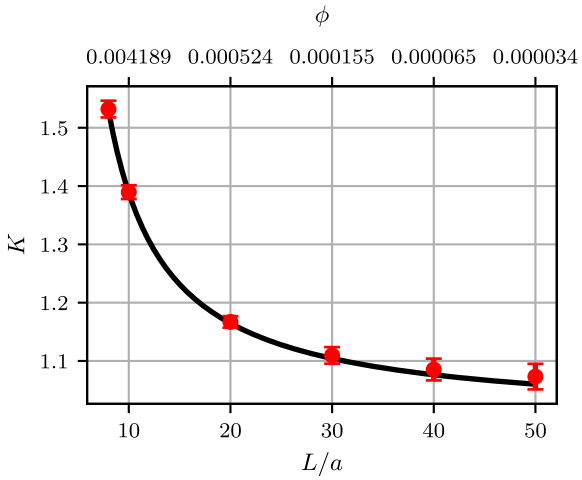

Fig. 5. Drag coefficient K as a function of the reduced size of the cubic cell, or equivalently as a function of the solid volume fraction ϕ ($(b, c) = (5, 0.3)$): red dots: simulation results; plain line: Hasimoto (1958) predictions [58].

pressure p on all boundaries. A uniform pressure gradient in the x-direction is added to the periodic pressure to induce fluid flow. To stick to the usual algorithm, the particle velocity is left as a free parameter, but an external force is exerted on the particle to counterbalance the hydrodynamic force (Eq. (30)). This force is deduced from the fluid momentum balance Eq. (1):

$$\mathbf{0} = \boldsymbol{\nabla} \cdot \boldsymbol{\sigma} - \boldsymbol{\nabla} P_0 + \rho_f \boldsymbol{\lambda} \tag{42}$$

where the stress is split into the periodic component $\boldsymbol{\sigma}$ and the uniform pressure tensor $-P_0 \boldsymbol{\delta}$. Eq. (42) is integrated over the simulation domain, yielding the total hydrodynamic drag force exerted on the particle:

$$\mathbf{F} = -\rho_f \int_{\mathcal{D}_p} \boldsymbol{\lambda}(\mathbf{x}) \mathrm{d}\mathcal{V} = -V_0 \boldsymbol{\nabla} P_0 \tag{43}$$

meaning that the hydrodynamic force exerted by the particle on the surrounding liquid is transmitted to the boundaries, where the only contribution to the net force originates in the pressure P_0.

Finally, the slip velocity $\mathbf{U}_s$ is computed:

$$\mathbf{U}_s = \frac{1}{V_0} \int_{\mathcal{D}} \mathbf{u}(\mathbf{x}) \mathrm{d}\mathcal{V} - \mathbf{U} \tag{44}$$

The opposite of the slip velocity, i.e. the particle velocity in the reference frame where the suspension as a whole is at rest, corresponds to the particle settling velocity in a sedimentation experiment. The drag coefficient K follows from Eq. (40), averaging over 64 positions inside a single mesh cell to get rid of the oscillations due to the mesh. As previously explained in Section 4.4, this simulation allows to tune the parameters b and c involved in the indicator functions $\mathcal{I}_u(\mathbf{x})$ and $\mathcal{I}_\lambda(\mathbf{x})$ (Eqs. (36) and (37)). The drag coefficient K mostly depends on the parameter c, i.e. on the effective radius of the particle. The computed values of K are shown for the best values $(b, c) = (5, 0.3)$ in Fig. 5 and in Table 4 for different values of the ratio L/a, or equivalently for different values of the solid volume fraction ϕ, in very good agreement with the theoretical predictions of Hasimoto (1958) [58] (Eq. (41)). It should be noted here that the long-range hydrodynamic interactions between the particles in the lattice are always important or at least significant, including the case of the largest unit cell considered ($L/a = 50$), and that they are properly accounted for by the Fictitious Domain Method.

Table 4
Drag coefficient K as a function of the reduced size of the cubic cell, or equivalently as a function of the solid volume fraction ϕ ($(b, c) = (5, 0.3)$): comparison between the simulations results K and the values K_H predicted by Hasimoto (1958) [58].

L/a	ϕ	K_H	K	σ_K	$\lvert K - K_H\rvert/K_H$ [%]
8	0.00818	1.53041	1.532059	0.014381	0.11
10	0.00419	1.38805	1.389611	0.011877	0.11
20	0.000524	1.16461	1.167027	0.009899	0.21
30	0.000155	1.10427	1.109563	0.014221	0.48
40	0.0000654	1.07627	1.085323	0.018710	0.84
50	0.0000335	1.06012	1.073184	0.021934	1.23

5.2. A free sphere in the presence of walls

In this section, the numerical method is tested against various shear flows past a single free sphere in the presence of solid walls. The first two examples address the case of a simple shear flow, bounded by either one or two planes. It is shown that such flows are conveniently tackled, whether the particle is close to the wall and sub-grid corrections are needed, or not. In the latter two-plane configuration, the flow may be strongly confined leading to strong hydrodynamic interactions with both walls, and it is still suitably computed. Finally, the case of a single sphere in a confined nonlinear (Poiseuille) flow is addressed.

5.2.1. A sphere in simple shear flow close to a single wall

A free single particle with radius a is suspended in a simple shear flow close to a wall with $\varepsilon = d/a - 1$, where d is the distance between the particle center and the wall (Fig. 6).

The simulation volume is a square hexahedron with dimension $(L_x/a_1,\ L_y/a_1,\ L_z/a_1) = (50,\ 50,\ 50)$. On the top and bottom boundaries (respectively $y = L_y$ and $y = 0$), the velocity is prescribed (respectively $\mathbf{u} = \mathbf{0}$ and $\mathbf{u} = \dot{\gamma} L_y \mathbf{e}_x$). The pressure and velocity fields on the other boundaries ($x = \pm L_x/2,\ z = \pm L_z/2$) obey cyclic boundary conditions. The quantities of interest, namely the particle velocity, angular velocity, and stresslet, are computed for different values of the distance to the lower wall d, and both particle radius values a_1 and a_2. For each value of the distance to the wall and each particle radius, the quantities of interest are averaged over 16 different positions of the particle center evenly distributed in a single mesh cell. The standard deviation is computed to evaluate the accuracy of the computation and shown on the figures as error bars.

Since the size of the simulation box is much larger than the particle radius, the simulation data may be compared to the case of a free particle close to a single wall in an otherwise unbounded liquid. Chaoui and

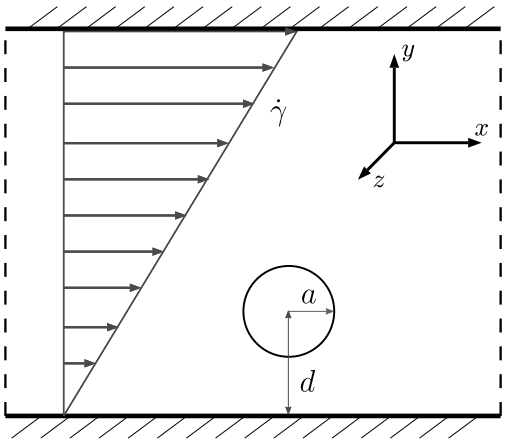

Fig. 6. Free sphere in simple shear flow close to a wall.

Feuillebois (2003) [60] have performed highly accurate computations of the velocity and angular velocity of the particles in that case. They provide also a polynomial expansion in $log(\varepsilon)$ for both quantities:

$$U_x = \left[\sum_j u_j \left(\log \varepsilon\right)^j\right]^{-1}, \qquad \Omega_z = \left[\sum_j \omega_j \left(\log \varepsilon\right)^j\right]^{-1} \tag{45}$$

where the coefficients u_j and ω_j are given in their article [60]. They show for instance that the expansion gives a precision better than 10^{-11} for the velocity for $\varepsilon \leq 0.4$. The data from the current simulations are compared to the values from their expansion in Fig. 7. The agreement is very good, in particular for values of ε lower than 0.15 for which the sub-grid corrections (the relevant functions are here Y^A, Y^B, Y^C) are activated. It should be recalled here that, according to the lubrication approximation, both the velocity and the angular velocity of the sphere slowly approach 0 as the reduced distance ε goes to 0 [60].

Sangani et al. (2011) [61] have performed computations of the stresslet in the same flow conditions. They use a semi-analytical method based on Lamb's multipoles. They also show that their data for the normalized stresslet $S^* = S_{12}/\left[(10/3)\,\pi\eta a^3\dot{\gamma}\right]$ are well approximated by the expressions given below:

$$S^* = \begin{cases} \left[1 - \dfrac{15}{16Y^3} + \dfrac{1}{Y^5} - \dfrac{0.65}{Y^7}\right]^{-1} & \text{for } 0 < 1/Y \leq 0.85 \\ \dfrac{0.847 \ln \varepsilon^{-1} - 0.41 + 1.44\varepsilon \ln \varepsilon^{-1} - 0.3\varepsilon}{(1/5)\ln \varepsilon^{-1} + 0.6376} & \text{for } 0.85 < 1/Y \leq 1 \end{cases} \tag{46}$$

where $Y = 1 + \varepsilon$. The data from the current simulations are displayed in Fig. 8. Again, a very good agreement is found between the simulation data and the correlation law Eq. (46) over the whole range of the distance to the wall, including the low distance range where the sub-grid corrections are needed. The relevant functions are here Y^A, Y^B, Y^C, Y^G, Y^H.

As a conclusion to this section, the interaction between a sphere and a single wall in a simple shear flow is conveniently tackled by the FDM supplemented by the frame-invariant sub-grid corrections. Since the underlying shear flow is not explicitly taken into account in the computation of the sub-grid corrections, this confirms that the FDM solver without sub-grid correction can capture the specific contribution of the ambient shear flow, as explained in Appendix D. This good agreement was indeed expected since the particle-wall sub-grid corrections have been built for this particular flow to be conveniently tackled. In the following, more complicated flows are addressed to further check the validity of the method.

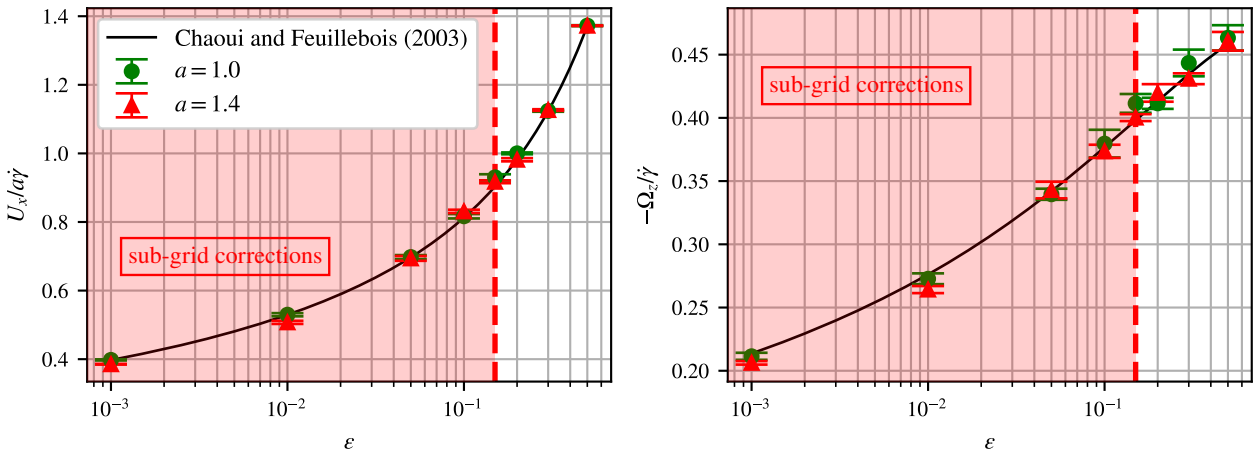

Fig. 7. Normalized translational and rotational velocities for a free sphere in a simple shear flow close to a wall.

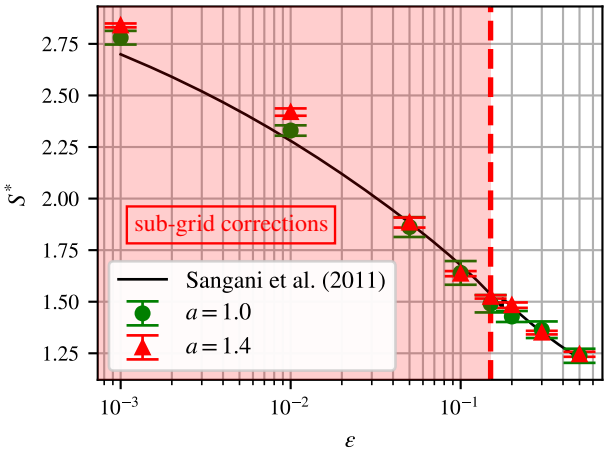

Fig. 8. Normalized stresslet S^* for a free sphere in a simple shear flow close to a wall.

5.2.2. A sphere in simple shear flow at the center of a channel

In this section, a free sphere is placed at the center of a channel. The upper and lower walls move with equal and opposite velocities, inducing a simple shear flow in the liquid in-between them (Fig. 9). On the other boundaries, periodic conditions are applied for the pressure and velocity fields. The flow is computed, together with the particle angular velocity Ω_z and the normalized stresslet S^* for different values of the reduced distance between the walls H/a. The translational velocity of the sphere is zero due to the symmetry of the flow. The dimensions of the bounding walls have been chosen large enough to mimic infinite planes $(L_x \times L_y) = (60a \times 40a)$. This case may appear a bit different from that addressed in the previous section, because of the significant hydrodynamic interactions between the walls. More precisely, in the more confined geometry where $H \sim 2a$, besides the small scale flow between the sphere surface and the plane that makes the sub-grid corrections necessary, vortices develop in front of the sphere and behind it, with a typical dimension of the channel width, or equivalently of the sphere radius [61].

The computed angular velocity and normalized stresslet are displayed in Fig. 10 together with the computational data obtained by Sangani et. al (2011) [61]. Again, for each value of H, both particle radii $a_1 = 1.0$ and $a_2 = 1.4$ are considered and the quantities are averaged over 16 different positions of the particle center evenly distributed within a single mesh cell. The agreement is again satisfactory, still with small oscillations of the angular velocity (at most 3%). This shows that the current method can account for all components of the flow despite its complexity.

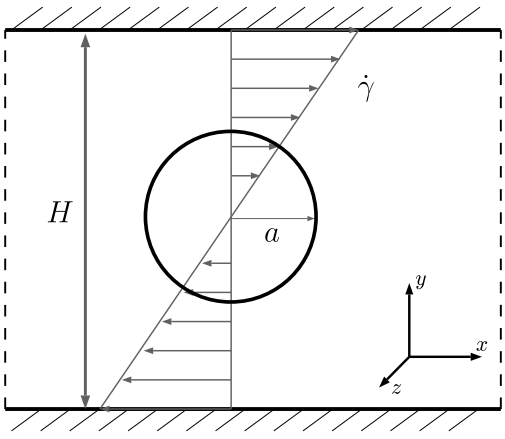

Fig. 9. Free sphere in a simple shear flow at the center of a channel.

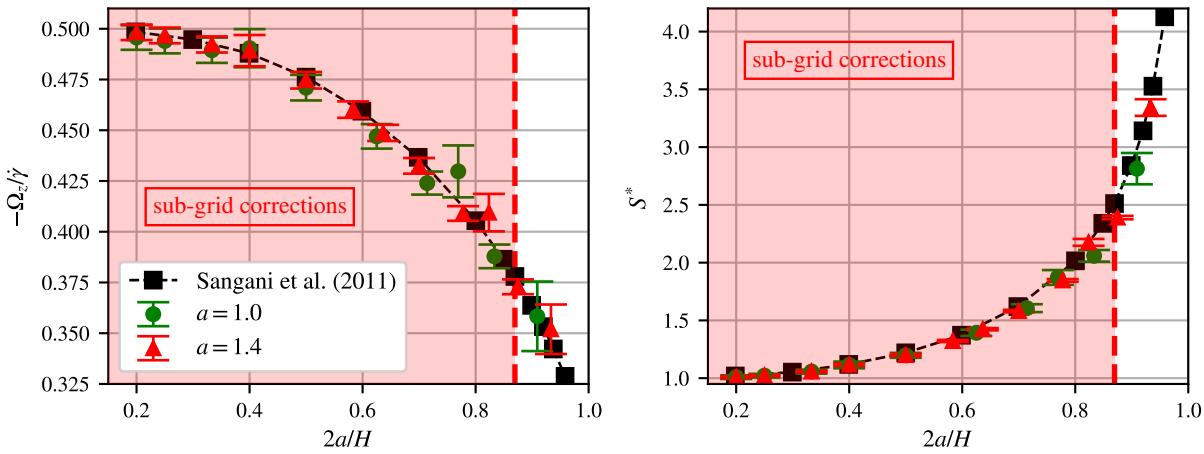

Fig. 10. (left) Normalized angular velocity and (right) stresslet for a free sphere in a simple shear flow at the center of the channel. The line is a guide to the eye.

5.2.3. A free sphere in a channel with a Poiseuille flow

We turn now to the flow induced by a free-moving sphere in an ambient Poiseuille flow. The purpose of this section is to check the validity of the method for a single sphere in a nonlinear flow, including the sphere-wall sub-grid correction. The plane Poiseuille flow is bounded by two parallel walls separated by a distance H (see Fig. 11), and the unperturbed velocity reads:

$$\mathbf{u}_0(\mathbf{x}) = U_c \left(1 - \left(\frac{2y}{H}\right)^2\right) \boldsymbol{e}_x \tag{47}$$

A homogeneous pressure gradient is applied in the whole simulation domain:

$$\boldsymbol{\nabla} P_0 = -8\eta \frac{U_c}{H^2} \boldsymbol{e}_x \tag{48}$$

The particle translational U_x and rotational Ω_z velocities as well as the stresslet S_{xy} are computed for different values of the channel height H and of the reduced distance between the particle center and the bottom wall d/a. Again, the computed quantities are averaged over 16 different positions inside the plane section of a single mesh cell. Two different radius lengths are considered for the sphere, $a = a_1 = 1.0$ and $a = a_2 = 1.4$. The channel height H is sampled in the range $[2.86a;\ 20a]$ and the dimensions of the bounding walls are chosen as $(L_x \times L_z) = (60a \times 40a)$.

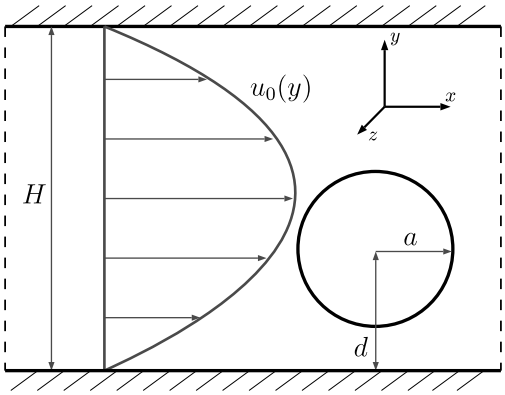

Fig. 11. A free sphere in a plane Poiseuille.

Using a boundary-integral method, Staben et al. (2003) [62] computed the translational and angular velocities of the sphere in a similar flow geometry, although with infinite planes. The current computations are compared to their data in Fig. 12. The agreement is very good, whether the sphere is close to the wall or not, and for all values of $2a/H$, including the most confined case $2a/H = 0.7$. The latter case is probably the most important for our purpose due to the strongly nonlinear variation of the unperturbed flow at the scale of the sphere: the shear rate variation over the sphere diameter $16aU_c/H^2$ amounts to $8a/H \approx 1.6$ times the mean shear rate of the flow $2U_c/H$, making the definition of a single value for the shear rate as seen by the particle difficult. For that reason, the formulation of the particle-wall sub-grid corrections in Eq. (D.6) is better suited to the current flow geometry than the general expression in Eq. (A.6), and, as already noted, its accuracy is very satisfactory.

Ghalya et al. (2020) [63] computed the stresslet for $2a/H = 0.4$ using a bipolar coordinates method (infinite planes). Their results for the normalised stresslet $S^* = S_{xy}/\left(4U_c\eta a^3/H\right)$ are displayed in Fig. 13, together with the values from the current method. Both sets of values are in close agreement, including the smallest value of the distance to the wall $d/a = 1.1$, which requires sub-grid corrections.

The data from Refs. [62] and [63], together with the corresponding computed values using the current model are gathered in Tables S1 and S2 in the Supplementary Material.

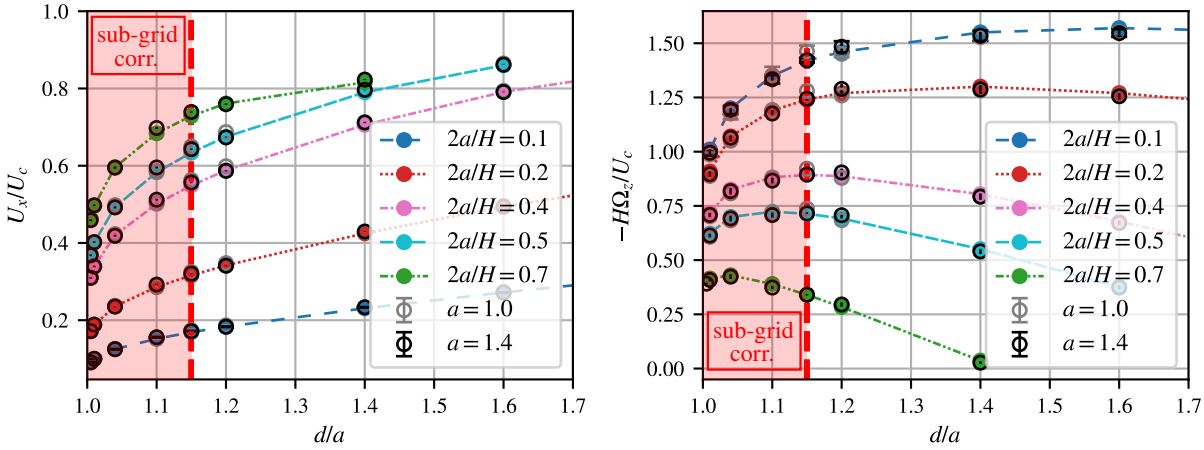

Fig. 12. (left) Normalized translational and (right) rotational velocities for a free sphere in a plane Poiseuille for different channel heights H and distances from the bottom wall d/a. (•): Staben et al. (2003) [62], the lines are a guide to the eye. (◯): current computations.

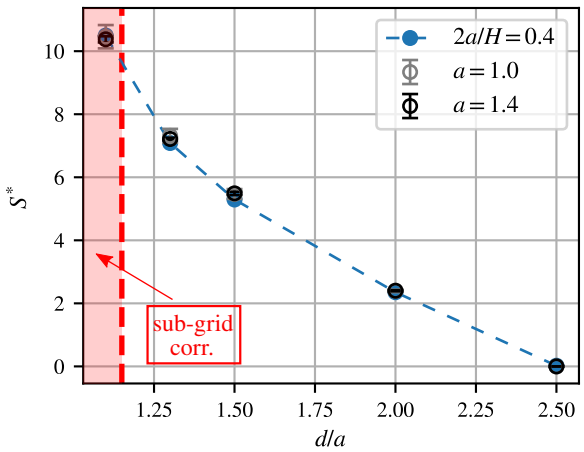

Fig. 13. Normalised stresslets S^* for a free sphere in a plane Poiseuille for $2a/H = 0.4$ and different distances from the bottom wall d/a. (•): Ghalya et al. (2020) [63], the lines are a guide to the eye. (◯): current computations.

5.3. A particle pair in simple shear flow

The emblematic case of two particles in simple shear flow is treated here. The flow is the same as in Section 5.2.2, with $L_x = L_y = L_z = 40a_1$. The particles are placed in the same shear plane $z = 0$, at initial positions $x/a_1 = \pm 3$, $y = \mp\, r_y^0/2$, where r_y^0 is the impact parameter, and the relative trajectory is computed. Different trajectories are computed by changing the radii ratio a_2/a_1 and the impact parameter r_y^0. Two different cases are considered: either the particles move only due to hydrodynamic interactions, or an additional force is applied to mimic contact between particles as they are close enough.

In the former case, the relative trajectory is expected to display fore-aft symmetry [64] due to the linearity of Stokes equations combined with the symmetry of the ambient flow. In addition, depending on the impact parameter, the trajectories may either be open ("large" impact parameter) or closed and periodic ("small" impact parameter). Zarraga and Leighton (2001) [65] showed that for two particles with the same radius $a_2 = a_1$, the smallest distance between the surfaces for an open trajectory is very small, i.e. approximately $4 \cdot 10^{-5} a_1$, so that a quite short time step is required to obtain sufficient accuracy. The time step is $\delta t = 10^{-4}$ in the following. In Fig. 14 (top), the trajectories for $a_2/a_1 = 1$ and different impact factors are showed. They display the expected fore-aft symmetry, suggesting that the hydrodynamic interactions are properly tackled and that the time step is sufficiently small. The plain lines on the figure correspond to the direct time-integration of the velocity computed for a pair of free particles using the theoretical two-particle resistance matrix, in close agreement with the FDM computations. We also checked that the trajectories as computed from the mobility functions given in Ref. [64] were in good agreement too. In Fig. 14 (top, right), the distance between the particles is displayed as a function of the relative x-position, r_x of the particles for the same trajectories as in Fig. 14 (top, left), together with its counterpart using direct integration of the theoretical velocity. Again, the good agreement validates the FDM computations. It should be stressed here that the cumulative error over $2 \cdot 10^5$ time steps is sufficiently small that fore-aft symmetry is preserved and that the trajectories from both methods are in close agreement.

On the other hand, non-hydrodynamic forces, such as contact forces, are known to induce asymmetry of the trajectory [64, 65]. To validate the FDM against the computation of contacting particles trajectories, a roughness height h_r is defined, and a contact force is triggered as the distance between the surfaces is smaller than h_r. A standard contact model is used, also including friction [55]. It is briefly summarized in the Supplementary Material. A typical trajectory is shown in Fig. 14 (bottom) for size ratio $a_2/a_1 = 1.4$, roughness $h_r = 5 \cdot 10^{-3}$ and friction coefficient $\mu_s = 0.5$. Fore-aft asymmetry is induced by contact between particles that occurs for $-1.39 \lesssim r_x/a_1 \lesssim 0$ ($\xi \leq 2h_r/(a_1 + a_2) \approx 4.2 \cdot 10^{-3}$). Again, the simulations show good agreement with the data from the direct time integration of the theoretical velocity. However, a slight discrepancy may be observed at the end of the trajectory: this is caused by the hydrodynamic interactions with the walls that are not accounted for by the theoretical two-particle matrix. Even though the domain is quite large compared to the particle sizes, the residual hydrodynamic interactions with the walls push the particles to the centerline, slightly slowing them down as well and causing some delay. This discrepancy is more easily observed in the current case than in the former one probably because one of the particles is larger, and consequently induces stronger hydrodynamic interactions with the walls.

To complete the validation for this type of flow, various components of the normalized hydrodynamic stresslet $\mathbf{S}_p^{h^*} = \mathbf{S}_p^h / \left[(10/3)\,\pi\eta a^3 \dot{\gamma}\right]$ are shown in Fig. 15 for each particle. Smooth particles are considered here to avoid contact (see figure caption for a complete list of simulation parameters). Again, the data from the simulations compare very well with their theoretical counterpart, which was computed using the theoretical resistance matrix on a trajectory computed by direct time-integration of the theoretical particle velocity.

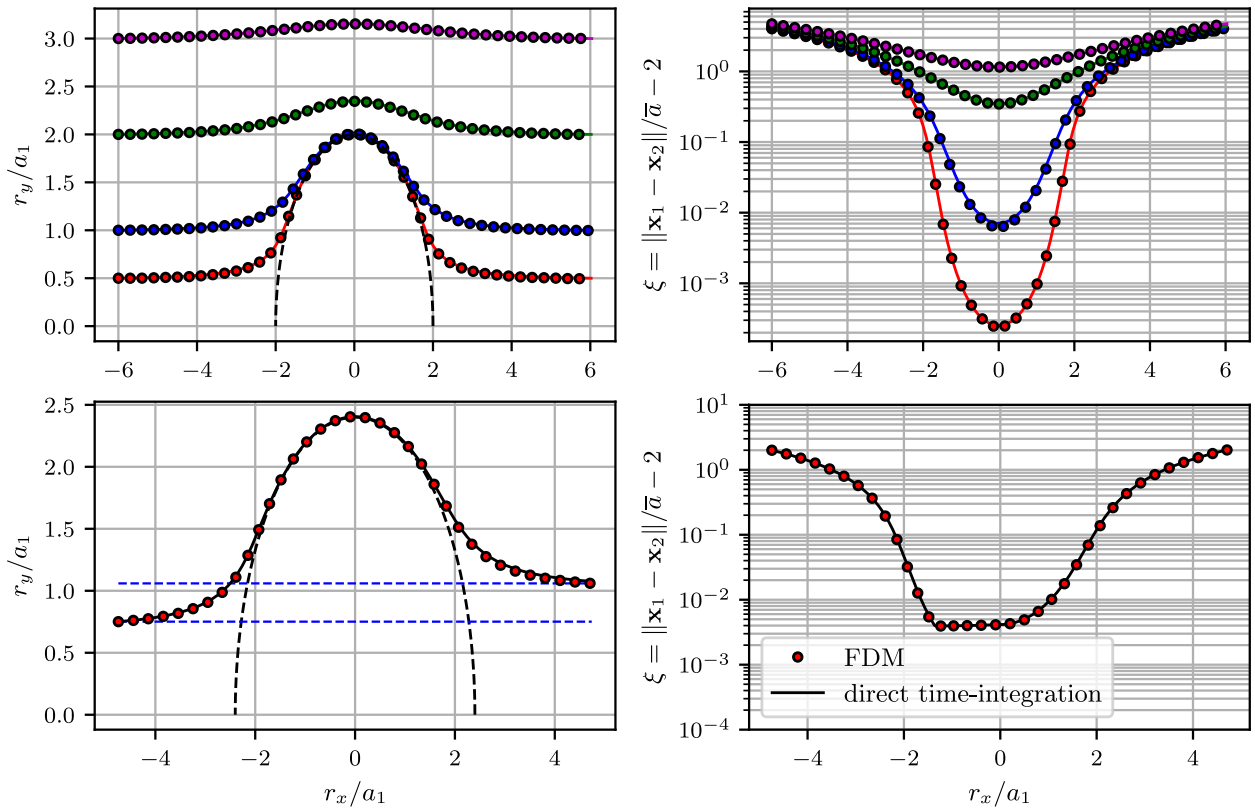

Fig. 14. (left) Relative trajectories and (right) normalized distance between the particle surfaces of a particle pair in a simple shear flow. Results for different impact factors without contact ($h_r = 0$, $a_2/a_1 = 1$) (top), and for a case with contact ($h_r = 0.005a_1$, $\mu_s = 0.5$, $a_2/a_1 = 1.4$) (bottom). Symbols: FDM computation. Plain line: time-integration of the velocities using the theoretical two-particle resistance matrix.

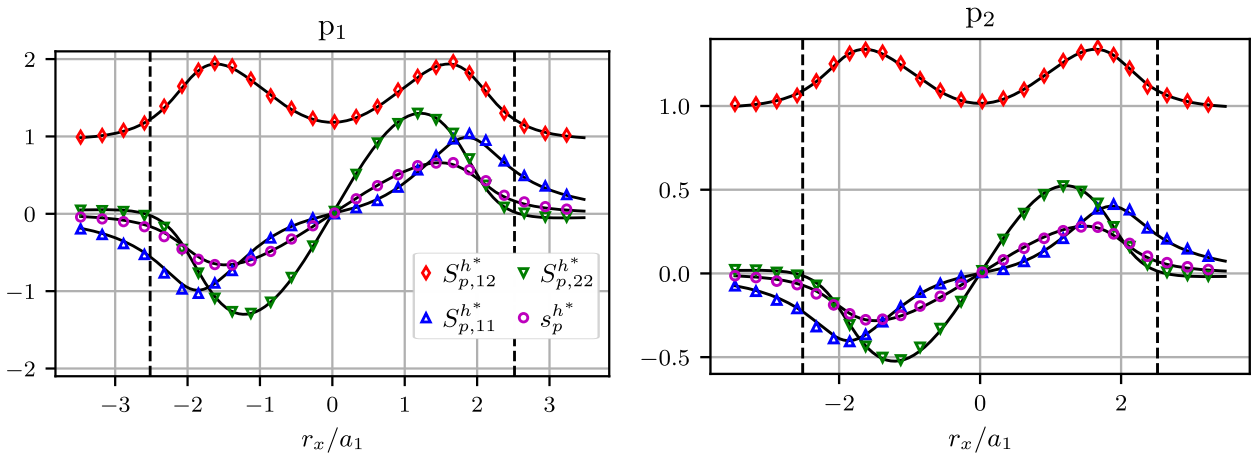

Fig. 15. Normalized hydrodynamic stresslet ($\mathbf{S}^{h^*}_p = \mathbf{S}^h_p / \left[(10/3)\,\pi\eta a^3\dot{\gamma}\right]$) components and trace for a particle pair in a simple shear flow without contact as a function of relative particle position ($h_r = 0$, $\mu_s = 0.5$, $a_2/a_1 = 1.4$, $r^0_x/a_1 = -3.48$, $r^0_y/a_1 = 0.93$). Comparison between (black lines) theoretical stresslet for the trajectory from time-integration of the velocities using the theoretical two-particle resistance matrix and (colored lines) simulation results. (left) Data for particle (p_1) ($a_1 = 1.0$) and (right) for particle (p_2) ($a_2 = 1.4$). Sub-grid corrections are applied for positions between the vertical dashed lines.

5.4. A particle pair in confined Poiseuille flow

The purpose of this section is to show that the current numerical method properly accounts for hydrodynamic interactions between two particles in a nonlinear flow, particularly when the small distance between the particle surfaces requires sub-grid corrections. We consider two identical force- and torque-free particles with radius a suspended in a plane Poiseuille flow bounded by parallel planes (Fig. 16). This particular flow has been numerically solved by Bhattacharya et al. (2006) [66] for infinite walls using an accurate Cartesian-representation method. In the current study, the dimension of the stationary bounding walls is set to $(L_x \times L_z) = (60a \times 40a)$, and the channel height is set to $H = 4a$. On the other bounding surfaces, periodic boundary conditions are applied. As in Section 5.2.3, the unperturbed parabolic flow (Eq. (47)) is induced by an imposed pressure gradient (Eq. (48)). Both particles are in the same plane $(\boldsymbol{e}_x, \boldsymbol{e}_y)$. The first particle is placed at the center of the channel, while the second one is placed at a distance from the lower wall $d/a = 1.33$. The relevant particle translational and rotational velocities U_x, U_y and Ω_z are measured for values of the reduced lateral distance between the particles ρ_{12}/H (Fig. 16) ranging from 0.4714 to 1.5, which correspond to reduced distance $\xi = 2\|\mathbf{x}_2 - \mathbf{x}_1\|/(a_1 + a_2) - 2$ between the particle surfaces ranging from 10^{-5} to 4.04. As before, for each value of the lateral distance, the measured quantities are averaged over 16 different particle positions inside the plane section of a single mesh cell.

The normalized velocities U_x/U_c, U_y/U_c and $2a\Omega_z/U_c$ from the FDM computations are displayed in Figs. 17 and 18 together with the results from Ref. [66]. As shown in the latter article, the interactions between the particles are quite strong in that arrangement of the particle positions, resulting in significant variations of the velocities as a function of ρ_{12}. We note a very good agreement between the current results and those from Ref. [66], both in the near-contact and the far-field regions. In particular, the decay of the far-field flow, which is specific to the two-wall configuration [66], is properly accounted for by the FDM solver. In the near-contact region, the particle velocities primarily depend on the lubrication flow between the particle surfaces. As shown in Figs. 17 and 18, the sub-grid corrections allow accurate computation of the velocities in this distance range. The intermediate range is accurately described as well, with a sign change in the y-component of the translational particle velocities at $\rho_{12}/H \sim 0.6$. It should be stressed again that the expression of the sub-grid corrections in Eq. (21) does not require specifying any ambient strain rate tensor, which would be difficult to define in this particular case. The shear rate of the unperturbed flow indeed significantly varies at the scale of the particle, not to mention the strong influence of the walls on the flow around the particles.

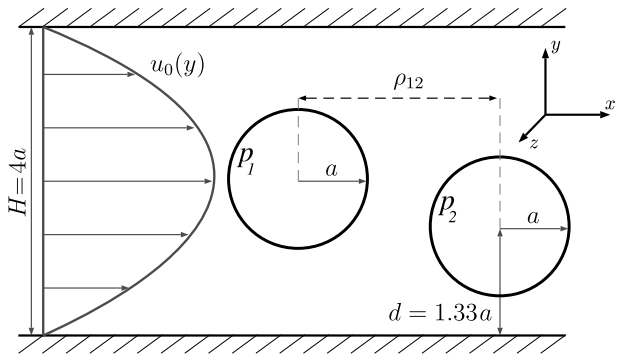

Fig. 16. Two spheres in a plane Poiseuille.

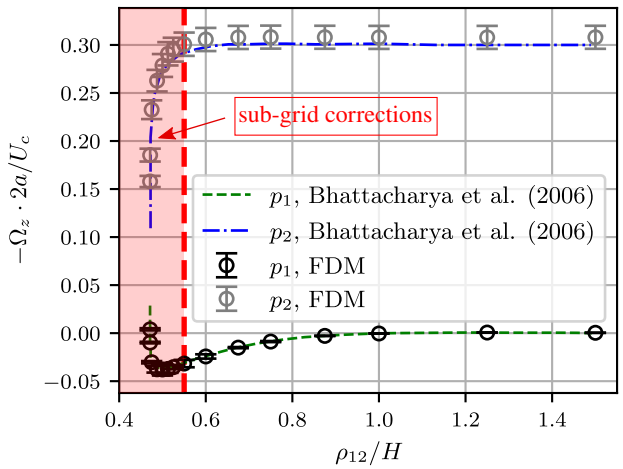

Fig. 17. Rotational velocities Ω_z for two free spheres in a plane Poiseuille for different inter-particular distances ρ_{12}.

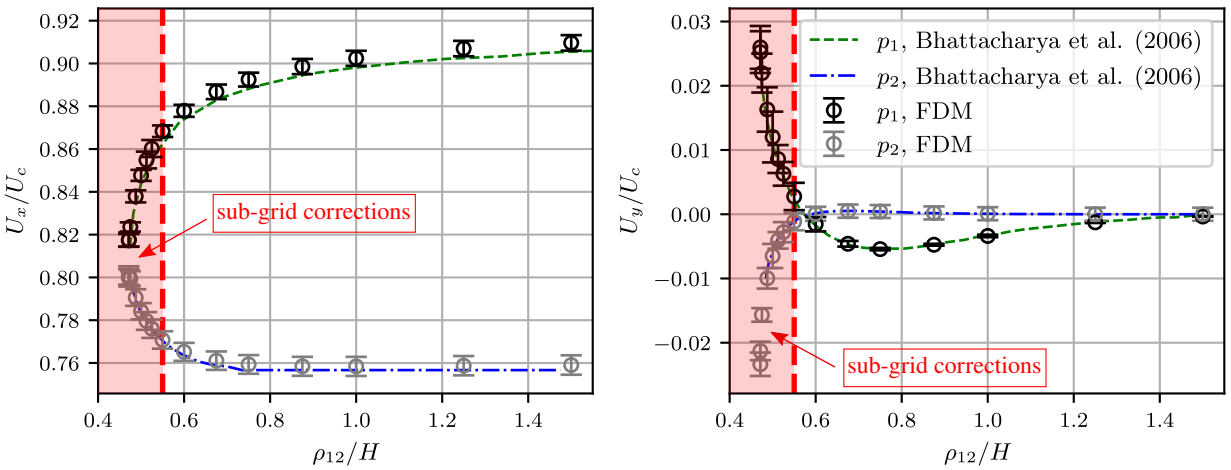

Fig. 18. Normalized translational velocities U_x (left) and U_y (right) for two free spheres in a plane Poiseuille as a function of the lateral distance ρ_{12}.

5.5. Three particles in a liquid at rest

We investigate the dynamics of three particles of radius a arranged in an equilateral triangle of side r in a quiescent fluid (see Fig. 19). Particle (p_1) is driven toward the triangle centroid with a force $F_x\boldsymbol{e}_x$ but no torque is exerted, while the two remaining particles are freely moving. The particle centers lie in the plane (x, y) and the dimensions of the simulation domain are $(L_x/a, L_y/a, L_z/a) = (60, 40, 50)$. The planes $y = \pm L_y/2$ are rigid walls at rest, while at the other boundaries $x = \pm L_x/2$ and $z = \pm L_z/2$ periodic conditions are applied. The velocities of all three particles are measured in the direction of the force (x) and the direction perpendicular to it (y), together with the angular velocity of particles (p_2) and (p_3) in the z-direction perpendicular to the plane of the particle centers. The velocities and angular velocities are made dimensionless using respectively $F_x/(6\pi\eta a)$ and $F_x/(6\pi\eta a^2)$.

The triangle size, i.e. the distance between the particles, is varied over a range including both values for which sub-grid corrections are needed or not. For each distance, 64 different positions of the triangle centroid inside a single mesh cell are considered, and both the average quantities and their standard deviation are computed. The data are gathered in Tables 5 to 7 together with the reference solution provided by Wilson (2013) [67], using a technique based on the Method of Reflections, for the case of a boundary-free system with an infinite extension of the fluid.

The velocities in the direction of the force (Table 5) from the FDM are significantly underestimated compared to the data from Ref. [67]. It was expected since an external force parallel to the walls is applied on the triangle of particles, which induces a stokeslet flow far away from the particles. The latter is a slowly decreasing function of the distance, and thus induces significant hydrodynamic interactions, both with the

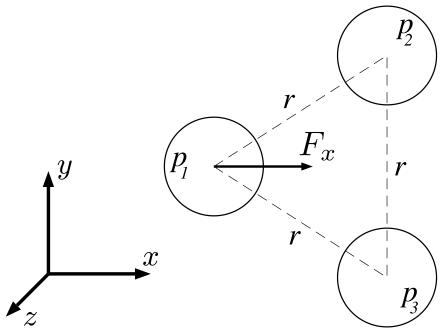

Fig. 19. Three spheres arranged in an equilateral triangle, one of which is driven toward the centroid with a force F.

walls and with the implied periodically repeated triangles. The discrepancy between the mean velocity of the three spheres from the FDM and the infinite size system amounts to 3.5% to 5.5%, which is roughly consistent with the discrepancy observed for the mobility of a single sphere with radius $1.4a_1$ at the center of the simulation box, driven by a force parallel to the walls, compared to the theoretical sphere mobility in a fluid of infinite extension. Anyway, the discrepancy is strongly reduced if the difference of velocity of particles (p_2/p_3) with respect to particle (p_1) is considered (Table 6). This was indeed expected, due to the small distance between the particles compared to the distance of the triangles to the walls.

As for the velocity normal to the wall (y-component), the discrepancy between the data from the FDM and the infinite fluid case is very small (Table 7). This is probably because no stokeslet is produced in the direction normal to the walls so the interactions with the walls are weaker. The angular velocities from the two methods (Table 7) are in better agreement as well, probably because the prominent contribution to the hydrodynamic interactions with the wall is the gradient of the flow induced by the reflection of the stokeslet parallel to the walls.

As a conclusion, except for the discrepancies induced by the hydrodynamic interactions with the walls due to the stokeslet originating in the external force, the computed quantities from the FDM are in good agreement with the accurate computations from Ref. [67]. In particular, the short-range hydrodynamic interactions seem to be well tackled by the sub-grid corrections.

Table 5
Velocity components in the direction of the force parallel to the walls. The last two columns are the relative standard deviation from the 64 measurements (see text).

	Wilson (2013)		FDM (current work)			
r	$U_x^{p_1}$	$U_x^{p_{2,3}}$	$U_x^{p_1}$	$U_x^{p_{2,3}}$	$\frac{\sigma_{U_x^{p_1}}}{U_x^{p_1}}$ [%]	$\frac{\sigma_{U_x^{p_{2,3}}}}{U_x^{p_{2,3}}}$ [%]
2.01	0.65528	0.63461	0.61923	0.59857	2.3	2.4
2.10	0.73857	0.59718	0.70256	0.56129	2.2	2.7
2.50	0.87765	0.49545	0.83976	0.45889	1.7	3.1
3.00	0.93905	0.41694	0.90194	0.38084	1.6	3.7
4.00	0.97964	0.31859	0.94362	0.28491	1.4	4.6
6.00	0.99581	0.21586	0.96172	0.18428	1.4	6.6

Table 6
Relative velocity components in the direction of the force parallel to the walls. The last column is the relative standard deviation from the 64 measurements (see text).

	Wilson (2013)	FDM (current work)	
r	$U_x^{p_1} - U_x^{p_{2,3}}$	$U_x^{p_1} - U_x^{p_{2,3}}$	$\frac{\sigma_{\Delta U_x^{p_{1,23}}}}{\Delta U_x^{p_{1,23}}}$ [%]
2.01	0.02067	0.02066	3.5
2.10	0.14139	0.14127	2.8
2.50	0.38220	0.38087	1.0
3.00	0.52211	0.52110	1.1
4.00	0.66105	0.65870	0.6
6.00	0.77995	0.77743	0.5

Table 7
(left) Velocity components in the direction perpendicular to the force and (right) angular velocity component in the direction perpendicular to the force and parallel to the walls. The last column of each set is the relative standard deviation from the 64 measurements (see text).

	Wilson (2013)	FDM (current work)		Wilson (2013)	FDM (current work)	
r	$\lvert U_y^{p_{2,3}}\rvert$	$\lvert U_y^{p_{2,3}}\rvert$	$\frac{\sigma_{U_y^{p_{2,3}}}}{\lvert U_y^{p_{2,3}}\rvert}$ [%]	$\lvert \Omega_z^{p_{2,3}}\rvert$	$\lvert \Omega_z^{p_{2,3}}\rvert$	$\frac{\sigma_{\Omega_z^{p_{2,3}}}}{\lvert \Omega_z^{p_{2,3}}\rvert}$ [%]
2.01	0.00498	0.00501	8.9	0.037336	0.036476	5.0
2.10	0.03517	0.03514	5.5	0.052035	0.052299	8.3
2.50	0.07393	0.07372	1.5	0.045466	0.045646	7.2
3.00	0.07824	0.07830	1.1	0.035022	0.035065	5.9
4.00	0.06925	0.06893	0.7	0.021634	0.021648	6.8
6.00	0.05078	0.05003	0.3	0.010159	0.009992	8.7

6. Validation: particulate suspension flow

We turn now to the flow of a suspension containing many particles. In the first subsection, a Couette flow is considered, and the viscosity is computed for different values of the solid volume fraction. In the next subsection, an example of nonlinear flow is proposed, namely a plane Poiseuille flow. It is well-known that, in such a flow, particle migration toward the center of the channel is observed. The computed stationary volume fraction profile is shown and compared to previous numerical data.

Before the mentioned flows are studied in detail, some important points should be recalled concerning particle interaction forces, which were not addressed before. Contact forces between particles are known to have a major influence on the rheological properties of non-Brownian suspensions. Even in the case of model spherical particles, contact occurs due to micro-asperities on the particle surface [68, 69]. In particular, friction between particles significantly enhances the viscosity [23, 55, 70, 71]. In this article, both surface roughness and friction are taken into account using a simple contact model (see Ref. [70]), which is shortly explained in the Supplementary Material. Contact between particles occurs as soon as the distance between their surface is smaller than the roughness height h_r, resulting in elastic interaction forces, both normal ($\mathbf{F}_n$) and tangential ($\mathbf{F}_t$). Sliding is not allowed until the tangential force reaches the value $\|\mathbf{F}_t\| = \mu_s\|\mathbf{F}_n\|$, where μ_s stands for the static friction coefficient. As long as sliding occurs, the latter relation between normal and tangential forces holds, meaning that no difference is made here between the static and dynamic friction coefficients. The influence of h_r is quite moderate as long as its value is kept under $10^{-2}a_1$ [55]. In the following, the value $h_r/a_1 = 5 \cdot 10^{-3}$ is chosen, which is consistent with experimental data concerning quite smooth polymer spheres [68]. In contrast, friction induces a strong increase of the suspension viscosity [23, 55, 70, 71] as μ_s increases in the range $[0; 2]$. In the following, the friction coefficient value is chosen as $\mu_s = 0.5$.

Concerning the numerical details of the simulations presented in this section, aiming at reducing the computational time, we changed the tolerances for p and $\mathbf{u}$ and we employed $\mathrm{tol}_p = 10^{-3}$ and $\mathrm{tol}_u = 10^{-5}$. As presented in Section 4.4.5, these values still present good convergence behavior and small errors. In addition, by studying the residual of $\boldsymbol{\lambda}$ and the number of iterations needed for step 7 in the algorithm (i.e., the computation of the velocity and pressure fields and the update of the particle velocities, see Section 4.3), we decided to fix the number of iterations to limit the oscillations of the latter number due to the mesh, instead of checking $\|\boldsymbol{\lambda}^{n+1} - \boldsymbol{\lambda}^n\|/\|\boldsymbol{\lambda}^n\|$. In any case, the number of iterations required to obtain a given average small residual of $\boldsymbol{\lambda}$ varies with respect to the Δt employed. For example, for $\Delta t = 10^{-4}$ the needed number of iterations of step 7 of the algorithm is approximately 10.

As previously mentioned, the considered suspensions are made of particles of radii a_1 and $a_2 = 1.4a_1$ to reduce ordering. The two populations occupy the same volume, i.e. $\phi_1 = \phi_2 = \phi_{bulk}/2$.

6.1. Suspensions in simple shear flow

The same geometry as in Section 5.2 (Fig. 9) is considered here. The dimensions of the simulation domain are quoted in Table 8 for each simulation, together with the main simulation parameters, some of which will be explained in the following. The particles are placed at random positions at time zero, and after a short transient that occurs over a few strain units, the particle velocity and volume fraction reach steady profiles, from which the relevant quantities are extracted, time-averaging over a few tens of strain units.

Table 8
Suspension in Couette flow: simulation parameters.

ϕ_{bulk}	ϕ_{core}	$\dot{\gamma}_0$	$\dot{\gamma}_{core}$	L_x/a_1	L_y/a_1	L_z/a_1	N_P	Δt
0.27	0.303	1	0.923	20	20	20	350	10^{-4}
0.32	0.359	1	0.885	20	20	20	416	10^{-4}
0.37	0.405	1	0.873	20	20	20	481	10^{-4}
0.42	0.458	1	0.773	20	20	20	547	10^{-4}
0.47	0.493	1	0.745	25	25	20	956	10^{-4}
0.52	0.543	1	0.563	25	25	20	1057	10^{-4}
0.54	0.570	1	0.391	25	25	20	1098	$2 \cdot 10^{-5}$

Experimental [72, 73, 74] and numerical [6, 54, 55, 56] studies have shown that, as a non-Brownian monodisperse suspension is sheared between smooth walls, the particles near the wall form layers. Depending on the volume fraction, this local ordering may extend over more than ten particle radii inside the suspension [54, 56]. In addition, the rheological properties are strongly affected in the layered region, leading in particular to significant wall slip. As previously mentioned, the current suspensions are composed of bidisperse particles to reduce the strength and extension of such layering. Nevertheless, local ordering is still observed in the vicinity of the walls, over a shorter extension though. Following Ref. [40], the local volume fraction is computed using a surface-averaging procedure:

$$\phi(y) = \frac{1}{L_x \times L_z} \iint_{\{\text{plane } y\}} \sum_{p \in \mathcal{D}} \chi_p(\mathbf{x}) \mathrm{d}x \mathrm{d}z \tag{49}$$

where $\chi_p(\mathbf{x})$ is the particle indicator function and integration is performed over the plane of constant height y. From Eq. (49), the bulk volume fraction may be computed as $\phi_{bulk} = 1/L_y \int_{-L_y/2}^{+L_y/2} \phi(y) \mathrm{d}y$. In Fig. 20, the time-averaged volume fraction profile is displayed for a suspension with $\phi_{bulk} = 0.42$. Particle ordering is observed close to the walls and decays over a length of a few particle radius units.

Based on the variation of the local volume fraction, the simulation domain may be split into a wall region and a core region. In the former region, the time-averaged volume fraction varies with the distance to the wall with a typical length scale $a_1 + a_2$, while in the latter region the volume fraction is approximately constant and the particle velocity profile is nearly linear. The results shown in the following are averaged over the core region only, which is defined for all volume fractions as the positions farther from the wall than $H_{layer} = 5a_1$. Specifically, the core volume fraction is computed as the average of the local volume fraction from Eq. (49):

$$\phi_{core} = \frac{1}{L_y - 2H_{layer}} \int_{-L_y/2+H_{layer}}^{L_y/2-H_{layer}} \phi(y) \mathrm{d}y \tag{50}$$

As shown in Table 8, the core volume fraction is always higher than the bulk volume fraction, meaning that the average volume fraction in the wall region is lower than the bulk volume fraction.

The core shear rate $\dot{\gamma}_{core}$ is determined at each time step from a linear regression of the particle velocity distribution of the particles situated inside the core region (Table 8). The core shear rate is always lower than the nominal shear rate $\dot{\gamma}_0$ as computed from the velocity of the wall, showing that wall slip occurs at the scale of the wall region.

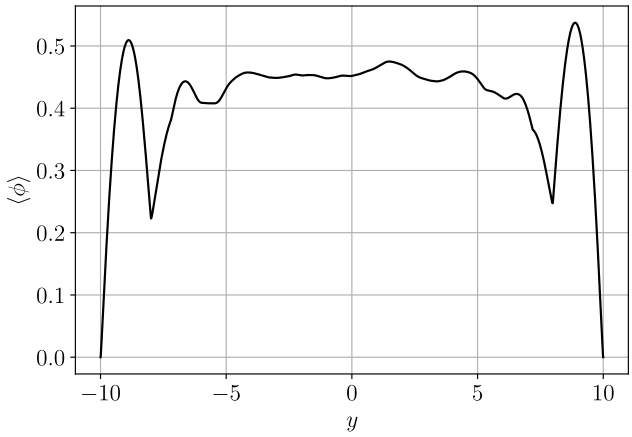

Fig. 20. Steady volume fraction profile in steady plane Couette flow for $\phi_{bulk} = 0.42$.

The bulk stress in the suspension is usually defined as:

$$\boldsymbol{\Sigma} = -P\boldsymbol{\delta} + \eta\dot{\gamma}\left(\boldsymbol{e}_x \otimes \boldsymbol{e}_y + \boldsymbol{e}_y \otimes \boldsymbol{e}_x\right) + \boldsymbol{\Sigma}^h + \boldsymbol{\Sigma}^c \tag{51}$$

where the last two terms respectively stand for the hydrodynamic and contact contributions of the particles to the stress, and are computed from the hydrodynamic stresslet (Eqs. (12) and (13)) and contact forces (see Supplementary Material) on the particles in the core region:

$$\begin{aligned}
\boldsymbol{\Sigma}^h &= \frac{1}{V_{core}} \sum_{p\in\mathcal{D}_{core}} \left(\boldsymbol{S}_p^{FDM} + \boldsymbol{S}_p^{SG} + \frac{s_p^{FDM} + s_p^{SG}}{3}\boldsymbol{\delta} \right) = \frac{1}{V_{core}} \sum_{p\in\mathcal{D}_{core}} \boldsymbol{S}_p^H \\
\boldsymbol{\Sigma}^c &= \frac{1}{V_{core}} \sum_{p\in\mathcal{D}_{core}} \sum_{\{p'\}\in\mathcal{D}_{core}} \frac{1}{2}\frac{a_p}{a_p + a'_p} \left(\mathbf{F}^{p'\to p} \otimes \boldsymbol{x}^{(pp')} + \boldsymbol{x}^{(pp')} \otimes \mathbf{F}^{p'\to p} \right) = \frac{1}{V_{core}} \sum_{p\in\mathcal{D}_{core}} \boldsymbol{S}_p^c
\end{aligned} \tag{52}$$

where $\boldsymbol{S}_p^H = \boldsymbol{S}_p^h + s_p^h\boldsymbol{\delta}/3$, and $\boldsymbol{x}^{(pp')} = \boldsymbol{x}^{(p')} - \boldsymbol{x}^{(p)}$. It should be stressed that $\boldsymbol{S}_p^H$ and $\boldsymbol{S}_p^c$ are now both not traceless. The pressure term in Eq. (51) may be computed from the pressure outside of the particles and will not be addressed in the following.

In the current work, in line with the computation of the volume fraction, and following Ref. [40], the local particle contribution to the stress is computed with the assumption that the particle stresslet is homogeneously distributed over the particle domain with volume V_p:

$$\boldsymbol{\Sigma}^{h,c}(y) = \frac{1}{L_x \times L_z} \iint_{\{\text{plane } y\}} \sum_p \frac{\mathbf{S}_p^{H,c}}{V_p} \chi_p(\mathbf{x}) \mathrm{d}x\mathrm{d}z \tag{53}$$

The local stress is then averaged over the core region in the same way as the volume fraction in Eq. (50), yielding the core stress. The reduced bulk viscosity reads:

$$\eta^s = \frac{\Sigma_{xy}^{core}}{\eta\left\langle\dot{\gamma}_{core}\right\rangle} = 1 + \frac{\left\langle\Sigma_{xy}^{h,core} + \Sigma_{xy}^{c,core}\right\rangle}{\eta\left\langle\dot{\gamma}_{core}\right\rangle} \tag{54}$$

where $\langle\cdot\rangle$ denotes time-averaging over the steady flow.

The computed viscosity is displayed as a function of the core volume fraction in Fig. 21. It is compared to data obtained using the Force Coupling Method [75], or by the FDM with standard sub-grid corrections [32]. The different sets of data are in close agreement, with slight but significant discrepancy for the high volume fraction range ($\phi_{core} \geq 0.45$) where the viscosity from the current data set is a bit lower than the data from

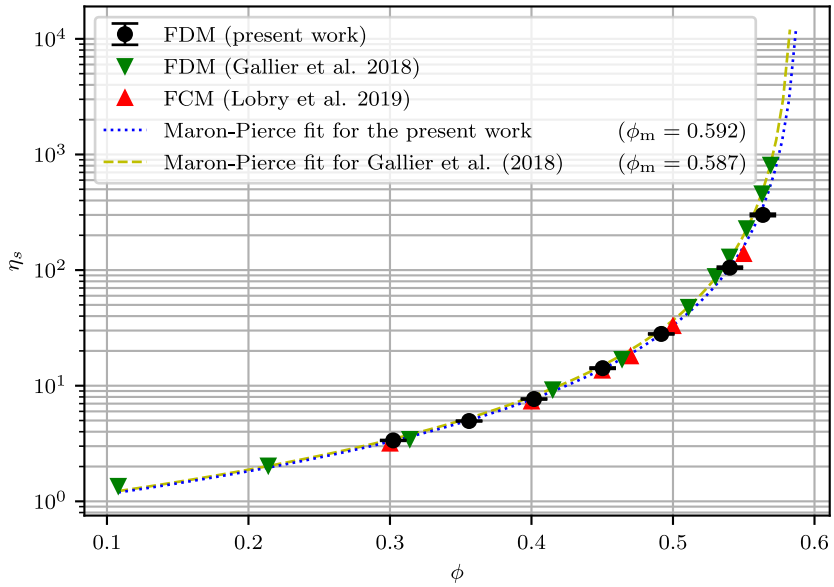

Fig. 21. Suspension viscosity in the core region as a function of the core volume fraction. Symbols: simulation data; dashed lines: Maron-Pierce fits. In the current work, $\alpha = 0.803$.

Ref. [32]. This discrepancy may be explained by the different sizes of the simulation volume used in either of the two studies. While the channel width is at most $L_y = 25a_1$ in this article, Gallier et al. (2018) chose a wider channel $L_y = 40a_1$. A slight residual ordering effect could be responsible for the lower viscosity in the current simulations.

A classic Maron-Pierce correlation law is fitted to the two FDM data sets:

$$\eta_s = \frac{\alpha}{\left(1 - \phi/\phi_m\right)^2} \tag{55}$$

where α and ϕ_m are left as fitting parameters. The latter, i.e. the jamming volume fraction, is known to significantly depend on the friction coefficient and takes decreasing values from 0.64 to approximately 0.55 as the friction coefficient increases from 0 to 10, although it hardly varies for $\mu_s \geq 2$ [23, 70, 71, 75]. In the current work, the fitting procedure yields close values for both the FDM data sets, i.e. approximately 0.59, in good agreement with data from the literature for the same friction coefficient.

Normal stresses, as well as their contact contribution, have been computed too. In the following, they are compared to correlation laws [76] that were obtained by a fitting procedure to the earlier numerical data mentioned above [32, 75]. They are displayed as normalized quantities:

$$\hat{N}_1 = \frac{\Sigma_{xx} - \Sigma_{yy}}{\Sigma_{xy}} \qquad \hat{N}_2 = \frac{\Sigma_{yy} - \Sigma_{zz}}{\Sigma_{xy}} \tag{56}$$

and:

$$\hat{\Sigma}^c_{11} = \frac{\Sigma^c_{xx}}{\Sigma_{xy}} \qquad \hat{\Sigma}^c_{22} = \frac{\Sigma^c_{yy}}{\Sigma_{xy}} \qquad \hat{\Sigma}^c_{33} = \frac{\Sigma^c_{zz}}{\Sigma_{xy}} \tag{57}$$

The first and second normal stress differences are displayed in Fig. 22 (top), together with the corresponding data from Refs. [32, 75] and the correlation laws. Again, the agreement with earlier simulations is satisfactory, although with a larger discrepancy for the first normal stress difference. However, the latter quantity is smaller and subject to relatively higher fluctuations. Finally, the contact contributions to the normal stresses are important quantities, since they are expected to play a key role in the shear-induced particle migration [77, 78]. They are displayed in Fig. 22 (bottom). Again, they agree with the correlation laws from Ref. [76].

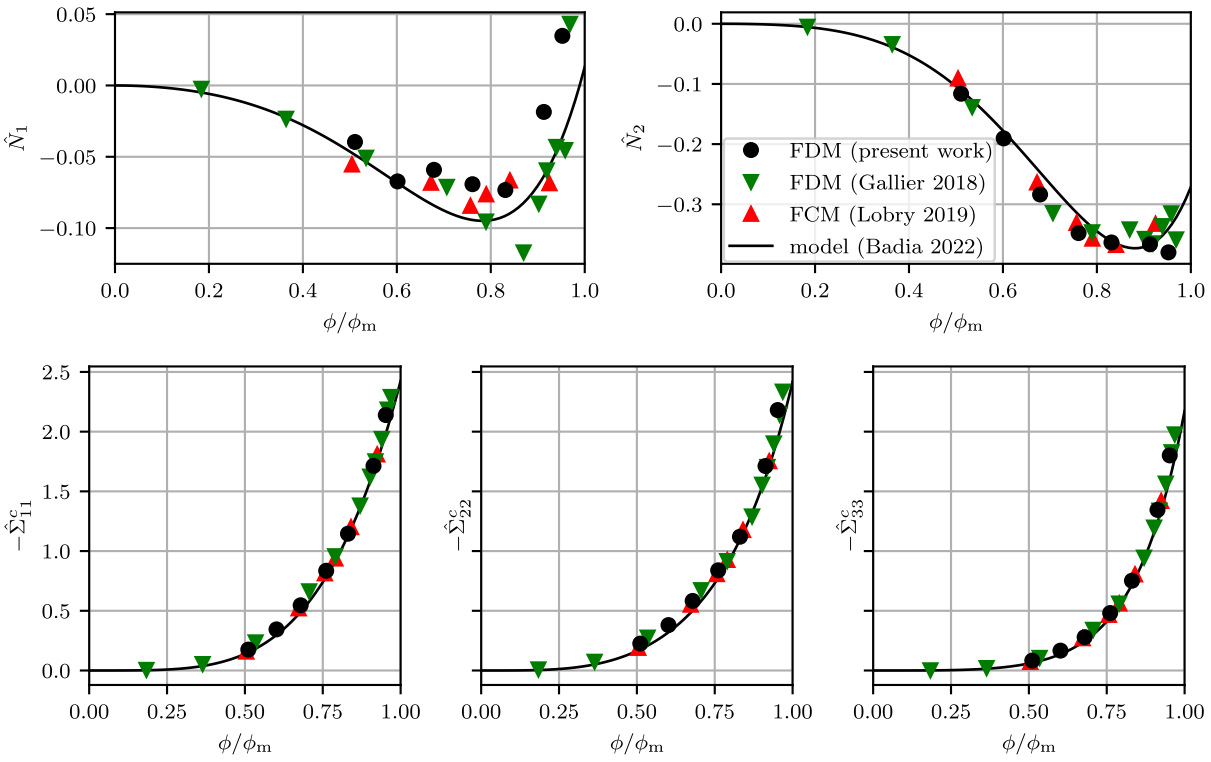

Fig. 22. (top) First and second normal stress differences $\hat{N}_1$ and $\hat{N}_2$. (bottom) Contact forces contributions to normal stresses. Symbol: simulation data. Plain line: correlation law from Ref. [76].

6.2. Pressure-driven flow of a suspension

We turn now to the pressure-driven flow of a quite concentrated suspension ($\phi_{bulk} = 0.45$). The flow geometry is the same as in Section 5.2.3 and the dimensions of the simulation domain are $(L_x/a_1, L_y/a_1, L_z/a_1) = (40, 40, 20)$. As in the previous case, a homogeneous pressure gradient is applied at each point of the simulation volume:

$$\boldsymbol{\nabla} P_0 = \frac{\mathrm{d}P_0}{\mathrm{d}x}\boldsymbol{e}_x = -8\eta\frac{U_c}{L_y^2}\boldsymbol{e}_x \tag{58}$$

The time step has been chosen sufficiently small for the particle dynamics to be conveniently computed: $\Delta t = 10^{-3} L_y/(2U_c)$. In such a flow, the shear stress is proportional to the distance from the channel center plane, resulting in shear-induced particle migration [39, 79, 80, 40]. Particles are driven toward the center of the channel until the steady velocity and volume fraction profiles are established. In the following, we address the steady flow when migration has ended, i.e. after a time $T \approx 1500 L_y/(2U_c)$.

The volume fraction and stress profiles are computed as in the previous section (Eqs. (49), (51) and (53)), and the particle velocity profile $\mathbf{u}_p(y)$ is computed from the velocity of the particles following Ref. [40]:

$$\phi\,(y)\,\mathbf{u}_p\,(y) = \frac{1}{L_x \times L_z}\iint_{\{plane\ y\}} \sum_p \mathbf{U}_p \chi_p(\mathbf{x})\mathrm{d}x\mathrm{d}z \tag{59}$$

In this section, we are not interested in variations at a scale smaller than a particle radius. As a consequence, the different profiles are re-sampled at positions y_n such that $y_{n+1} - y_n = \Delta y = a_1$. To this purpose, the fine-scale profiles in Eqs. (49), (53) and (59) are averaged over each position bin, e.g. for the volume fraction:

$$\phi^{coarse} = \frac{1}{\Delta y}\int_{y_n-\Delta y/2}^{y_n+\Delta y/2} \phi\,(y)\,\mathrm{d}y \tag{60}$$

All quantities are averaged over a time interval $\Delta T = 400 L_y/(2U_c)$ in the steady regime. In addition, the following dimensionless quantities are considered:

$$\mathbf{u}_p^* = \frac{\mathbf{u}_p}{-\frac{L_y^2}{4\eta}\frac{\mathrm{d}P_0}{\mathrm{d}x}} = \frac{\mathbf{u}_p}{2U_c} \quad , \qquad y^* = \frac{y}{L_y} \tag{61}$$

Fig. 23 shows the steady solid volume fraction and particle velocity profiles. As expected, a volume fraction gradient toward the center of the channel is observed. This results in a blunted velocity profile that differs from the usual parabolic profile observed in the pressure-driven flow of a homogeneous Newtonian liquid. Indeed, in any case, the shear stress in a plane pressure-driven flow is proportional to the y-coordinate. In the current case, the volume fraction increase toward the channel center increases the shear viscosity at the center (see Fig. 21), and consequently to a lower shear rate compared to the constant viscosity case.

The fine-scale volume fraction profile displays particle ordering at the walls, despite the precaution of mixing particles of two different sizes. The extension of the ordering area is approximately $3a_1$, and is less apparent when considering the coarse profiles. It results in a brutal variation of the particle velocity over the same extension. We note also that the particle velocity does not vanish at the walls. The rapid variation of the particle velocity at the wall and the non-zero value at the walls may be termed as wall slip and is classically observed in experiments [81].

We note that the local volume fraction at the channel center slightly exceeds the jamming volume fraction $\phi_m = 0.592$ that was estimated from the homogeneous suspension viscosity (Fig. 21). This occurs over a quite narrow area, approximately $6a_1$ in width, where the actual shear rate is close to 0, with a mean value $\bar{\dot{\gamma}} \approx 7 \cdot 10^{-4} \times 2U_c/Ly$, to be compared to the maximum value at the walls $\dot{\gamma}_{max} \approx 0.2 \times 2U_c/Ly$. The suspension is thus not completely jammed in this area, even though the shear rate is very low.

We now compare the steady velocity and volume fraction profiles to theoretical computations using the so-called Suspension Balance Model (SBM) [39, 82, 83, 77, 78]. In the frame of this model, particle migration is induced by stress gradients. The precise nature of the stresses that should be considered as the driving force is still an open question [78]. In the current article, the contact force contribution to stress is assumed to play this role. The version of the SBM that we use is explained in detail in Ref. [76], and it is briefly summarized in the Supplementary Material. It involves the material functions that were determined from the discrete simulations and mentioned in the previous section. The steady velocity and volume fraction

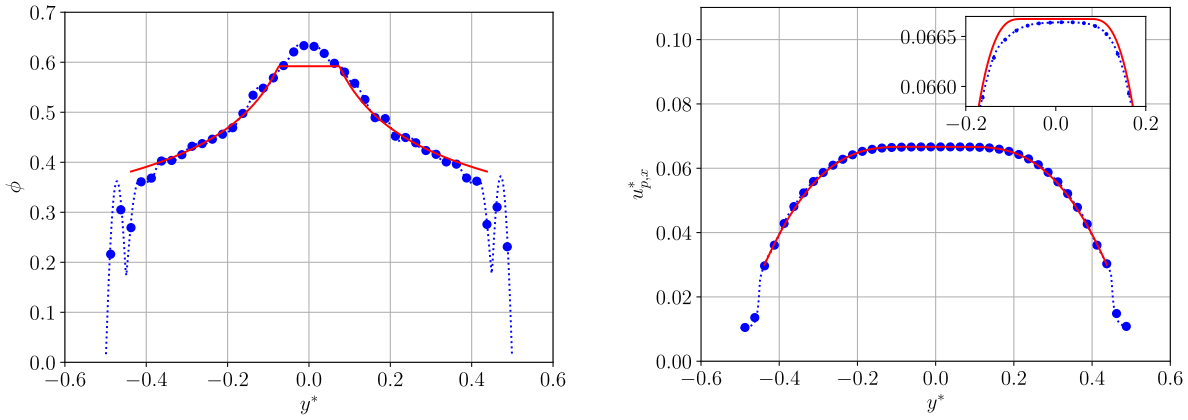

Fig. 23. (left) Steady volume fraction and (right) particle velocity profiles. $\phi_{bulk} = 0.45$. Symbol: simulations (coarse sampling). Dotted line: simulations (fine sampling). Plain line: Suspension Balance Model.

profiles obey the following equations, which are derived in the Supplementary Material:

$$\frac{\mathrm{d}u^*_{p,x}}{\mathrm{d}y^*} = -\frac{4}{\eta_s\left(\phi_r(y^*)\right)}y^* \tag{62a}$$

$$\frac{\mathrm{d}\phi_r}{\mathrm{d}y^*} = -\frac{\hat{\Sigma}^c_{22}}{y^*\dfrac{\mathrm{d}\hat{\Sigma}^c_{22}}{\mathrm{d}\phi_r}} \tag{62b}$$

with the constraint that the total particle volume is kept constant, i.e.:

$$\int_{-1/2}^{+1/2}\phi_r \mathrm{d}y^* = \frac{\phi_{bulk}}{\phi_m} \tag{63}$$

where $\phi_r = \phi/\phi_m$. Eq. (62a) states that the shear stress is driven by the pressure gradient, while Eq. (62b) controls the steady volume fraction profile.

Once Eqs. (62b) and (63) are solved, the velocity profile is simply determined by integration of Eq. (62a). It should be noted that the SBM as presented here suffers important drawbacks (see Ref. [84] for a discussion). In particular, the steady-state volume fraction is allowed to exceed the jamming volume fraction ϕ_m, which is easily understood by inspection of Eq. (62b). The multiplying factor of $1/y^*$ in the RHS is negative so that ϕ increases as $|y^*|$ decreases. In addition, this factor does not vanish as $\phi/\phi_m \to 1$, so the volume fraction gradient diverges as $y^* \to 0$, and $\phi_r \to \infty$. To avoid this divergence, it has been proposed to slightly modify the expression of the particle flux with a non-local stress. This non-local stress may be induced by a suspension "temperature" [39], a force network [82], or the finite size of the particles [85]. In the current article, we follow a simple empirical idea: we postulate that the particle flux must be vanishing as soon as ϕ reaches ϕ_m. As a consequence, a jammed zone where $\phi = \phi_m$ develops in the vicinity of the channel center plane. Finally, to avoid the difficulties associated with particle layering and wall slip, Eqs. (62a), (62b) and (63) are solved outside the layering region, i.e. at a distance from the bounding walls larger than $2.5a_1$, and taking into account only the mean volume fraction inside this region. The steady volume fraction and velocity profiles are displayed in Fig. 23.

The simulation data and the SBM predictions are in close agreement, both for the velocity and volume fraction profiles, except in the direct vicinity of the boundaries and at the channel center. As already mentioned, the discrepancies at the walls are connected to particle layering, and we now shortly address the central region. The jammed zone extends over a width approximately equal to $6a_1$. In this area, the volume fraction from the simulations is larger than the jamming volume fraction ϕ_m, and reaches approximately the value 0.63. This may appear surprising, since the shear rate from the averaged velocity profile does not vanish, except at the exact center plane. Nonetheless, as already noted by Yeo and Maxey (2011) in their simulations of monosized suspensions in Poiseuille flow [40], velocity fluctuations never vanish, so they may play a significant role in the central region, in particular for the enhanced suspension concentration. In the same line, Yeo and Maxey (2011) evidenced a variation of the pair distribution function at the center of the channel, compared to the bulk suspension, possibly revealing a degree of ordering. We also note that, in their experiments concerning Brownian suspensions, Gao et al. (2010) [86] measured ordering at the center of a Poiseuille flow. A detailed study of the suspension structure may be useful, although not easy due to the small extension of the area of interest. Finally, it should be noted that recent experiments evidenced that the volume fraction could exceed the shear jamming volume fraction at the centerline of the channel [87]. 2D simulations of suspensions in Kolmogorov flow [36] also showed such an increase in the particle area fraction in the regions where the shear rate vanishes.

More generally, this part of the flow raises questions: the shear rate vanishes, but finite velocity fluctuations [40] suggest that the suspension is not completely frozen. In that part of the flow, it is likely that, despite the observed residual deformation rate, the usual relation between stress and shear rate may not hold anymore, allowing the particles to hold the pressure applied by the material outside this region in the absence of a significant deformation rate. We note that Lecampion and Garagash (2014) [88] adapted the SBM to the frictional rheology proposed by Boyer et al. (2011) [89], including a compressible jammed state.

According to this model, the volume fraction in the jammed region may exceed ϕ_m up to the random close packing $\phi_{rcp} \approx 0.64$. The underlying mechanism that is responsible for such a compressible jammed state is an open question. It may be akin to the "tapping" of granular material, which may originate in stress fluctuations in the current case.

Another issue is the failure of the SBM at the center of the channel which is usually observed for smaller volume fractions. Experiments [79, 80] and simulations [40] show that, for bulk volume fractions lower than typically 0.3, the volume fraction at the center of the channel keeps lower than ϕ_m, while the raw SBM predicts that ϕ reaches ϕ_m whatever the bulk volume fraction. As previously mentioned, various modifications of the SBM were proposed to overcome these issues, often involving a non-local stress, which, as a consequence, does not vanish at the centerline. In particular, it may be argued [85] that the shear stress vanishes at the centerline in an average sense only: the shear stress may take different values at the walls, resulting in a fluctuating linear stress profile. As a consequence, the shear stress value at the centerline needs not to vanish instantaneously, inducing finite values of the root mean square shear rate and of the normal stresses. The simulation method of interest in the current article should allow new insights into this area. In particular, it will allow detailed stress balance on the particle phase.

7. Conclusion

We have proposed a Fictitious Domain Method well suited to the simulations of non-Brownian suspensions in nonlinear flows, including sub-grid corrections, based on a previously developed method [16]. The conditions for the sub-grid corrections not to involve the ambient flow while keeping the necessary frame indifference have been derived. They require the flow induced by the rigid body motion of a particle pair in a fluid at rest or in an ambient linear flow to be properly accounted for by the solver alone, without the need for sub-grid corrections. Once the method has been implemented in the CFD toolbox OpenFOAM, the conditions have been shown to apply within a good approximation. Then, the sub-grid correction matrix has been built in such a way that those conditions exactly hold. As for the method validation, several flows that involve one to three particles in various linear and nonlinear flows have been computed and compared to accurate computations from the literature. The material functions of a sheared suspension have been computed as well for different values of the particle volume fraction and compared to data from the literature. Finally, the pressure-driven flow of a suspension in a channel has been computed, and the velocity and volume fraction profiles have been compared to computations based on the Suspension Balance Model.

The novelty of the method is to be found in the computation of the sub-grid corrections. While the current implementation is based on the computation of the flow using the finite volume method, the frame-invariant correction matrix may be determined and applied without loss of accuracy using any solver (finite difference, finite element, smooth particle method, lattice Boltzmann method, ...) provided that the conditions mentioned above hold reasonably well. If those conditions would only loosely hold, the frame-invariant sub-grid corrections as computed in the current article would certainly still allow tackling nonlinear flows, although probably at the cost of reduced accuracy.

Several questions concerning the transport of particles in slow flows remain open, which involve nonlinear flows, among which a few have been mentioned in the last section. We think that the numerical method that was developed in the current article will allow us to tackle those problems with confidence.

Acknowledgements

This work was supported by the French National Agency (ANR) under the program Blanc AMARHEO (ANR-18-CE06-0009-01).

This work was also supported by the French government, through the UCAJEDI Investments in the Future project managed by the National Research Agency (ANR) under reference number ANR-15-IDEX-01. The authors are grateful to the OPAL infrastructure from Université Côte d'Azur and the Université Côte d'Azur's Center for High-Performance Computing for providing resources and support.

The authors are pleased to acknowledge Stany Gallier for fruitful discussions. They warmly thank Maeva Antoine for her technical help concerning the HPC facilities and more generally for her unwavering support.

Appendix A. General form of the resistance tensors

In this section, the general form of the resistance matrices is recalled, both for the two-particle and the particle-wall hydrodynamic interactions. It holds for the theoretical matrices, as well as for the FDM matrices and the sub-grid correction matrices.

Appendix A.1. Particle pair

Considering two particles (p_1) and (p_2) with respective radii a_1 and a_2, and the unitary vector connecting their centers $\mathbf{d} = (\mathbf{x}_2 - \mathbf{x}_1) / \|\mathbf{x}_2 - \mathbf{x}_1\|$, the general form of the resistance tensors in Eq. (19) are:

$$
\begin{aligned}
A_{ij}^{(\alpha\beta)} &= X_{\alpha\beta}^{A} d_i d_j + Y_{\alpha\beta}^{A} \left(\delta_{ij} - d_i d_j\right) \\
B_{ij}^{(\alpha\beta)} &= Y_{\alpha\beta}^{B} \epsilon_{ijk} d_k \\
\tilde{B}_{ij}^{(\alpha\beta)} &= Y_{\alpha\beta}^{\tilde{B}} \epsilon_{ijk} d_k \\
C_{ij}^{(\alpha\beta)} &= X_{\alpha\beta}^{C} d_i d_j + Y_{\alpha\beta}^{C} \left(\delta_{ij} - d_i d_j\right) \\
G_{ijk}^{(\alpha\beta)} &= X_{\alpha\beta}^{G} \left(d_i d_j - \frac{1}{3}\delta_{ij}\right) d_k + Y_{\alpha\beta}^{G} \left(d_i \delta_{jk} + d_j \delta_{ik} - 2 d_i d_j d_k\right) \\
\tilde{G}_{ijk}^{(\alpha\beta)} &= X_{\alpha\beta}^{\tilde{G}} \left(d_j d_k - \frac{1}{3}\delta_{jk}\right) d_i + Y_{\alpha\beta}^{\tilde{G}} \left(d_j \delta_{ki} + d_k \delta_{ij} - 2 d_i d_j d_k\right) \\
H_{ijk}^{(\alpha\beta)} &= Y_{\alpha\beta}^{H} \left(d_i \epsilon_{jkm} d_m + d_j \epsilon_{ikm} d_m\right) \\
\tilde{H}_{ijk}^{(\alpha\beta)} &= Y_{\alpha\beta}^{\tilde{H}} \left(d_j \epsilon_{kim} d_m + d_k \epsilon_{jim} d_m\right) \\
M_{ijkl}^{(\alpha\beta)} &= \frac{3}{2} X_{\alpha\beta}^{M} \left(d_i d_j - \frac{1}{3}\delta_{ij}\right)\left(d_k d_l - \frac{1}{3}\delta_{kl}\right) + \frac{1}{2} Y_{\alpha\beta}^{M} \left(d_i \delta_{jl} d_k + d_j \delta_{il} d_k + d_i \delta_{jk} d_l + d_j \delta_{ik} d_l - 4 d_i d_j d_k d_l\right) + \\
&\quad + \frac{1}{2} Z_{\alpha\beta}^{M} \left(\delta_{ik}\delta_{jl} + \delta_{jk}\delta_{il} - \delta_{ij}\delta_{kl} + d_i d_j \delta_{kl} + \delta_{ij} d_k d_l + d_i d_j d_k d_l - d_i \delta_{jl} d_k - d_j \delta_{il} d_k - d_i \delta_{jk} d_l - d_j \delta_{ik} d_l\right) \\
P_{i}^{(\alpha\beta)} &= X_{\alpha\beta}^{P} d_i \\
Q_{ij}^{(\alpha\beta)} &= X_{\alpha\beta}^{Q} \left(d_i d_j - \frac{1}{3}\delta_{ij}\right)
\end{aligned}
\tag{A.1}
$$

where the different scalar coefficients $X_{\alpha\beta}^{A}$, ..., depend on a_1, a_2 and on the reduced distance between the surfaces of the particles $\xi = 2\|\mathbf{x}_2 - \mathbf{x}_1\| / (a_1 + a_2) - 2$.

The resistance matrix respects the symmetry originating in the Lorentz Reciprocal Theorem [38], thus:

$$
\begin{aligned}
A_{ij}^{\alpha\beta} &= A_{ji}^{\beta\alpha} & \tilde{B}_{ij}^{\alpha\beta} &= B_{ji}^{\beta\alpha} & C_{ij}^{\alpha\beta} &= C_{ji}^{\beta\alpha} \\
\tilde{G}_{ijk}^{\alpha\beta} &= G_{jki}^{\beta\alpha} & \tilde{H}_{ijk}^{\alpha\beta} &= H_{jki}^{\beta\alpha} & M_{ijkl}^{\alpha\beta} &= M_{lkij}^{\beta\alpha}
\end{aligned}
\tag{A.2}
$$

Then, from the definition of the terms, we obtain:

$$\begin{aligned}
&X^A_{\alpha\beta} = X^A_{\beta\alpha} && Y^A_{\alpha\beta} = Y^A_{\beta\alpha} && X^C_{\alpha\beta} = X^C_{\beta\alpha} \\
&X^M_{\alpha\beta} = X^M_{\beta\alpha} && Y^M_{\alpha\beta} = Y^M_{\beta\alpha} && Y^C_{\alpha\beta} = Y^C_{\beta\alpha} \\
&Y^{\tilde{B}}_{\alpha\beta} = -Y^B_{\beta\alpha} && X^{\tilde{G}}_{\alpha\beta} = X^G_{\beta\alpha} && Z^M_{\alpha\beta} = Z^M_{\beta\alpha} \\
&Y^{\tilde{G}}_{\alpha\beta} = Y^G_{\beta\alpha} && Y^{\tilde{H}}_{\alpha\beta} = Y^H_{\beta\alpha}
\end{aligned} \tag{A.3}$$

Moreover, the relations for $\lambda = \dfrac{a_2}{a_1}$ and λ^{-1}, which originates in geometrical symmetry, read:

$$\begin{aligned}
&X^A_{\alpha\beta}(s,\lambda) = X^A_{(3-\alpha)(3-\beta)}(s,\lambda^{-1}) && Y^A_{\alpha\beta}(s,\lambda) = Y^A_{(3-\alpha)(3-\beta)}(s,\lambda^{-1}) \\
&Y^B_{\alpha\beta}(s,\lambda) = -Y^B_{(3-\alpha)(3-\beta)}(s,\lambda^{-1}) && X^C_{\alpha\beta}(s,\lambda) = X^C_{(3-\alpha)(3-\beta)}(s,\lambda^{-1}) \\
&Y^C_{\alpha\beta}(s,\lambda) = Y^C_{(3-\alpha)(3-\beta)}(s,\lambda^{-1}) && X^G_{\alpha\beta}(s,\lambda) = -X^G_{(3-\alpha)(3-\beta)}(s,\lambda^{-1}) \\
&Y^G_{\alpha\beta}(s,\lambda) = -Y^G_{(3-\alpha)(3-\beta)}(s,\lambda^{-1}) && Y^H_{\alpha\beta}(s,\lambda) = Y^H_{(3-\alpha)(3-\beta)}(s,\lambda^{-1}) \\
&X^M_{\alpha\beta}(s,\lambda) = X^M_{(3-\alpha)(3-\beta)}(s,\lambda^{-1}) && Y^M_{\alpha\beta}(s,\lambda) = Y^M_{(3-\alpha)(3-\beta)}(s,\lambda^{-1}) \\
&Z^M_{\alpha\beta}(s,\lambda) = Z^M_{(3-\alpha)(3-\beta)}(s,\lambda^{-1}) && X^P_{\alpha\beta}(s,\lambda) = -X^P_{(3-\alpha)(3-\beta)}(s,\lambda^{-1}) \\
&X^Q_{\alpha\beta}(s,\lambda) = X^Q_{(3-\alpha)(3-\beta)}(s,\lambda^{-1})
\end{aligned} \tag{A.4}$$

Appendix A.2. Particle-wall interactions

The particle-wall resistance matrix reflects the linear relation between the stress moments on a particle (p) close to a wall and the generalized relative velocity of the particle. In the following, the wall is supposed to have zero angular velocity for the sake of simplicity. Any point of the wall moves with the velocity $\mathbf{U}_w$. A linear simple shear flow is assumed in the vicinity of the wall so that the undisturbed velocity reads:

$$\mathbf{u}_\infty(\mathbf{x}) = \mathbf{U}_w + \boldsymbol{\Omega}_\infty \times \mathbf{x} + \mathbf{E}_\infty \cdot \mathbf{x} \tag{A.5}$$

where the origin of the frame lies on the wall, and the usual relation between $\boldsymbol{\Omega}_\infty$ and $\mathbf{E}_\infty$ for a simple shear flow is assumed (see Fig. 6 as an example). The hydrodynamic stress moments on the particle read:

$$\boldsymbol{\mathcal{M}}_p = \begin{pmatrix} \mathbf{F}_p \\ \mathbf{T}_p \\ \mathbf{S}_p \\ s_p \end{pmatrix} = -\boldsymbol{\mathcal{R}}_w \cdot \begin{pmatrix} \mathbf{U}_p - \mathbf{u}_\infty(\mathbf{x_p}) \\ \boldsymbol{\Omega}_\mathbf{p} - \boldsymbol{\Omega}_\infty \\ -\mathbf{E}_\infty \end{pmatrix} = -\eta \begin{pmatrix} \mathbf{A}_w & \tilde{\mathbf{B}}_w & \tilde{\mathbf{G}}_w \\ \mathbf{B}_w & \mathbf{C}_w & \tilde{\mathbf{H}}_w \\ \mathbf{G}_w & \mathbf{H}_w & \mathbf{M}_w \\ \mathbf{P}_w & \mathbf{0} & \mathbf{0} \end{pmatrix} \cdot \begin{pmatrix} \mathbf{U}_p - \mathbf{u}_\infty(\mathbf{x_p}) \\ \boldsymbol{\Omega}_p - \boldsymbol{\Omega}_\infty \\ -\mathbf{E}_\infty \end{pmatrix} \tag{A.6}$$

We note that, due to the symmetry of the simple shear flow, the matrix $\mathbf{Q}_w$ yields no force dipole trace, so that it has been removed in Eq. (A.6). Finally, the same general form holds for the particle-wall interaction matrices $\mathbf{Mat}_w$ as for their two-particle counterpart $\mathbf{Mat}_{11}$ in Eqs. (A.1) and (A.3), provided $\mathbf{d}$ is now the unit vector normal to the wall directed into the wall. The resistance functions depend on the radius of the particle a and the reduced distance of the particle surface to the wall $\varepsilon = [(\mathbf{x}_w - \mathbf{x}_p) \cdot \mathbf{d}]/a - 1$, where $\mathbf{x}_w$ is the position of any point on the wall. Useful theoretical expressions for the said resistance functions are given in the Supplementary Material.

Appendix B. Determination of the Fictitious Domain solver resistance matrix

As recalled in Section 2.2, the standard sub-grid two-particle correction matrix (Eq. (19)) is computed as $\boldsymbol{\mathcal{R}}_{2p}^{SG} = \boldsymbol{\mathcal{R}}_{2p}^{th} - \boldsymbol{\mathcal{R}}_{2p}^{FDM}$, where $\boldsymbol{\mathcal{R}}_{2p}^{th}$ stands for the theoretical two-particle resistance matrix. The standard sub-grid particle-wall correction matrix (Eq. (A.6)) is defined in the same way. This section deals with the computation of the Fictitious Domain solver resistance matrices $\boldsymbol{\mathcal{R}}_{2p}^{FDM}$ and $\boldsymbol{\mathcal{R}}_{W}^{FDM}$.

The whole set of two-particle FDM resistance functions is deduced from the computation of 8 particular arrangements of the particles, velocities of the particles, and ambient flow. Each arrangement was evaluated for 4 different domain sizes of a cubic domain ($L/(a_1 = 1.0) = 20$, 30, 40, 50), and the asymptotic values for infinite domain size were estimated, to get rid of long-range hydrodynamic interactions with the bounding walls. This procedure was repeated for each value of the reduced distance ξ of interest. In Fig. B.24, an example of the obtained fits for two resistance functions is shown.

The same procedure was followed to build the whole particle-wall resistance matrix as written in Eq. (A.6), except that fewer arrangements – namely 5 – were requested. In Fig. B.25 we show as an example the measurement of X^A and Y^A, respectively: we can observe for Y^A the difference between the expressions based on the lubrication approximation gathered by Yeo and Maxey (2010) [6] from the literature and the expansions proposed by Chaoui and Feuillebois (2003) [60], which are recalled in the Supplementary Material. Using the latter (for Y^A, Y^B and Y^C) allows us to precisely determine the ε-range for which the sub-grid corrections are needed, i.e. starting from $\varepsilon < 0.3$ for the X terms and from $\varepsilon < 0.15$ for the Y terms.

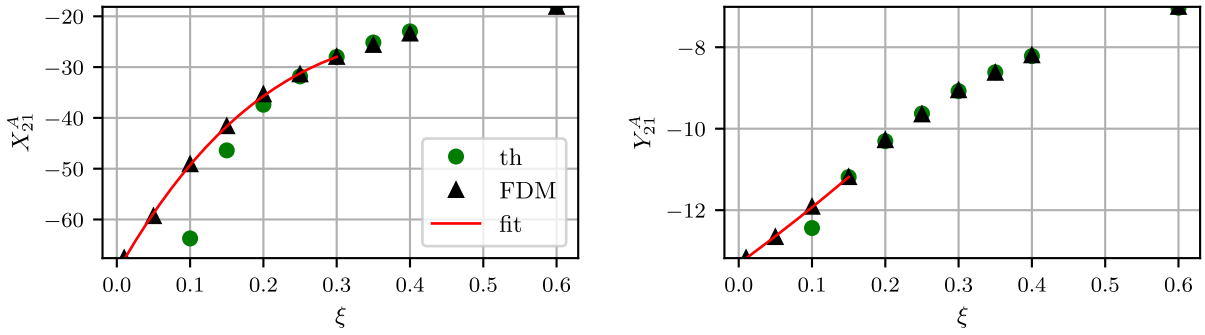

Fig. B.24. Two-particle resistance functions X_{21}^A and Y_{21}^A. (●) Theoretical function. (▲) FDM function. Plain line: fit to the FDM function.

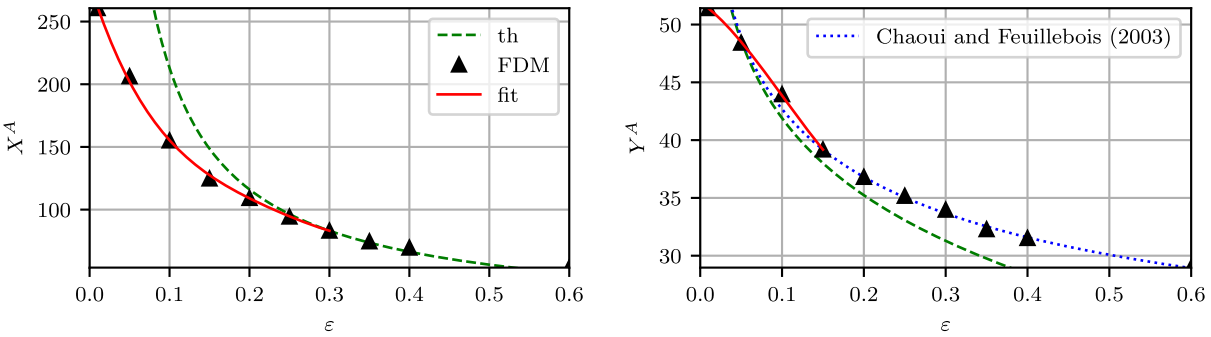

Fig. B.25. Particle-wall resistance functions X^A and Y^A. (▲) FDM function. Dashed line: theoretical function from the lubrication approximation. Dotted line: theoretical functions by Chaoui and Feuillebois (2003) [60]. Plain line: fit to the FDM function.

Appendix C. Building the two-particle frame-invariant sub-grid correction matrix

In the whole section, the sub-grid correction matrix is considered. The superscript "SG" has been omitted for the sake of simplicity.

Appendix C.1. Constraints to the frame-invariant sub-grid correction matrix

The whole set of relations that follow from Eq. (20) is quoted below. Only the relations for the $(\cdot)_{11}$ and $(\cdot)_{12}$ terms are shown: the remaining ones are obtained by simply replacing $(\cdot)_{11}$ by $(\cdot)_{21}$ and $(\cdot)_{12}$ by $(\cdot)_{22}$.

$$X_{11}^{A} + X_{12}^{A} = 0$$

$$Y_{11}^{A} + Y_{12}^{A} = 0$$

$$\frac{r}{2}\left(Y_{11}^{A} - Y_{12}^{A}\right) - \left(Y_{11}^{\tilde{B}} + Y_{12}^{\tilde{B}}\right) = 0$$

$$Y_{11}^{B} + Y_{12}^{B} = 0$$

$$X_{11}^{C} + X_{12}^{C} = 0$$

$$\frac{r}{2}\left(Y_{11}^{B} - Y_{12}^{B}\right) + \left(Y_{11}^{C} + Y_{12}^{C}\right) = 0$$

$$X_{11}^{G} + X_{12}^{G} = 0$$

$$Y_{11}^{G} + Y_{12}^{G} = 0$$

$$\frac{r}{2}\left(Y_{11}^{G} - Y_{12}^{G}\right) - \left(Y_{11}^{H} + Y_{12}^{H}\right) = 0$$

$$\frac{r}{2}\left(-X_{11}^{A} + X_{12}^{A}\right) + \left(X_{11}^{\tilde{G}} + X_{12}^{\tilde{G}}\right) = 0$$

$$\frac{r}{2}\left(-Y_{11}^{A} + Y_{12}^{A}\right) + 2\left(Y_{11}^{\tilde{G}} + Y_{12}^{\tilde{G}}\right) = 0$$

$$\frac{r}{2}\left(-Y_{11}^{B} + Y_{12}^{B}\right) - 2\left(Y_{11}^{\tilde{H}} + Y_{12}^{\tilde{H}}\right) = 0$$

$$\frac{r}{2}\left(-X_{11}^{G} + X_{12}^{G}\right) + \frac{3}{2}\left(X_{11}^{M} + X_{12}^{M}\right) = 0$$

$$\frac{r}{2}\left(-Y_{11}^{G} + Y_{12}^{G}\right) + \left(Y_{11}^{M} + Y_{12}^{M}\right) = 0$$

$$\frac{1}{2}\left(Z_{11}^{M} + Z_{12}^{M}\right) = 0$$

$$X_{11}^{P} + X_{12}^{P} = 0$$

$$\frac{r}{2}\left(-X_{11}^{P} + X_{12}^{P}\right) + \left(X_{11}^{Q} + X_{12}^{Q}\right) = 0$$

Appendix C.2. Expressions of the frame-invariant sub-grid correction matrix coefficients

Putting together the previous relations and imposing the relations that originate from Lorentz reciprocal theorem, we can get a list of relations between the different resistance functions. We choose as the only ten independent resistance functions that need to be considered the following: X_{21}^A, Y_{21}^A, Y_{21}^B, X_{21}^C, Y_{11}^C, X_{11}^G, Y_{11}^G, Y_{21}^H, X_{12}^P, X_{21}^P; the expressions of the remaining ones are:

$$
\begin{aligned}
X_{11}^A &= -X_{21}^A \\
X_{12}^A &= X_{21}^A \\
X_{22}^A &= -X_{21}^A
\end{aligned}
\qquad
\begin{aligned}
Y_{11}^A &= -Y_{21}^A \\
Y_{12}^A &= Y_{21}^A \\
Y_{22}^A &= -Y_{21}^A
\end{aligned}
$$

$$
\begin{aligned}
X_{11}^C &= -X_{21}^C \\
X_{12}^C &= X_{21}^C \\
X_{22}^C &= -X_{21}^C
\end{aligned}
\qquad
\begin{aligned}
Y_{12}^C &= -Y_{11}^C + rY_{21}^B - r^2Y_{21}^A \\
Y_{21}^C &= -Y_{11}^C + rY_{21}^B - r^2Y_{21}^A \\
Y_{22}^C &= Y_{11}^C - 2rY_{21}^B + r^2Y_{21}^A
\end{aligned}
$$

$$
\begin{aligned}
Y_{11}^B &= -Y_{21}^B + rY_{21}^A \\
Y_{12}^B &= Y_{21}^B - rY_{21}^A \\
Y_{22}^B &= -Y_{21}^B
\end{aligned}
\qquad
\begin{aligned}
Y_{11}^{\tilde{B}} &= Y_{21}^B - rY_{21}^A \\
Y_{12}^{\tilde{B}} &= -Y_{21}^B \\
Y_{21}^{\tilde{B}} &= -Y_{21}^B + rY_{21}^A \\
Y_{22}^{\tilde{B}} &= Y_{21}^B
\end{aligned}
$$

$$
\begin{aligned}
X_{12}^G &= -X_{11}^G \\
X_{21}^G &= -X_{11}^G - rX_{21}^A \\
X_{22}^G &= X_{11}^G + rX_{21}^A
\end{aligned}
\qquad
\begin{aligned}
X_{11}^{\tilde{G}} &= X_{11}^G \\
X_{12}^{\tilde{G}} &= -X_{11}^G - rX_{21}^A \\
X_{21}^{\tilde{G}} &= -X_{11}^G \\
X_{22}^{\tilde{G}} &= X_{11}^G + rX_{21}^A
\end{aligned}
$$

$$
\begin{aligned}
Y_{12}^G &= -Y_{11}^G \\
Y_{21}^G &= -Y_{11}^G - \frac{1}{2}rY_{21}^A \\
Y_{22}^G &= Y_{11}^G + \frac{1}{2}rY_{21}^A
\end{aligned}
\qquad
\begin{aligned}
Y_{11}^{\tilde{G}} &= Y_{11}^G \\
Y_{12}^{\tilde{G}} &= -Y_{11}^G - \frac{1}{2}rY_{21}^A \\
Y_{21}^{\tilde{G}} &= -Y_{11}^G \\
Y_{22}^{\tilde{G}} &= Y_{11}^G + \frac{1}{2}rY_{21}^A
\end{aligned}
$$

$$
\begin{aligned}
Y_{11}^H &= -Y_{21}^H - \frac{1}{2}r^2Y_{21}^A + \frac{1}{2}rY_{21}^B \\
Y_{12}^H &= Y_{21}^H + \frac{1}{2}r^2Y_{21}^A + rY_{11}^G - \frac{1}{2}rY_{21}^B \\
Y_{22}^H &= -Y_{21}^H - \frac{1}{2}r^2Y_{21}^A - rY_{11}^G
\end{aligned}
\qquad
\begin{aligned}
Y_{11}^{\tilde{H}} &= -Y_{21}^H - \frac{1}{2}r^2Y_{21}^A + \frac{1}{2}rY_{21}^B \\
Y_{12}^{\tilde{H}} &= Y_{21}^H \\
Y_{21}^{\tilde{H}} &= Y_{21}^H + \frac{1}{2}r^2Y_{21}^A + rY_{11}^G - \frac{1}{2}rY_{21}^B \\
Y_{22}^{\tilde{H}} &= -Y_{21}^H - \frac{1}{2}r^2Y_{21}^A - rY_{11}^G
\end{aligned}
$$

$$
\begin{aligned}
X_{11}^P &= -X_{12}^P \\
X_{22}^P &= -X_{21}^P
\end{aligned}
$$

Appendix D. The particle-wall frame-invariant sub-grid correction matrix

In this section, the expression of the sub-grid correction matrix as written in Eq. (A.6) is simplified in the same line as the two-particle matrix in Section 3. The expression of the theoretical stress moments is first split into two contributions:

$$\begin{pmatrix} \mathbf{F}_p \\ \mathbf{T}_p \\ \mathbf{S}_p \\ s_p \end{pmatrix} = -\boldsymbol{\mathcal{R}}_w \cdot \begin{pmatrix} \mathbf{U}_p - \mathbf{U}_w \\ \boldsymbol{\Omega}_p \\ \mathbf{0} \end{pmatrix} - \boldsymbol{\mathcal{R}}_w \cdot \begin{pmatrix} -\boldsymbol{\Omega}_\infty \times \mathbf{x}_p - \mathbf{E}_\infty \cdot \mathbf{x}_p \\ -\boldsymbol{\Omega}_\infty \\ -\mathbf{E}_\infty \end{pmatrix} \tag{D.1}$$

The first term of the RHS of Eq. (D.1) is the stress moments vector on the moving particle as the liquid far from the wall moves at the same velocity $\mathbf{U}_w$ as the wall. Concerning the second term of the RHS, we recall here that $\boldsymbol{\Omega}_\infty$ and $\mathbf{E}_\infty$ are not independent, and that they define a simple shear flow parallel to the wall. The whole term stands for the stress moment on a particle at rest, where the wall is also at rest, and the liquid far from the wall experiences a simple shear flow. Again, the latter contribution does not involve any lubrication flow between the particle and the wall, so the corresponding resistance functions do not diverge as the distance of the particle surface to the wall goes to zero. It is thus expected to be well accounted for by the Fictitious Domain Method without the need for specific sub-grid corrections.

As in the case of the two-particle sub-grid correction matrix, we check that this ambient flow contribution could be neglected. To this purpose, a particle is held at rest in a simple shear flow close to the fixed wall (Fig. 6), and the force friction factor $\hat{F}^{\dot{\gamma}}$ and the torque friction factor $\hat{T}^{\dot{\gamma}}$, as defined below, are computed without any sub-grid correction:

$$\begin{aligned} \hat{F}^{\dot{\gamma}} &= \frac{F_x}{6\pi\eta a^2(1+\varepsilon)\dot{\gamma}} = \frac{(1+\varepsilon)aY^A - 1/2\ Y^{\tilde{B}} - Y^{\tilde{G}}}{6\pi a^2(1+\varepsilon)} \\ \hat{T}^{\dot{\gamma}} &= -\frac{T_z}{4\pi\eta a^3\dot{\gamma}} = \frac{(1+\varepsilon)aY^B + 1/2\ Y^C + Y^{\tilde{H}}}{4\pi a^3} \end{aligned} \tag{D.2}$$

In Fig. D.26, the computed values are compared to the precise computations from Ref. [60]. A very good agreement is observed, although weak oscillations of the quantities with the position may be noted, which are due to the finite mesh size. This explicitly shows that no sub-grid correction is requested for the ambient flow contribution, which amounts to:

$$\begin{aligned} (1+\varepsilon)aY^{A,SG} - 1/2\ Y^{\tilde{B},SG} - Y^{\tilde{G},SG} &= 0 \\ (1+\varepsilon)aY^{B,SG} + 1/2\ Y^{C,SG} + Y^{\tilde{H},SG} &= 0 \end{aligned} \tag{D.3}$$

In addition, the symmetry of the FDM particle-wall matrix has been checked, meaning that $Y^{B,SG} = -Y^{\tilde{B},SG}$, $Y^{G,SG} = Y^{\tilde{G},SG}$ and $Y^{H,SG} = Y^{\tilde{H},SG}$. From Eq. (D.3), the following expressions are deduced:

$$\begin{aligned} Y^{G,SG} &= \ \ (1+\varepsilon)aY^{A,SG} + 1/2\ Y^{B,SG} \\ Y^{H,SG} &= -(1+\varepsilon)aY^{B,SG} - 1/2\ Y^{C,SG} \end{aligned} \tag{D.4}$$

These relations are the equivalent of those quoted Appendix C.2 for the two-particle matrix: the sub-grid correction for $Y^{G,SG}$ and $Y^{H,SG}$ may be directly computed from $Y^{A,SG}$, $Y^{B,SG}$, and $Y^{C,SG}$. This presents the particular advantage that the latter quantities may be computed with better precision using the theoretical expressions proposed by Chaoui and Feuillebois (2003) [60] that are valid over a wide range of the distance between particle and wall, compared to the usual expressions from lubrication approximation that are available in the literature.

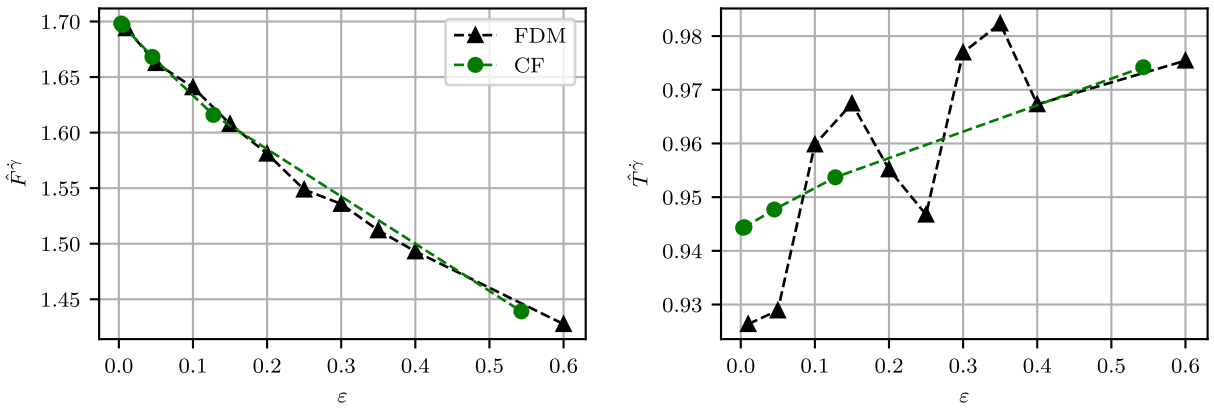

Fig. D.26. $\hat{F}^{\dot{\gamma}}$ and $\hat{T}^{\dot{\gamma}}$ for a particle held fixed near a wall: comparison between FDM computations (▲) and (CF, ●) the results proposed by Chaoui and Feuillebois (2003) [60].

The stresslet was also computed in this case. It is related to the resistance functions through:

$$\begin{aligned} \hat{S}^{\dot{\gamma}} &= \frac{S_{xy}}{10/3\ \pi a^3 \eta \dot{\gamma}} = \frac{-(1+\varepsilon) a Y^G + 1/2\ Y^H + 1/2\ Y^M}{10/3\ \pi a^3} \\ \hat{s}^{\dot{\gamma}} &= 0 \end{aligned} \tag{D.5}$$

As expected, the lubrication approximation of the resistance functions (presented in the Supplementary Material) confirms that no divergence takes place for the stresslet. In addition, the FDM solver yields a very low value for the trace $\hat{s}^{\dot{\gamma},FDM}$ in agreement with Eq. (D.5), and the value of the stresslet for the smallest distance probed ($\epsilon = 10^{-2}$) is close to the asymptotic limit from the lubrication approximation ($\lim_{\varepsilon \to 0}\ \hat{S}^{\dot{\gamma}} = 0.5325$). However, a more detailed comparison is difficult, since the available lubrication approximation for $\hat{S}^{\dot{\gamma}}$ cannot be used as soon as $\varepsilon \gtrsim 10^{-2}$. Nevertheless, the good agreement of the computed stresslet in the case of a free particle in a shear flow close to the wall (Section 5.2) is a further confirmation that no specific correction is needed in the current case.

Finally, the sub-grid stress moments vector reduces to the first term of the RHS of Eq. (D.1):

$$\begin{pmatrix} \mathbf{F}_p^{SG} \\ \mathbf{T}_p^{SG} \\ \mathbf{S}_p^{SG} \\ s_p^{SG} \end{pmatrix} = -\eta \begin{pmatrix} \mathbf{A}_w^{SG} & \tilde{\mathbf{B}}_w^{SG} \\ \mathbf{B}_w^{SG} & \mathbf{C}_w^{SG} \\ \mathbf{G}_w^{SG} & \mathbf{H}_w^{SG} \\ \mathbf{P}_w^{SG} & \mathbf{0} \end{pmatrix} \cdot \begin{pmatrix} \mathbf{U}_p - \mathbf{U}_w \\ \mathbf{\Omega}_p \end{pmatrix} \tag{D.6}$$

Eq. (D.6) does not depend on a specific reference frame, since it precisely involves the translational and angular velocities of the particle in the reference frame attached to the translating wall. As a consequence, it may be used as it is without further caution.

References

[1] M. R. Maxey, Simulation Methods for Particulate Flows and Concentrated Suspensions, Annual Review of Fluid Mechanics 49 (1) (2017) 171–193. doi:10.1146/annurev-fluid-122414-034408.

[2] J. F. Brady, Stokesian Dynamics, Annual Review of Fluid Mechanics 20 (111-57) (1988) 47. doi:10.1146/annurev.fl.20.010188.000551.

[3] A. Sierou, J. F. Brady, Accelerated Stokesian Dynamics simulations, Journal of Fluid Mechanics 448 (2001) 115–146. doi:10.1017/S0022112001005912.

[4] I. L. Claeys, J. F. Brady, Suspensions of prolate spheroids in Stokes flow. Part 1. Dynamics of a finite number of particles in an unbounded fluid, Journal of Fluid Mechanics 251 (1993) 411–442. doi:10.1017/S0022112093003465.

[5] J. W. Swan, J. F. Brady, The hydrodynamics of confined dispersions, Journal of Fluid Mechanics 687 (2011) 254–299. doi:10.1017/jfm.2011.351.

[6] K. Yeo, M. R. Maxey, Simulation of concentrated suspensions using the force-coupling method, Journal of Computational Physics 229 (6) (2010) 2401–2421. doi:10.1016/j.jcp.2009.11.041.

[7] K. Yeo, M. R. Maxey, Dynamics of concentrated suspensions of non-colloidal particles in Couette flow, Journal of Fluid Mechanics 649 (2010) 205–231. doi:10.1017/S0022112009993454.

[8] D. Liu, E. Keaveny, M. R. Maxey, G. Karniadakis, Force-coupling method for flows with ellipsoidal particles, Journal of Computational Physics 228 (10) (2009) 3559–3581. doi:10.1016/j.jcp.2009.01.020.

[9] M. Abbas, P. Magaud, Y. Gao, S. Geoffroy, Migration of finite sized particles in a laminar square channel flow from low to high Reynolds numbers, Physics of Fluids 26 (12) (2014) 123301. doi:10.1063/1.4902952.

[10] M. Uhlmann, An immersed boundary method with direct forcing for the simulation of particulate flows, Journal of Computational Physics 209 (2) (2005) 448–476. doi:10.1016/j.jcp.2005.03.017.

[11] W.-P. Breugem, A second-order accurate immersed boundary method for fully resolved simulations of particle-laden flows, Journal of Computational Physics 231 (13) (2012) 4469–4498. doi:10.1016/j.jcp.2012.02.026.

[12] R. Glowinski, A distributed Lagrange multiplier/fictitious domain method for particulate flows, International Journal of Multiphase Flow 184 (2-4) (1999) 241–267. doi:http://dx.doi.org/10.1016/S0045-7825(99)00230-3.

[13] R. Glowinski, T. W. Pan, T. Hesla, D. Joseph, J. Périaux, A Fictitious Domain Approach to the Direct Numerical Simulation of Incompressible Viscous Flow past Moving Rigid Bodies: Application to Particulate Flow, Journal of Computational Physics 169 (2) (2001) 363–426. doi:10.1006/jcph.2000.6542.

[14] A. Wachs, Peligriff, a parallel dem-dlm/fd direct numerical simulation tool for 3d particulate flows, Journal of Engineering Mathematics 71 (1) (2011) 131–155. doi:https://doi.org/10.1007/s10665-010-9436-2.

[15] N. Patankar, P. Singh, D. Joseph, R. Glowinski, T. W. Pan, A new formulation of the distributed Lagrange multiplier/fictitious domain method for particulate flows, International Journal of Multiphase Flow 26 (9) (2000) 1509–1524. doi:10.1016/S0301-9322(99)00100-7.

[16] S. Gallier, E. Lemaire, L. Lobry, F. Peters, A fictitious domain approach for the simulation of dense suspensions, Journal of Computational Physics 256 (2014) 367–387. doi:10.1016/j.jcp.2013.09.015.

[17] M. Wu, B. Peters, T. Rosemann, H. Kruggel-Emden, A forcing fictitious domain method to simulate fluid-particle interaction of particles with super-quadric shape, Powder Technology 360 (2020) 264–277. doi:10.1016/j.powtec.2019.09.088.

[18] X. Bian, S. Litvinov, R. Qian, M. Ellero, N. A. Adams, Multiscale modeling of particle in suspension with smoothed dissipative particle dynamics, Physics of Fluids 24 (1) (2012) 012002. doi:10.1063/1.3676244.

[19] A. Vázquez-Quesada, M. Ellero, Rheology and microstructure of non-colloidal suspensions under shear studied with Smoothed Particle Hydrodynamics, Journal of Non-Newtonian Fluid Mechanics 233 (2016) 37–47. doi:10.1016/j.jnnfm.2015.12.009.

[20] A. Vázquez-Quesada, M. Ellero, SPH modeling and simulation of spherical particles interacting in a viscoelastic matrix, Physics of Fluids 29 (12) (2017) 121609. doi:10.1063/1.4993610.

[21] A. J. C. Ladd, Numerical simulations of particulate suspensions via a discretized Boltzmann equation. Part 1. Theoretical foundation, Journal of Fluid Mechanics 271 (1994) 285–309. doi:10.1017/S0022112094001771.

[22] N. Q. Nguyen, A. J. C. Ladd, Lubrication corrections for lattice-Boltzmann simulations of particle suspensions, Physical Review E 66 (4) (2002) 046708. doi:10.1103/PhysRevE.66.046708.

[23] R. Mari, R. Seto, J. F. Morris, M. M. Denn, Shear thickening, frictionless and frictional rheologies in non-Brownian suspensions, Journal of Rheology 58 (6) (2014) 1693–1724. doi:10.1122/1.4890747.

[24] C. Ness, J. Sun, Flow regime transitions in dense non-Brownian suspensions: Rheology, microstructural characterization, and constitutive modeling, Physical Review E 91 (1) (2015) 012201. doi:10.1103/PhysRevE.91.012201.

[25] T. Pöschel, T. Schwager, Computational Granular Dynamics: Models and Algorithms, Springer-Verlag, Berlin; New York, 2005. doi:https://doi.org/10.1007/3-540-27720-X.

[26] S. P. Kumar, A. Vázquez-Quesada, M. Ellero, A conservative lubrication dynamics method for the simulation of dense non-colloidal suspensions with particle spin, Journal of Computational Physics 427 (2021) 110001. doi:https://doi.org/10.1016/j.jcp.2020.110001.

[27] R. Seto, R. Mari, J. F. Morris, M. M. Denn, Discontinuous Shear Thickening of Frictional Hard-Sphere Suspensions, Physical Review Letters 111 (21) (2013) 218301. doi:10.1103/PhysRevLett.111.218301.

[28] J. F. Morris, Lubricated-to-frictional shear thickening scenario in dense suspensions, Physical Review Fluids 3 (11) (2018) 110508. doi:10.1103/PhysRevFluids.3.110508.

[29] A. Singh, C. Ness, R. Seto, J. J. de Pablo, H. M. Jaeger, Shear Thickening and Jamming of Dense Suspensions: The "Roll" of Friction, Physical Review Letters 124 (24) (2020) 248005. doi:10.1103/PhysRevLett.124.248005.

[30] M. A. Jones, C. Ness, Linking attractive interactions and confinement to the rheological response of suspended particles close to jamming, Granular Matter 20 (1) (2018) 3. doi:10.1007/s10035-017-0770-1.
[31] O. Cheal, C. Ness, Rheology of dense granular suspensions under extensional flow, Journal of Rheology 62 (2) (2018) 501–512. doi:10.1122/1.5004007.
[32] S. Gallier, F. Peters, L. Lobry, Simulations of sheared dense noncolloidal suspensions: Evaluation of the role of long-range hydrodynamics, Physical Review Fluids 3 (4) (2018) 042301. doi:10.1103/PhysRevFluids.3.042301.
[33] É. Guazzelli, J. Hinch, Fluctuations and Instability in Sedimentation, Annual Review of Fluid Mechanics 43 (1) (2011) 97–116. doi:10.1146/annurev-fluid-122109-160736.
[34] E. Catalano, B. Chareyre, E. Barthélémy, Pore-scale modeling of fluid-particles interaction and emerging poromechanical effects: Pore-scaling modeling of fluid-particles interactions, International Journal for Numerical and Analytical Methods in Geomechanics 38 (1) (2014) 51–71. doi:10.1002/nag.2198.
[35] W. Chèvremont, B. Chareyre, H. Bodiguel, Quantitative study of the rheology of frictional suspensions: Influence of friction coefficient in a large range of viscous numbers, Physical Review Fluids 4 (6) (2019) 064302. doi:10.1103/PhysRevFluids.4.064302.
[36] J. J. J. Gillissen, C. Ness, Modeling the Microstructure and Stress in Dense Suspensions under Inhomogeneous Flow, Physical Review Letters 125 (18) (2020) 184503. doi:10.1103/PhysRevLett.125.184503.
[37] J. Happel, H. Brenner, Low Reynolds number hydrodynamics 1 (1981). doi:10.1007/978-94-009-8352-6.
[38] S. Kim, S. J. Karrila, Microhydrodynamics: principles and selected applications, Dover Publications Inc., 2005. doi:https://doi.org/10.1016/C2013-0-04644-0.
[39] P. R. Nott, J. F. Brady, Pressure-driven flow of suspensions: Simulation and theory, Journal of Fluid Mechanics 275 (1994) 157–199. doi:10.1017/S0022112094002326.
[40] K. Yeo, M. R. Maxey, Numerical simulations of concentrated suspensions of monodisperse particles in a Poiseuille flow, Journal of Fluid Mechanics 682 (2011) 491–518. doi:10.1017/jfm.2011.241.
[41] G. K. Batchelor, The stress system in a suspension of force-free particles, Journal of Fluid Mechanics 41 (3) (1970) 545–570. doi:10.1017/S0022112070000745.
[42] D. J. Jeffrey, J. F. Morris, J. F. Brady, The pressure moments for two rigid spheres in low-Reynolds-number flow, Physics of Fluids A: Fluid Dynamics 5 (10) (1993) 2317–2325. doi:10.1063/1.858795.
[43] D. J. Jeffrey, Y. Onishi, Calculation of the resistance and mobility functions for two unequal rigid spheres in low-Reynolds-number flow, Journal of Fluid Mechanics 139 (1984) 261–290. doi:10.1017/S0022112084000355.
[44] D. J. Jeffrey, The calculation of the low Reynolds number resistance functions for two unequal spheres, Physics of Fluids A: Fluid Dynamics 4 (1) (1992) 16–29. doi:10.1063/1.858494.
[45] R. Rivlin, J. Ericksen, Stress-deformation relations for isotropic materials, Journal of Rational Mechanics and Analysis 4 (1955) 323–425doi:10.1512/iumj.1955.4.54011.
[46] P. Saramito, Complex Fluids: Modeling and Algorithms, Vol. 79 of Mathématiques et Applications, Springer International Publishing, Cham, 2016. doi:10.1007/978-3-319-44362-1.
[47] R. Ball, J. Melrose, A simulation technique for many spheres in quasi-static motion under frame-invariant pair drag and Brownian forces, Physica A: Statistical Mechanics and its Applications 247 (1-4) (1997) 444–472. doi:10.1016/S0378-4371(97)00412-3.
[48] S. Plimpton, Fast Parallel Algorithms for Short-Range Molecular Dynamics, Journal of Computational Physics 117 (1) (1995) 1–19. doi:10.1006/jcph.1995.1039.
[49] B. Cichocki, M. L. Ekiel-Jeżewska, E. Wajnryb, Lubrication corrections for three-particle contribution to short-time self-diffusion coefficients in colloidal dispersions, The Journal of Chemical Physics 111 (7) (1999) 3265–3273. doi:10.1063/1.479605.
[50] D. J. Jeffrey, Programs for Stokes resistance functions, URL: https://www.uwo.ca/apmaths/faculty/jeffrey/research/Resistance.html (2021).
[51] H. Jasak, Error analysis and estimation for the finite volume method with applications to fluid flows, Ph.D. thesis, Imperial College London (University of London), URL: http://hdl.handle.net/10044/1/8335 (1996).
[52] F. Moukalled, L. Mangani, M. Darwish, The Finite Volume Method in Computational Fluid Dynamics: An Advanced Introduction with OpenFOAM® and Matlab, Vol. 113 of Fluid Mechanics and Its Applications, Springer International Publishing, Cham, 2016. doi:10.1007/978-3-319-16874-6.
[53] R. Issa, Solution of the implicitly discretised fluid flow equations by operator-splitting, Journal of Computational Physics 62 (1) (1986) 40–65. doi:10.1016/0021-9991(86)90099-9.
[54] K. Yeo, M. R. Maxey, Ordering transition of non-Brownian suspensions in confined steady shear flow, Physical Review E 81 (5) (2010) 051502. doi:10.1103/PhysRevE.81.051502.
[55] S. Gallier, E. Lemaire, F. Peters, L. Lobry, Rheology of sheared suspensions of rough frictional particles, Journal of Fluid Mechanics 757 (2014) 514–549. doi:10.1017/jfm.2014.507.
[56] S. Gallier, E. Lemaire, L. Lobry, F. Peters, Effect of confinement in wall-bounded non-colloidal suspensions, Journal of Fluid Mechanics 799 (2016) 100–127. doi:10.1017/jfm.2016.368.
[57] G. Guennebaud, B. Jacob, et al., Eigen v3.4, http://eigen.tuxfamily.org (2021).
[58] H. Hasimoto, On the periodic fundamental solutions of the Stokes equations and their application to viscous flow past a cubic array of spheres, Journal of Fluid Mechanics 5 (02) (1959) 317. doi:10.1017/S0022112059000222.
[59] A. A. Zick, G. M. Homsy, Stokes flow through periodic arrays of spheres, Journal of Fluid Mechanics 115 (-1) (1982) 13. doi:10.1017/S0022112082000627.
[60] M. Chaoui, F. Feuillebois, Creeping flow around a sphere in a shear flow close to a wall, The Quarterly Journal of Mechanics and Applied Mathematics 56 (2003) 381–410. doi:10.1093/qjmam/2F56.3.381.

[61] A. S. Sangani, A. Acrivos, P. Peyla, Roles of particle-wall and particle-particle interactions in highly confined suspensions of spherical particles being sheared at low Reynolds numbers, Physics of Fluids 23 (8) (2011) 083302. doi:10.1063/1.3613972.
[62] M. E. Staben, A. Z. Zinchenko, R. H. Davis, Motion of a particle between two parallel plane walls in low-Reynolds-number Poiseuille flow, Physics of Fluids 15 (6) (2003) 1711. doi:10.1063/1.1568341.
[63] N. Ghalya, A. Sellier, M. L. Ekiel-Jeżewska, F. Feuillebois, Effective viscosity of a dilute homogeneous suspension of spheres in Poiseuille flow between parallel slip walls, Journal of Fluid Mechanics 899 (2020) A13. doi:10.1017/jfm.2020.429.
[64] F. R. Da Cunha, E. J. Hinch, Shear-induced dispersion in a dilute suspension of rough spheres, Journal of Fluid Mechanics 309 (1996) 211–223. doi:10.1017/S0022112096001619.
[65] I. E. Zarraga, D. T. Leighton, Shear-Induced Diffusivity in a Dilute Bidisperse Suspension of Hard Spheres, Journal of Colloid and Interface Science 243 (2) (2001) 503–514. doi:10.1006/jcis.2001.7854.
[66] S. Bhattacharya, J. Bławzdziewicz, E. Wajnryb, Hydrodynamic interactions of spherical particles in Poiseuille flow between two parallel walls, Physics of Fluids 18 (5) (2006) 053301. doi:10.1063/1.2195992.
[67] H. J. Wilson, Stokes flow past three spheres, Journal of Computational Physics 245 (2013) 302–316. doi:10.1016/j.jcp.2013.03.020.
[68] F. Blanc, F. Peters, E. Lemaire, Experimental Signature of the Pair Trajectories of Rough Spheres in the Shear-Induced Microstructure in Noncolloidal Suspensions, Physical Review Letters 107 (20) (2011) 208302. doi:10.1103/PhysRevLett.107.208302.
[69] P. Pham, B. Metzger, J. E. Butler, Particle dispersion in sheared suspensions: Crucial role of solid-solid contacts, Physics of Fluids 27 (2015) 051701. doi:10.1063/1.4919728.
[70] F. Peters, G. Ghigliotti, S. Gallier, F. Blanc, E. Lemaire, L. Lobry, Rheology of non-Brownian suspensions of rough frictional particles under shear reversal: A numerical study, Journal of Rheology 60 (4) (2016) 715–732. doi:10.1122/1.4954250.
[71] A. Singh, R. Mari, M. M. Denn, J. F. Morris, A constitutive model for simple shear of dense frictional suspensions, Journal of Rheology 62 (2) (2018) 457–468. doi:10.1122/1.4999237.
[72] F. Blanc, E. Lemaire, A. Meunier, F. Peters, Microstructure in sheared non-Brownian concentrated suspensions, Journal of Rheology 57 (1) (2013) 273–292. doi:10.1122/1.4766597.
[73] M. Sarabian, M. Firouznia, B. Metzger, S. Hormozi, Fully developed and transient concentration profiles of particulate suspensions sheared in a cylindrical Couette cell, Journal of Fluid Mechanics 862 (2019) 659–671. doi:10.1017/jfm.2018.982.
[74] E. d'Ambrosio, F. Blanc, E. Lemaire, Viscous resuspension of non-Brownian particles: Determination of the concentration profiles and particle normal stresses, Journal of Fluid Mechanics 911 (2021) A22. doi:10.1017/jfm.2020.1074.
[75] L. Lobry, E. Lemaire, F. Blanc, S. Gallier, F. Peters, Shear thinning in non-Brownian suspensions explained by variable friction between particles, Journal of Fluid Mechanics 860 (2019) 682–710. doi:10.1017/jfm.2018.881.
[76] A. Badia, Y. D'Angelo, F. Peters, L. Lobry, Frame-invariant modeling for non-brownian suspension flows, Journal of Non-Newtonian Fluid Mechanics 309 (2022) 104904. doi:https://doi.org/10.1016/j.jnnfm.2022.104904.
[77] D. Lhuillier, Migration of rigid particles in non-Brownian viscous suspensions, Physics of Fluids 21 (2) (2009) 023302. doi:10.1063/1.3079672.
[78] P. R. Nott, E. Guazzelli, O. Pouliquen, The suspension balance model revisited, Physics of Fluids 23 (4) (2011) 043304. doi:10.1063/1.3570921.
[79] M. K. Lyon, L. G. Leal, An experimental study of the motion of concentrated suspensions in two-dimensional channel flow. Part 1. Monodisperse systems, Journal of Fluid Mechanics 363 (1998) 25–56. doi:10.1017/S0022112098008817.
[80] C. Gao, B. Xu, J. F. Gilchrist, Mixing and segregation of microspheres in microchannel flows of mono- and bidispersed suspensions, Physical Review E 79 (3) (2009) 036311. doi:10.1103/PhysRevE.79.036311.
[81] S. C. Jana, B. Kapoor, A. Acrivos, Apparent wall slip velocity coefficients in concentrated suspensions of noncolloidal particles, Journal of Rheology 39 (6) (1995) 1123–1132. doi:10.1122/1.550631.
[82] P. Mills, P. Snabre, Rheology and Structure of Concentrated Suspensions of Hard Spheres. Shear Induced Particle Migration, Journal de Physique II 5 (10) (1995) 1597–1608. doi:10.1051/jp2:1995201.
[83] J. F. Morris, F. Boulay, Curvilinear flows of noncolloidal suspensions: The role of normal stresses, Journal of Rheology 43 (5) (1999) 1213–1237. doi:10.1122/1.551021.
[84] B. Snook, J. E. Butler, É. Guazzelli, Dynamics of shear-induced migration of spherical particles in oscillatory pipe flow, Journal of Fluid Mechanics 786 (2016) 128–153. doi:10.1017/jfm.2015.645.
[85] R. M. Miller, J. F. Morris, Normal stress-driven migration and axial development in pressure-driven flow of concentrated suspensions, Journal of Non-Newtonian Fluid Mechanics 135 (2-3) (2006) 149–165. doi:10.1016/j.jnnfm.2005.11.009.
[86] C. Gao, S. D. Kulkarni, J. F. Morris, J. F. Gilchrist, Direct investigation of anisotropic suspension structure in pressure-driven flow, Physical Review E 81 (4) (2010) 041403. doi:10.1103/PhysRevE.81.041403.
[87] S. Oh, Y.-q. Song, D. I. Garagash, B. Lecampion, J. Desroches, Pressure-driven suspension flow near jamming, Physical review letters 114 (8) (2015) 088301. doi:10.1103/PhysRevLett.114.088301.
[88] B. Lecampion, D. I. Garagash, Confined flow of suspensions modelled by a frictional rheology, Journal of Fluid Mechanics 759 (2014) 197–235. doi:10.1017/jfm.2014.557.
[89] F. Boyer, É. Guazzelli, O. Pouliquen, Unifying Suspension and Granular Rheology, Physical Review Letters 107 (18) (2011) 188301. doi:10.1103/PhysRevLett.107.188301.